

Preliminary Design of a 30 kN
Methane-Oxygen-powered
Electric-Pump-fed
Liquid Rocket Propulsion System

Vikramjeet Das

Space Engineering, master's level
2023

Luleå University of Technology
Department of Computer Science, Electrical and Space Engineering



PRELIMINARY DESIGN OF A 30 kN
METHANE-OXYGEN-POWERED
ELECTRIC-PUMP-FED
LIQUID ROCKET PROPULSION SYSTEM



PRELIMINARY DESIGN OF A 30 KN
METHANE-OXYGEN-POWERED
ELECTRIC-PUMP-FED
LIQUID ROCKET PROPULSION SYSTEM

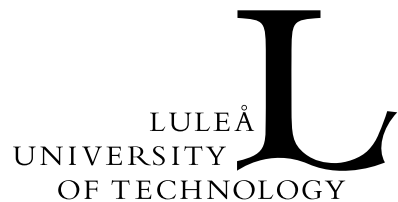
VIKRAMJEET DAS

Master in Space Engineering
Luleå University of Technology

Supervisors: Dr Élcio Jeronimo de Oliveira

R. Murugesan (PhD)

Examiner: Dr Victoria Barabash



Vikramjeet Das: *Preliminary Design of a 30 kN Methane-Oxygen-powered Electric-Pump-fed Liquid Rocket Propulsion System*

May 2023

*A thesis submitted in partial fulfilment of the requirements for
the degree of Master in Space Engineering
at the Division of Space Technology*

Department of Computer Science, Electrical and Space Engineering
Luleå University of Technology
Kiruna, Sweden

Correspondence with the author may be directed to
vikramjeet101@gmail.com

An electronic version of this thesis is available at
www.ltu.se/publications

Cover image: The methane-oxygen-powered JD-1 rocket engine from i-Space.

Keywords: rocket engine, liquid rocket, methalox, electropump, LRPS, LPRE

URN:

OAI:

DiVA, id:

For Cyrus boi

CONTENTS

ABSTRACT	xiii
ACKNOWLEDGEMENTS	xv
LIST OF FIGURES	xvii
LIST OF TABLES	xix
LIST OF ABBREVIATIONS	xxi
LIST OF SYMBOLS	xxiii
1 INTRODUCTION	1
1.1 Design Objective	2
1.2 Project Motivation	3
1.3 Thesis Outline	9
2 FUNDAMENTALS OF ROCKET PROPULSION	13
2.1 Ideal Rocket Propulsion System	13
2.2 Performance Parameters	14
2.2.1 Thrust	14
2.2.2 Specific Impulse	15
2.2.3 Effective Exhaust Velocity	16
2.2.4 Characteristic Velocity	17
2.2.5 Thrust Coefficient	17
2.2.6 Average Exhaust Velocity	18
2.2.7 Propellant Mass Flow Rate	19

2.2.8	Density Impulse	19
2.3	Quasi 1-D Flow Parameters	20
2.3.1	Isentropic Flow Condition	20
2.3.2	Nozzle Throat Conditions	20
2.4	Real Rocket Propulsion System	21
2.5	Engine Nomenclature	23
3	LIQUID PROPELLANTS	25
3.1	Propellant Characteristics	25
3.1.1	Important Aspects & Desirable Features.	26
3.1.2	Classification of Propellants	26
3.1.3	Propellant Selection Criteria	27
3.2	Candidate Propellants.	28
3.2.1	Liquid Oxygen (LOX)	28
3.2.2	Liquid Hydrogen (LH ₂)	29
3.2.3	Rocket Propellant 1 (RP-1)	30
3.2.4	Liquid Methane (LCH ₄)	31
3.3	Propellant Performance Analysis	33
3.4	Mixture Ratio	34
3.4.1	Liquid Oxygen & Liquid Methane.	35
3.4.2	Liquid Oxygen & Liquid Hydrogen	39
3.4.3	Liquid Oxygen & Rocket Propellant 1	40
3.5	Summary	43
4	PROPELLANT FEED SYSTEMS	45
4.1	Types of Feed Systems.	45
4.1.1	Pressure Feed Systems.	46
4.1.2	Turbopump Feed Systems	47
4.1.3	Electropump Feed Systems	50
4.2	Feed System Selection Criteria	52
4.2.1	Optimum Pressure Ratio	53
4.2.2	Combustion Chamber Pressure	54
4.3	Suitability of Feed Systems	56
4.3.1	Pressure Feed System	56
4.3.2	Turbopump Feed System	57
4.3.3	Electropump Feed System	62
4.3.4	Analysis of the Feed System Mass	66
4.4	Summary	70

5	DESIGN OF THE THRUST CHAMBER	73
5.1	Design Requirements	73
5.2	Design Parameters.	74
5.2.1	Expansion Area Ratios.	74
5.2.2	Performance Parameters	76
5.2.3	Performance Correction Factors	79
5.3	Design of the Nozzle	79
5.3.1	Ideal Nozzle	80
5.3.2	Truncated Ideal Contoured (TIC) Nozzle	85
5.3.3	Thrust Optimised Contoured (TOC) Nozzle	87
5.3.4	Thrust Optimised Parabolic (TOP) Nozzle	88
5.4	Design of the Combustion Chamber	91
5.5	Summary	93
6	THRUST CHAMBER DESIGN SPECIFICS	95
6.1	Thermal Management.	95
6.1.1	Booster-Stage Thrust Chamber	98
6.1.2	Upper-Stage Thrust Chamber	104
6.2	Injector Design	105
6.2.1	Injection Elements	106
6.2.2	Design of Injection Elements.	108
6.3	Launch Vehicle Specifics.	111
6.4	Summary	114
7	CONCLUSION	119
7.1	Conclusion	119
7.2	Limitations & Future Work	121
A	CEA COMPUTATION	125
B	MATLAB SCRIPT	127
B.1	Thrust Chamber Parameters.	127
B.2	Engine Cycle Parameters	139
B.3	Vehicle Mass Parameters	144
	BIBLIOGRAPHY	147

ABSTRACT

The design of a liquid rocket propulsion system, unlike that of a standalone system, is intertwined with the overall development of a number of associated systems and is influenced by a multitude of conditions and considerations: from the requirements needed to accomplish the mission to the rationalizations involved behind the development of each rocket system and/or component. In my thesis, the preliminary design of a “new generation” 30 kN rocket engine driven by an electric pump feed system and running on liquid methane and liquid oxygen is performed. The propulsion system would be employed on a hypothetical small-lift orbital-class twin-stage rocket to deliver a light payload of about 200 kg into a circular 500 km LEO. Such topics as the selection of bipropellant combinations, the feasibility of electric pump feed systems, design methodologies for thrust chambers, for nozzles in particular, management of the high thermal energy and the selection of compatible wall materials, as well as the design of an injector have been looked comprehensively into.

It is realized that methalox is indeed better than both hydrolox (with regard to density impulse) and kerolox (in terms of specific impulse). Besides, a suite of attractive characteristics makes the bipropellant a combination of choice to power rockets of the future. Yet more notably, an electric-pump-fed engine cycle is, under the right circumstances of engine operation, established to outperform both the pressure feed system and the turbopump feed system. With constant advancement in battery technologies, improvement of both power density and energy density to achieve much higher performance is but a matter of time. The adoption of a propulsion system such as ours for a mission objective as outlined above, therefore, is not just viable but unquestionably realistic.

Two thrust chamber versions—a sea-level variant for the booster stage and a vacuum-optimized variant for the upper stage—are developed for our rocket. And both the nozzles employ a TOP “thrust optimised parabolic” contour; also, the booster stage comprises a cluster of 9 engines in a parallel burn arrangement. Concerning thermal management, the entirety of the booster-stage thrust chamber implements regenerative cooling (using Inconel 625), whereas the aft of the upper-stage nozzle section implements radiative cooling (with Niobium C-103). Further, the injector faceplate (also of Inconel 625) comprises two concentric patterns of unlike impingement doublet sets: with 80 pairs on the outer ring and 40 pairs on the inner ring. With rational assumptions, our hypothetical launch vehicle is deemed to have a mass of roughly 17200 kg (200 kg of which is the payload) and a delta-v of approximately 9600 m/s—quite within the desirable range of specifications for small-lift orbital-class twin-stage rockets of today.

ACKNOWLEDGEMENTS

As I stand on the precipice of completion of this master's thesis, I find myself brimming with an overwhelming sense of gratitude—of awe—from the deepest depths of my being. This degree project draws the curtains on my studies in Space Science & Technology for the Space Engineering programme at LTU. The culmination of this intellectual odyssey would not have been possible without the unwavering support, encouragement and inspiration by the wonderful individuals who have shaped the trajectory of my scholarly journey and touched my life in extraordinary ways.

First, I extend my deepest gratitude to Élcio for agreeing to take me under his wing. His expertise, wisdom and guidance coupled with his kind and patient personality have been instrumental in influencing my work. I now understand quite well that “it is not so simple” to design a rocket engine; and yet we have somehow done it together. To Ramakrishnan, you have been the beacon of light when I needed help the most and my catalyst without whom I would perhaps not be standing here today. Your invaluable mentorship, genuine passion for knowledge and relentless pursuit of excellence have shaped not only my research but also my character. I express my heartfelt appreciation to Victoria Barabash for believing in me throughout my studies. I am forever indebted to you for the immeasurable impact you have had on both my academic and my personal growth. I am immensely thankful to all the professors at LTU Rymdcampus, to Maria Winnebäck and to Anette Snällfot-Brändström for nurturing my intellectual curiosity, imparting their knowledge and offering their care during my time at Kiruna.

Throughout my studies, I have met some amazing souls who I share a lot of fond memories with: Lea, Aakash, Matthias, Adam, Roger, Selvamuthukumaran,

Anand, Meltem, Stevan, Akila, Franziska, Markus, Max, Sergio, Ricardo, the list keeps going. Thanks for providing me all those happy distractions. Attman, you have been my awesome friend ever since I have known you. Nabbu and Subbu, thank you for being there anytime and everytime I needed you. Roshni, thank you for making my world your own and for everything that you have done for me. I will forever cherish everything about you! Thanks, Anuswiya, for having my back at all times, for loving, understanding and encouraging me so much, no matter what. You are the absolute best!

Sushree, thanks for being the nicest sibling I could ever get, and for bringing in good and happy vibes all the time. I am unfathomably thankful to my beloved parents for all their blessings, love, sacrifices, support, care and concern, and for making me the person that I am today. Lastly, Carl Sagan, you are—and always will be—my greatest inspiration on my ephemeral voyage through the cosmos aboard “the pale blue dot, the only home we’ve ever known”.

FIGURES

1.1. A render of the V-2	2
1.2. SpaceX Falcon 9	4
1.3. Rocket Lab Electron	5
1.4. Typical flight profile of a launch vehicle	6
1.5. Electron ready to launch on the Virginia Is For Launch Lovers mission	7
1.6. Four commercial small satellites by Axelspace	8
1.7. Overview of Rocket Lab Electron	10
2.1. Major components/sections of a rocket engine	24
3.1. Optimum Mixture Ratio for Liquid Oxygen and Liquid Methane . .	36
3.2. Specific Impulse vs Mixture Ratio	37
3.3. Temperature vs Mixture Ratio	37
3.4. Characteristic Velocity & Molecular Mass vs Mixture Ratio . . .	38
3.5. Specific Impulse & Temperature vs Mixture Ratio	38
3.6. Optimum Mixture Ratio for Liquid Oxygen and Liquid Hydrogen .	39
3.8. Optimum Mixture Ratio for Liquid Oxygen and Liquid Hydrogen .	40
3.7. Specific Impulse & Temperature & Molecular Mass vs Mixture Ratio for LOX/LH ₂	41
3.9. Specific Impulse & Temperature & Molecular Mass vs Mixture Ratio for LOX/RP-1	41
3.10. Specific Impulse vs Mixture Ratio for all three bipropellants considered	42
3.11. The relative volume of respective fuels against the oxidizer volume .	42
4.1. Schematic of a pressure feed system	47
4.2. Schematics of turbopump feed systems	49

4.3. Schematic of an electropump feed system	51
4.4. Thrust Coefficient & Specific Impulse vs Pressure Ratio	55
4.5. Expansion Area Ratio & Exit Pressure vs Pressure Ratio	55
4.6. Variation of feed system mass with engine burn time	69
4.7. Variation of feed system mass ratio with engine burn time	69
5.1. Variation of combustion parameters with chamber pressure	77
5.2. Local characteristic curves of a streamline	81
5.3. Design schematic of a supersonic nozzle contour using the method of characteristics	83
5.4. Nozzle contours for our thrust chamber variants using the method of characteristics	84
5.5. Illustration of TIC nozzle constraints	86
5.6. TOC Nozzle Schematic	87
5.7. Schematic of a TOP nozzle	88
5.8. The two angles of a parabolic nozzle	89
5.9. Combustor configuration layout	92
5.10. Thrust chamber cross-sectional profiles	93
6.1. Variation of nozzle parameters with Mach number	96
6.2. Variation of nozzle parameters with pressure	97
6.3. Schematic diagram of the coolant channel	99
6.4. Configuration of the cooling jacket	101
6.5. Heat flux distribution on the inner thrust chamber wall	102
6.6. Temperature distribution on the thrust chamber inner wall surfaces .	102
6.7. Variation of both temperature and pressure for the coolant	103
6.8. Schematic diagram of the upper-stage thrust chamber	104
6.9. Temperature distribution on the upper-stage thrust chamber wall surfaces	105
6.10. Typical configuration of an unlike doublet injector	109
6.11. Injector configuration layout	111
6.12. Impingement angles and resultant jet momentum	112
6.13. Booster stage engine cluster configuration	116

TABLES

2.1. Convention used for our rocket engine	24
4.1. Preliminary parameters for thrust chamber	56
4.2. Specifications for feed system mass estimation	68
6.1. Material properties of Inconel 625	100
6.2. Cooling jacket parameters	103
6.3. Parameters for the injector design	112
6.4. Preliminary mass and delta-v values of our launch vehicle	115

ABBREVIATIONS

1-D	One Dimensional
2-D	Two Dimensional
APS	Ascent Propulsion System
CEA	Chemical Equilibrium with Applications
CFD	Computational Fluid Dynamics
CTIC	Compressed Truncated Ideal Contour
Cubesat	Cube Satellite
DC	Direct Current
DPS	Descent Propulsion System
Electropump	Electric Pump
EPFS	Electropump Feed System
ESA	European Space Agency
FEA	Finite Element Analysis
GG	Gas Generator
Hydrolox	(Liquid) Hydrogen & Liquid Oxygen
IRFNA	Inhibited Red Fuming Nitric Acid
JP-4	Jet Propellant 4
Kerolox	Kerosene & Liquid Oxygen,
LCH4	Liquid Methane
LEO	Low Earth Orbit
LH2	Liquid Hydrogen
LiPo	Lithium Polymer
LNG	Liquefied Natural Gas
LOX	Liquid Oxygen

LPRE	Liquid Propellant Rocket Engine
LRPS	Liquid Rocket Propulsion System
Methalox	(Liquid) Methane & Liquid Oxygen
MMH	Monomethylhydrazine
NASA	National Aeronautics and Space Administration
NTO	Dinitrogen Tetroxide
OMS	Orbital Maneuvering System
PMSM	Permanent Magnet Synchronous Motor
RP-1	Rocket Propellant 1
RPA	Rocket Propulsion Analysis
SPS	Service Propulsion System
SSO	Sun Synchronous Orbit
TC	Thrust Chamber
TIC	Truncated Ideal Contour
TOC	Thrust Optimised Contour
TOP	Thrust Optimised Parabola
TPFS	Turbopump Feed System
UDMH	Unsymmetrical Dimethylhydrazine
WF	Working Fluid

SYMBOLS

A	Cross-sectional area
a	Sonic velocity
c	Effective exhaust velocity
c^*	Characteristic velocity
c_P	Heat capacity (constant pressure)
c_V	Heat capacity (constant volume)
C	Characteristic curve
C_d	Discharge coefficient
C_f	Thrust coefficient
d	Density
D	Diameter
e	Energy
F	Thrust
h	Fluid head
I	Impulse
I_s	Specific impulse
I_{svac}	Specific impulse (vacuum)
I_{sd}	Density impulse
K	Constant
k	Specific heat ratio
L	Length
L^*	Characteristic length
M	Mach number
M	Mixing factor

m	Mass
\dot{m}	Propellant mass flow rate
N	Number of engine clusters
O/F	Propellant mass mixture ratio
p	Power
P	Pressure
ΔP	Head rise/Pressure drop
R	Gas constant
R	Radius
S	Surface area
T	Temperature
t	Time
v	Average velocity
Δv	Velocity increment
V	Volume
\dot{w}	Propellant weight flow rate
X	Variable
MR	Mass ratio
M	Effective molecular mass
δ	Density
ϵ	Nozzle expansion area ratio
ϵ_c	Nozzle contraction area ratio
η	Efficiency
η	Lagrange multiplier
κ	Safety factor/margin
μ	Mach angle
ν	Prandtl–Meyer function
ϕ	Velocity potential
ρ	Mass density
σ	Yield strength
θ	Angle
ε	Structural mass fraction
ζ	Correction factor
ζ	Propellant mass fraction

SUBSCRIPTS

<i>1st</i>	First “booster” stage
<i>2nd</i>	Second “upper” stage
<i>b</i>	Burn duration
<i>bat</i>	Battery pack
<i>c</i>	Convergent section
<i>cc</i>	Combustion chamber
<i>char</i>	Characteristic curve
<i>d</i>	Divergent section
<i>e</i>	Energy
<i>e</i>	Nozzle exit
<i>ext</i>	External conditions
<i>EPFS</i>	Electropump feed system
<i>f</i>	Fuel
<i>gg</i>	Gas generator
<i>i</i>	Inflection
<i>i</i>	Nozzle inlet
<i>inj</i>	Injector
<i>inn</i>	Inner
<i>inv</i>	Inverter
<i>LV</i>	Launch vehicle
<i>m</i>	Material
<i>mot</i>	Electric motor
<i>n</i>	Nozzle
<i>o</i>	Oxidizer
<i>ori</i>	Orifice
<i>out</i>	Outer
<i>p</i>	Propellant
<i>p</i>	Pump
<i>pro</i>	Stage propellant
<i>prs</i>	Pressurant
<i>pu</i>	Pump assembly
<i>s</i>	Stay duration
<i>t</i>	Nozzle throat
<i>t</i>	Tank
<i>tc</i>	Thrust chamber
<i>tp</i>	Turbopump assembly

<i>tu</i>	Turbine assembly
<i>TPFS</i>	Turbopump feed system
<i>u</i>	Ullage
<i>w</i>	Wall

CONSTANTS

g_0	Standard gravity of Earth (= 9.80665 m/s ²)
R^*	Universal gas constant (= 8.314462618 J/K/mol)

1

INTRODUCTION

We began as wanderers, and we are wanderers still. We have lingered long enough on the shores of the cosmic ocean. We are ready at last to set sail for the stars.

— Carl Sagan, *Cosmos*

“Exploration is in our nature,” remarks Carl Sagan [1]. There have been humans for more than twenty thousand centuries, but only in the past century have we embarked on our cosmic voyage. We have sent dozens of ships to more than seventy worlds, and five spacecraft bound for the stars. Our present ships that ply the Keplerian trajectories to the planetary islands are “the harbingers, the vanguards of future human expeditions” to those unknown worlds. These voyages of exploration and discovery—emblematic of the epoch of sailing-ship voyages of exploration and discovery—are the latest in a long series that have characterized and distinguished human history.

Our essence of space exploration is not just as a scientific endeavour but as a fundamental biological necessity to explore and discover, to foster our sense of curiosity and wonder. And the instruments in enabling our zest for visiting those distant other worlds across the sea of space are rockets.

The rocket began, like the gunpowder that first powered it, in China where it was used for ceremonial and aesthetic purposes. Imported to Europe around the fourteenth century, it was applied to warfare, discussed in the late nineteenth century as a means of transportation to the planets by the Russian schoolteacher Konstantin Tsiolkovsky, and first developed seriously for high altitude flight by the American scientist Robert Goddard. The German V-2 military rocket (figure 1.1)

of World War II employed virtually all of Goddard's innovations and culminated in 1948 in the two-stage launching of the V-2/WAC Corporal combination to the then-unprecedented altitude of 400 kilometres.

In the 1950's, engineering advances organized by Sergei Korolov in the Soviet Union and Wernher von Braun in the United States, funded as delivery systems for weapons of mass destruction, led to the first artificial satellites. The pace of progress has continued to be brisk: crewed orbital flight; humans orbiting, then landing on the moon; and uncrewed spacecraft outward bound throughout the solar system. Many other nations have now launched spacecraft, including France, Japan, Germany, India and China, the society that invented the rocket in the first place.



Figure 1.1.: A render of the V-2
Credit: C. Stanley [2]

A rocket, working in accordance with Newton's third law of motion, obtains forward acceleration—thus generating thrust—from the rearward expulsion of matter at high velocities using its propulsion system. Based on the type of their energy source, propulsion systems may broadly be classified into thermal, chemical, electric and nuclear propulsion. In a chemical rocket propulsion system, the exhaust matter (also called reaction mass or working fluid) is generated by exothermic chemical reactions of the propellant(s), and is imparted with very high momentum through a supersonic nozzle. Depending on the nature of propellants used, chemical propulsion may comprise solid propellants, liquid propellants or both; liquid propulsion may further be classified into monopropellant and bipropellant systems. Now, bipropellant liquid rockets carry their own liquid oxidizer and liquid fuel which undergo a reduction–oxidation combustion process inside the combustion chamber of a thrust chamber, and have very high chemical-to-kinetic energy conversion efficiencies.

1.1 DESIGN OBJECTIVE

The design of a rocket propulsion system, unlike that of a standalone system, is intertwined with the overall development of a number of associated vehicle

systems and is influenced by a multitude of conditions and considerations: from the requirements needed to accomplish the mission to the rationalizations involved behind the development of each system and/or component. But perhaps the initial steps, and often the defining criteria, toward the preliminary design of a liquid propellant rocket engine stem from the objectives of the mission and the performance specifications of the system.

In a nutshell, a typical mission for our hypothetical small-lift orbital-class rocket would be to deliver a light payload into LEO. The two-stage launch vehicle is required to have a delta-v budget of 9500 m/s and a payload capacity of 200 kg. And we are required to preliminarily develop a “new generation” propulsion system that can fly such a mission.

In essence, the principal objectives of this project are to:

- Design a liquid rocket propulsion system for both the booster stage and the upper stage of a launch vehicle. The two rocket engines are obligated to be as similar as pragmatically possible, closely mirroring the design scheme of Rutherford on the Rocket Lab Electron or of Merlin on the SpaceX Falcon 9.
- Design a propellant feed system for the engine (after conducting a comparative study between turbopump systems and electropump systems).
- Design an injector assembly, together with its associated components such as propellant manifolds and injection elements, for the engine.

After some scrutiny into thrust metrics from extant rocket engines used on similar launch vehicles, we decide to target for a rated thrust of 30 kN from each engine. In addition, the outer diameter of our launch vehicle is capped at 1.25 m. While a preliminary study of a liquid propellant rocket engine can only include so much comprehensive analysis of every system and/or component the propulsion system integrates with, this project intends to cover the overall development of as many associated systems and/or components as theoretically applicable.

1.2 PROJECT MOTIVATION

But why? Why ought we to take up this project? What exactly is the societal significance behind studying small launchers?

On 28 September 2008, Falcon 1 by SpaceX lifted off from an unremarkable island in the Pacific and became the first privately-developed liquid-propelled launcher to

achieve orbit around the Earth. With the flights of Falcon 9 (figure 1.2) a few years later, SpaceX demonstrated the viability of reusable rockets, diminished the cost of accessing space, and ushered in a new era of space exploration in the process [4].

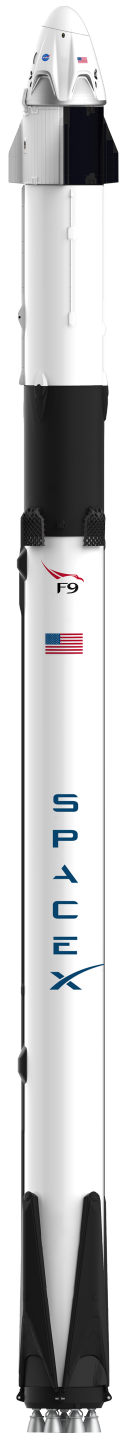


Figure 1.2.: SpaceX Falcon 9
Credit: SpaceX [3]

subsequently passed that encouraged private partners to operate their hardware in

The space age, however, was not always so privatization savvy [5] [6]. Ever since the V-2 back in 1944 became the first artificial object to touch space, rockets have primarily been built and operated by government space agencies. With the United States and the Soviet Union mired in the “space race” years later to achieve spaceflight superiority and be the first to conquer outer space through competitive technological dominance, there was little incentive to count cost as a factor for space exploration; national interest was all that mattered, since neither nation wanted to fall behind the other. The space race, which had its origins in the ballistic missile-based nuclear arms race between the two nations, started effectively with the launch of Sputnik 1 into an elliptical orbit around the Earth in 1957, climaxed perhaps with the landing of humans on the surface of the Moon with the Apollo 11 mission in 1969, and, owing partly to declining political support, ended eventually with the flight of the collaborative Apollo–Soyuz crewed mission between the two superpowers in 1975.

A consequence of the space race was the involvement of private organizations to build hardware for the government space agencies. Besides, a steady shift in paradigm from militaristic and political impetus to scientific and technological progression over due course of time did warrant the need to offer low launch prices to deliver payloads into orbit. In the US, a law was

space as well as to conduct their own launch services, thereby paving the way for the establishment of a billion-dollar commercial spaceflight industry [5]. Over on the Soviet side, design bureaus affiliated with the state spearheaded the research and development of pioneering space technologies. Likewise, the ESA created ArianeSpace to undertake spacecraft launches for and promote joint space exploration between the member European nations. This ultimately resulted in a myriad of firsts with regard to the privatization of spaceflight—from the first commercial satellite to the first launch vehicle.

With the emergence of commercial spacecraft (mostly through communications satellites), the cost of accessing space began to dominate the market competition for the first time [4]. A number of launchers of varying capabilities have therefore been developed across the globe to cater to the ever-increasing market demands. The partially reusable Space Shuttle by NASA is one such launcher system. The price of launching a payload to LEO has, owing to the competitiveness, declined substantially over time: from \$54500 per kilogram with the Space Shuttle during its operation to \$2720 per kilogram with the Falcon 9 today [8]. And decreasing costs of launch services, and of space hardware in general, have enticed new enterprises into this market; further, companies in a variety of industries have begun leveraging space accessibility and satellite technology to drive innovation and efficiency in their earth-bound products and services.

In more recent times, space agencies together with commercial consortia have begun the privatization of transporting cargo and crew to the ISS as well as launching missions to the Moon. Through cost reduction and breakthrough innovation, these new offerings have democratized space exploration and knocked down the barriers to space [9]—from reusable rockets and commercial space tourism to lunar habitats and constellations of small satellites.



Figure 1.3.: Rocket Lab Electron
Credit: Rocket Lab
[7]

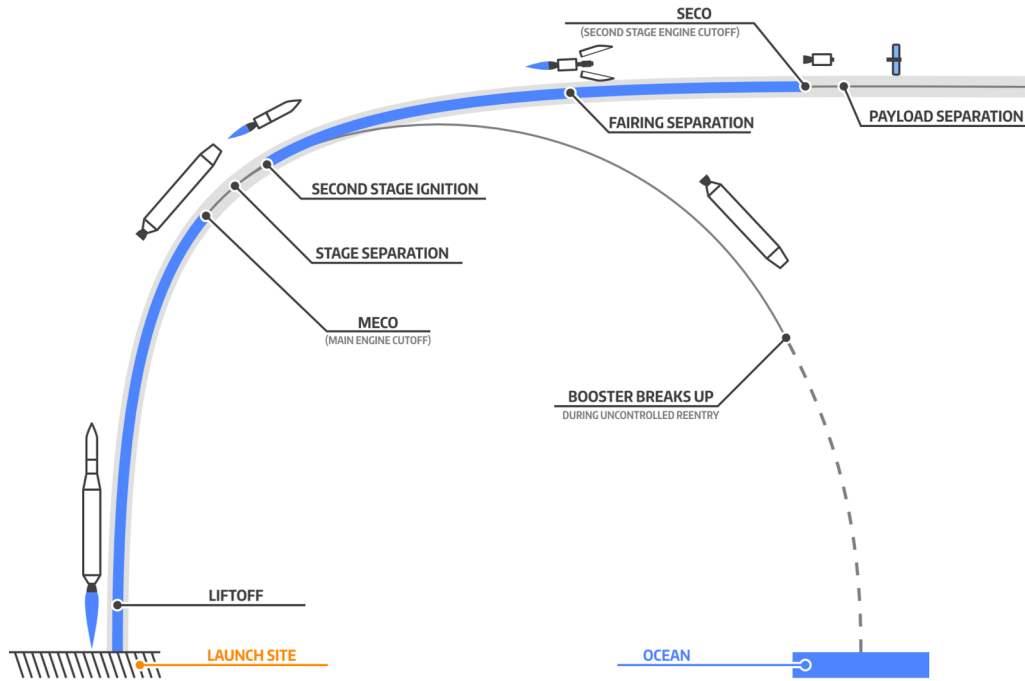


Figure 1.4.: A typical flight profile for an orbital-class twin-stage expendable launch vehicle configuration.

Image credit: John Gardi [10]

On 21 January 2018, Electron (figure 1.3) by Rocket Lab deployed three CubeSats into orbit and helped establish an expanding market for the commercial use of space. Rocket Lab categorically targeted the SmallSat industry by launching small satellites—which hitherto had only been launched as secondary payloads—as primary payloads into tailored orbits at flexible mission schedules [4].

Now, the secondary payload paradigm does not provide the specificity necessary for many sophisticated small satellites that require quite unique mission designs [5] [6]. To remedy this, while spurred by the emergence of such companies as SpaceX and Rocket Lab, a number of companies are currently developing (or have only recently developed) small-lift twin-stage launchers to cater to the increasingly specific demands of the small satellite market. With the small satellite economy skyrocketing, Virgin Orbit has flown LauncherOne to deploy ten CubeSats into orbit, albeit from air. Rocket 3.3 from Astra has launched a test payload for the United States Space Force. Alpha from Firefly Aerospace has, as of now, performed its first partially successful orbital launch. Needless to mention are the numerous launchers in various stages of their development cycles, viz. Spectrum from Isar



Figure 1.5.: Electron ready on the pad to launch on the Virginia Is For Launch Lovers mission for one of its commercial customers.
Image credit: Rocket Lab [7]

Aerospace, RFA One by Rocket Factory Augsburg, Prime from Orbex, Miura 5 by PLD Space, Skyrora XL from Skyrora, Terran 1 by Relativity Space, to name some [6]. Not only does such a fierce competition amongst the companies dwindle the cost of accessing space, but more significantly it drives innovation at quite unprecedented a pace—by developing new technologies and pushing the boundaries of what is considered conventional.

A breakthrough in inventing that innovation is employing advanced propulsion technologies to design a “new generation” liquid rocket propulsion system. Using the combination of liquid oxygen (LOX) and liquid methane (LCH₄) would be one instance. Another instance would be utilizing an electric pump feed system to



Figure 1.6.: Four commercial small satellites by Axelspace called GRUS awaiting shipment for launch, with each in the 200 kilogram mass category.
Image credit: Axelspace [11]

power the rocket engine. Extensive research and development are currently being performed on both these technologies throughout the rocket industry. Leading the development of LCH₄/LOX engines are SpaceX with the Raptor, Blue Origin with the BE-4, by Relativity Space with the Aeon, among others. Likewise, Rocket Lab and Astra have actively developed electropump systems for their Rutherford and Delphin rocket engines respectively. Yet no engine for any launcher has thus far been announced that employs both these technologies together.

Why is that the case? How good is a methane-oxygen-powered rocket engine? What edge does an electric-pump-fed engine cycle provide? Is a propulsion system employing these two techniques objectively better for a small-lift orbital-class rocket such as ours? These are the questions which we intend to address in our study.

With the success of Electron within the light-payload launch market as an exemplar, we strive to emulate—or rather to better—the precedent Electron has set [7]. Consequently, we target the commercial small satellite industry and plan for a payload mass between 150 kg and 250 kg for our hypothetical rocket. And accordingly, we aim for a vehicle diameter of about 1.2 m and a rated thrust of around 25 kN per engine system in our study.

Now, even though the reusability of rocket boosters and additive manufacturing of rocket components are active areas of investigation within the rocket industry at present, we do not delve into those topics in this project. A typical flight profile for an expendable orbital-class twin-stage launch vehicle is demonstrated in figure 1.4, wherein: after a few minutes of flight post liftoff, the first stage shuts down its engines, separates from the vehicle and drops back to Earth; soon thereafter, the second stage commences engine ignition, discards the fairing, deploys the payload at its targeted trajectory and velocity, and ultimately detaches away from the payload to eventually burn up in the atmosphere. This is the profile we plan our rocket to follow. In figure 1.5, Electron stands ready to launch on its 33rd (and the latest) mission called “Virginia Is For Launch Lovers” for a commercial customer. Figure 1.6 shows the example of a typical commercial small satellite in the 200 kilogram mass category, the type our payload will likely comprise of. Figure 1.7 presents an overview along with a few key specifications of the Electron.

1.3 THESIS OUTLINE

This chapter puts forth a mission definition for us, the objectives of this project, and the motivation behind our study.

Chapter two defines the fundamental principles of liquid rocket propulsion systems: from performance parameters and quasi-one-dimensional flow processes for an ideal rocket engine analysis to limitations and correction factors for a real propulsion system operation. All crucial equations used in the theoretical calculation of engine performance are presented as well.

The third chapter touches on a few fundamental aspects of propellant selection, and examines the myriad implications of bipropellant mixture characteristics on the design criteria of a rocket engine. A suite of performance parameters (such as specific impulse, mixture ratio, chamber pressure and temperature) obtained from the combustion of LOX with LH₂, RP-1 and LCH₄ are analysed in detail. This serves to choose the best bipropellant combination for our mission.

Chapter four delves into the functional details of pressure and pump feed systems, and investigates the practicality of each type of feed system for the operational regime of our engine. As a result, propellant pressures inside the combustion chamber as well as within the feed line are settled on. The selection criteria between turbopump and electropump systems are established on a multitude of component characteristics exclusive to the feed system, such as gas generator, battery pack, and



Figure 1.7.: An overview along with some key specifications for the different stages of the Electron launch vehicle.
Image credit: Rocket Lab [7]

the like. Eventually, mass fractions of the feed systems are estimated as functions of engine operation duration along with technological maturity of today.

The fifth chapter incorporates design methodologies to preliminarily design two thrust chamber versions for our rocket—a sea-level variant for the booster stage and a vacuum-optimized variant for the upper stage. After determining the expansion ratios and correcting the performance parameters, the dimensions of the thrust chamber are ascertained. An in-depth analysis of the convergent-divergent nozzle contour is performed based on TIC, TOC, TOP, and the method of characteristics techniques. Ultimately, the design configuration of the combustion chamber is presented.

Chapter six initially addresses the topic of thermal management together with the selection of compatible wall materials for our engine. As a consequence, comprehensive cooling procedures are employed for both the thrust chamber variants. The process of propellant metering, injection, atomization, vaporization and mixing for effective combustion are finally looked into, which culminates in the design of an injector assembly.

The last chapter lays out the conclusions of our study, discusses the circumstances wherein our design of methane-oxygen-powered electric-pump-fed liquid rocket propulsion system has an edge, and sets forth the opportunities for improvement of this project as future work prospects.

2

FUNDAMENTALS OF ROCKET PROPULSION

In liquid rocket propulsion systems, the mathematical tools necessary to analyse performance and to ascertain the myriad parameters for thrust chamber operations stem from the principles of gas dynamics and thermodynamics processes. These relations allow the determination of combustion chamber and nozzle shape and size for a specific performance requirement, and apply to any propulsion system that utilizes gas expansion as the mechanism for ejecting matter at high velocities to generate thrust. This chapter is an introduction to the theory of gas properties in chemical rocket propulsion systems, and identifies the relevant thermochemical fundamentals, basic analytical approaches and key equations.

2.1 IDEAL ROCKET PROPULSION SYSTEM

The concept of an ideal rocket propulsion system is useful because the mathematical relationships defining the primary underlying thermodynamic principles describe “quasi-one-dimensional nozzle flows, which represent an idealization and simplification of the full two-dimensional or three-dimensional equations of real aerothermochemical behaviour” [12, p. 46]. These descriptions are adequate to obtain useful solutions for preliminary rocket propulsion designs, and compute results that are usually only within 1 to 6% of their measured actual performance figures [12]. The ideal rocket parameters used in the design of new rocket propulsion systems are often modified by appropriate correction factors so as to get theoretical results as close to the empirical values.

The following assumptions define the operation of an ideal rocket propulsion unit [12, p. 46]:

- The working fluid (which usually consists of chemical reaction products) is homogeneous in composition.
- All the species of the working fluid are treated as gaseous. Any condensed phases (liquid or solid) add a negligible amount to the total mass.
- The working fluid obeys the perfect gas law.
- There is no heat transfer across any and all gas-enclosure walls; therefore, the flow is adiabatic.
- There is no appreciable wall friction and all boundary layer effects may be neglected.
- There are no shock waves or other discontinuities within the nozzle flow.
- The propellant flow rate is steady and constant. The expansion of the working fluid is uniform and steady, without gas pulsations or significant turbulence.
- Transient effects (i.e., startup and shutdown) are of such short duration that may they be neglected.
- All exhaust gases leaving the rocket nozzles travel with a velocity parallel to the nozzle axis.
- The gas velocity, pressure, temperature, and density are all uniform across any section normal to the nozzle axis.
- Chemical equilibrium is established within the preceding combustion chamber and gas composition does not change in the nozzle (i.e., frozen composition flow).
- Ordinary propellants are stored at ambient temperatures. Cryogenic propellants are at their boiling points.

These assumptions allow for the derivation of compact, quasi-one-dimensional set of equations for the ideal operation of a rocket propulsion system.

2.2 PERFORMANCE PARAMETERS

2.2.1 Thrust

The quintessential parameter defining the performance of a rocket engine is the propulsive force or thrust it generates.

The total thrust (in N) produced by a propulsion system is given as

$$F = \dot{m} v_e + A_e (P_e - P_{ext}) \quad (2.1)$$

The term $\dot{m} v_e$ represents momentum thrust (given by the product of the propellant mass flow rate \dot{m} and the average exhaust velocity of the reaction mass at nozzle exit v_e), and the term $A_e (P_e - P_{ext})$ denotes pressure thrust (given by the product of the cross-sectional area of the nozzle exit A_e and the difference between the exit pressure of the combustion fluid P_e and the external pressure of the surrounding fluid P_{ext}). While the momentum thrust is constant during steady operation of a thrust chamber, the pressure thrust does vary with any variation in the ambient pressure around the thrust chamber, and can amount from 10 to 30% of the overall thrust during the ascent of a rocket [13].

At altitudes where the ambient pressure is higher than the exhaust pressure, the pressure thrust term is negative and contributes to a lower-than-rated overall thrust; the nozzle in this condition is said to be over-expanded (and creates shock diamonds in the exhaust plume, thus losing efficiency). In contrasting conditions where the ambient pressure is lower than the exhaust pressure, the pressure thrust term, although positive, yet again contributes to a lower overall thrust; the nozzle is said to be under-expanded (and ejects the exhaust jet without complete expansion, thus again losing efficiency).

When the exhaust pressure equals the ambient pressure, the pressure thrust term becomes zero, and the nozzle is said to operate at its optimum expansion ratio. This condition of perfect expansion maximizes thrust (and thereby efficiency) from the nozzle for a given ambient pressure, and is only achieved at a particular altitude during the upward flight of a launch vehicle.

The total thrust from an optimally-expanded nozzle, therefore, can be expressed as

$$F = \dot{m} v_e \quad (2.2)$$

2.2.2 Specific Impulse

The fundamental metric determining the efficiency of a rocket engine is the specific impulse of the propulsion system. It directly contributes to the change in velocity (Δv) of a rocket stage at propellant burnout and has a pronounced effect on mass of the payload: the higher the specific impulse, the less is the propellant mass required to provide the desired impulse.

Expressed in units of time (in s), specific impulse is defined as the ratio of the thrust generated to the weight flow rate \dot{w} of the ejected propellant.

$$I_s = \frac{F}{\dot{w}} = \frac{F}{\dot{m} g_0} \quad (2.3)$$

The expression 2.3 can be formulated in terms of exhaust velocity v_e , nozzle exit area A_e , pressure difference at the nozzle exit ($P_e - P_{ext}$), and mass flow rate \dot{m} as follows

$$I_s = \frac{v_e}{g_0} + \frac{A_e}{\dot{m} g_0} (P_e - P_{ext}) \quad (2.4)$$

Specific impulse, when defined as the total impulse delivered per unit mass of the propellant consumed (or as thrust per unit propellant mass flow rate), does in essence represent the effective exhaust velocity of the expelled propellant relative to the rocket, and can thus have units of speed (in m/s).

$$I_s = \frac{I_t}{m_p} = \frac{F}{\dot{m}} \quad (2.5)$$

The specific impulse of an engine operating in a vacuum environment is called its vacuum specific impulse, and is denoted as I_{svac} .

2.2.3 Effective Exhaust Velocity

The efflux of propellants from a thrust chamber creates a non-uniform velocity profile across the exit cross sectional area of the nozzle. Because an accurate measurement of the actual exhaust velocity is difficult, “a uniform axial velocity is assumed for all calculations which employ one-dimensional problem descriptions” [12, p. 27]. Effective exhaust velocity, thus, represents “an average or mass-equivalent velocity” [12, p. 28] at which the exhaust jet is ejected from the thrust chamber, and can be expressed as

$$\begin{aligned} c &= I_s g_0 \\ &= v_e + \frac{A_e}{\dot{m}} (P_e - P_{ext}) \end{aligned} \quad (2.6)$$

Presence of the external pressure dependent term in the equation 2.6 implies that the effective exhaust velocity equals the average actual nozzle exhaust velocity v_e only for an optimum expansion ratio condition.

Effective exhaust velocity may further be defined as the product of characteristic velocity c^* and thrust coefficient C_f .

$$c = c^* C_f \quad (2.7)$$

2.2.4 Characteristic Velocity

Characteristic velocity reflects the design characteristics of a thrust chamber independent of the nozzle performance, and represents the effective energy of the propellant combustion within the combustion chamber. It is not a physical velocity but a measure of the combustion performance—propellant properties and combustion characteristics—of a thrust chamber, and thus can be used as a convenient parameter when comparing different propellant combinations for propulsion systems [13].

Characteristic velocity has units of speed (in m/s) and may be defined as

$$c^* = \frac{P_{cc} A_t}{\dot{m}} \quad (2.8)$$

The equation 2.8 indicates that the lower the rate of propellant consumption in order to maintain the required nozzle stagnation pressure, the higher is the energy (and efficiency) of the combustion process and thereby the higher is the value of characteristic velocity.

Characteristic velocity may again be determined from the measurements of specific heat ratio k , gas constant R , and combustion chamber temperature T_{cc} as follows

$$c^* = \frac{\sqrt{k R T_{cc}}}{k \sqrt{\left(\frac{2}{k+1}\right)^{\frac{(k+1)}{k-1}}}} \quad (2.9)$$

In the equation 2.9, specific heat ratio k is the ratio of heat capacity at constant pressure c_P to heat capacity at constant volume c_V , and gas constant R is the universal gas constant R^* ($= 8.314462618 \text{ J/K/mol}$ [14]) divided by the effective molecular mass \mathfrak{M} of the fluid (in g/mol).

2.2.5 Thrust Coefficient

Thrust coefficient reflects the design characteristics of a de Laval nozzle, and represents the expansion properties of the combustion fluid within the supersonic

nozzle of a thrust chamber. It measures the amplification of thrust generated due to the reaction mass expansion through the nozzle of a thrust chamber regardless of its combustion chamber characteristics, and is a convenient parameter for estimating the effects of chamber pressure and/or altitude variation on a given nozzle configuration [12].

Thrust coefficient is a dimensionless quantity with values ranging from just under 1.0 to roughly about 2.0 [12], and may be defined as

$$C_f = \frac{F}{P_{cc} A_t} \quad (2.10)$$

Thrust coefficient may again be formulated in terms of specific heat ratio k , combustion chamber pressure P_{cc} , exit pressure P_e , external pressure P_{ext} , and nozzle expansion area ratio ϵ as follows

$$C_f = \sqrt{\left(\frac{2k^2}{k-1}\right)\left(\frac{2}{k+1}\right)^{\left(\frac{k+1}{k-1}\right)}\left[1 - \left(\frac{P_e}{P_{cc}}\right)^{\left(\frac{k-1}{k}\right)}\right] + \left(\frac{P_e - P_{ext}}{P_{cc}}\right)\epsilon} \quad (2.11)$$

In the equation 2.11, expansion ratio ϵ is the ratio of exit area A_e to throat area A_t of a nozzle.

Combining the equations 2.10 and 2.11, thrust can now be expressed as

$$F = P_{cc} A_t \sqrt{\left(\frac{2k^2}{k-1}\right)\left(\frac{2}{k+1}\right)^{\left(\frac{k+1}{k-1}\right)}\left[1 - \left(\frac{P_e}{P_{cc}}\right)^{\left(\frac{k-1}{k}\right)}\right] + A_e (P_e - P_{ext})} \quad (2.12)$$

The equation 2.12, known as the ideal thrust equation, shows that thrust is proportional to throat area and chamber pressure, and is a function of the pressure ratio across the nozzle, the pressure thrust component and specific heat ratio.

2.2.6 Average Exhaust Velocity

The theoretical exhaust velocity of the reaction mass ejected from an ideal thrust chamber can be expressed as

$$v_e = \sqrt{R^* \frac{T_{cc}}{\mathfrak{M}} \left(\frac{2k}{k-1}\right) \left[1 - \left(\frac{P_e}{P_{cc}}\right)^{\left(\frac{k-1}{k}\right)}\right]} \quad (2.13)$$

The equation 2.13 indicates that exhaust velocity is a function of pressure ratio P_{cc}/P_e across the nozzle and specific heat ratio k , and is directly proportional to the absolute temperature at the nozzle inlet T_{cc} and inversely proportional to the molecular mass of the combustion fluid \mathfrak{M} . With other parameters remaining constant, an increase in the ratio T_{cc}/\mathfrak{M} will increase the exhaust velocity thereby increasing the specific impulse of the propulsion system.

2.2.7 Propellant Mass Flow Rate

Now, the theoretical mass flow rate of propellants (in kg/s) exhausted through a thrust chamber operating under ideal conditions can be expressed as

$$\dot{m} = P_{cc} A_t \sqrt{\frac{k \left(\frac{2}{k+1}\right)^{\frac{(k+1)}{k-1}}}{R T_{cc}}} \quad (2.14)$$

And for a propellant mass mixture ratio O/F , the respective oxidizer and fuel mass flow rates equal

$$\dot{m}_o = \dot{m} \frac{(O/F)}{(O/F) + 1} \quad (2.15a)$$

$$\dot{m}_f = \dot{m} \frac{1}{(O/F) + 1} \quad (2.15b)$$

The respective mass of the oxidizer and the fuel can be determined from the product of their mass flow rates and the nominal burn time t_b of the rocket engine

$$m_o = \dot{m}_o t_b \quad (2.16a)$$

$$m_f = \dot{m}_f t_b \quad (2.16b)$$

2.2.8 Density Impulse

The density impulse “expresses the total impulse delivered per unit volume of the propellant” [13, p. 19], and is defined as the product of specific weight d of a propellant combination and the specific impulse. Denoted as I_{sd} , it is an important measure in launch vehicle design since a lower density impulse implies the need for a larger tank volume to store the propellant, which in turn has a detrimental effect on the mass ratio of a rocket.

$$I_{sd} = I_s d \quad (2.17)$$

2.3 QUASI 1-D FLOW PARAMETERS

2.3.1 Isentropic Flow Condition

For any quasi-one-dimensional flow process undergoing isentropic expansion, the following relations hold true between two nozzle sections x and y

$$\frac{T_x}{T_y} = \left(\frac{P_x}{P_y} \right)^{\left(\frac{k-1}{k}\right)} = \left(\frac{V_y}{V_x} \right)^{(k-1)} \quad (2.18)$$

Stagnation conditions arise when the flow is stopped isentropically inside a combustion chamber, and the local temperatures and pressures approach the stagnation temperatures and pressures.

The Mach number M is a dimensionless flow parameter used to locally define the ratio of the flow velocity v to the local acoustic velocity a , and is given as

$$M = \frac{v}{a} = \frac{v}{\sqrt{k R T}} \quad (2.19)$$

Now, the relations between Mach number with stagnation temperature and stagnation pressure are written as

$$T_0 = T \left(1 + \frac{1}{2} (k - 1) M^2 \right) \quad (2.20)$$

$$P_0 = P \left(1 + \frac{1}{2} (k - 1) M^2 \right)^{\left(\frac{k}{k-1}\right)} \quad (2.21)$$

The nozzle area ratio for isentropic flow in terms of Mach number at two locations x and y within the nozzle can be written as

$$\frac{A_x}{A_y} = \frac{M_y}{M_x} \sqrt{\left(\frac{1 + \left(\frac{k-1}{2}\right) M_x^2}{1 + \left(\frac{k-1}{2}\right) M_y^2} \right)^{\left(\frac{k+1}{k-1}\right)}} \quad (2.22)$$

2.3.2 Nozzle Throat Conditions

From the above relations, the temperature T_t , pressure P_t and specific volume V_t at the throat can be expressed in terms of the respective parameters from the

combustion chamber as follows

$$T_t = T_{cc} \left(\frac{2}{k+1} \right) \quad (2.23)$$

$$P_t = P_{cc} \left(\frac{2}{k+1} \right)^{\left(\frac{k}{k-1}\right)} \quad (2.24)$$

$$V_t = V_{cc} \left(\frac{k+1}{2} \right)^{\left(\frac{1}{k-1}\right)} \quad (2.25)$$

Likewise, the throat velocity v_t can be written as

$$v_t = \sqrt{\left(\frac{2k}{k+1} \right) R T_{cc}} = \sqrt{k R T_t} = a_t \quad (2.26)$$

By definition, the sonic velocity a_t , or the Mach number, at the nozzle throat equals 1.0.

Now, for any region y downstream of the throat, the following relations, expressed in terms of pressure ratio, hold true

$$T_y = T_{cc} \left(\frac{P_y}{P_{cc}} \right)^{\left(\frac{k-1}{k}\right)} \quad (2.27)$$

$$V_y = V_{cc} \left(\frac{P_{cc}}{P_y} \right)^{\left(\frac{1}{k}\right)} \quad (2.28)$$

$$\frac{v_y}{v_t} = \sqrt{\left(\frac{k+1}{k-1} \right) \left(1 - \left(\frac{P_y}{P_{cc}} \right)^{\left(\frac{k-1}{k}\right)} \right)} \quad (2.29)$$

$$\begin{aligned} \frac{A_t}{A_y} &= \left(\frac{k+1}{2} \right)^{\left(\frac{1}{k-1}\right)} \left(\frac{P_y}{P_{cc}} \right)^{\left(\frac{1}{k}\right)} \sqrt{\left(\frac{k+1}{k-1} \right) \left(1 - \left(\frac{P_y}{P_{cc}} \right)^{\left(\frac{k-1}{k}\right)} \right)} \\ &= \frac{V_t v_y}{V_y v_t} \end{aligned} \quad (2.30)$$

2.4 REAL ROCKET PROPULSION SYSTEM

The assumptions defining the operation of an ideal rocket propulsion system allow for the analysis and design a real rocket propulsion unit using relatively

simple mathematical approximations and relations. In order to represent a better simulation of energy losses or physical and chemical phenomena, and contain more complex theoretical descriptions, it is possible either to use empirical correction factors based on experimental data or to implement more accurate algorithms besides the above assumptions. Compared to ideal thrust chambers, real thrust chambers suffer from numerous operational losses, some of which are mentioned below [12, p. 81]:

- Divergence of the flow in the nozzle exit sections is a loss that varies as a function of the cosine of the divergence angle for conical nozzles. These losses can be reduced with bell-shaped nozzle contours.
- Low nozzle contraction ratios cause pressure losses in the chamber and slightly reduce the thrust and exhaust velocity.
- The lower velocities at the wall boundary layers reduce the effective average exhaust velocity by 0.5 to 1.5%.
- Solid particles and/or liquid droplets in the gas may cause losses of perhaps up to 5% (depending on particle size, shape and percentage).
- Unsteady combustion and/or flow oscillations may result in small losses.
- Chemical reactions within nozzle flows change gas composition and gas properties, amounting to typically a 0.5% loss.
- Chamber pressures and overall performance are lower during start and stop transient operations.
- Any gradual erosion of the throat region increases its diameter by perhaps 1 to 6% during operation with uncooled nozzle materials. This, in turn, reduces the chamber pressure and thrust by about 1 to 6%.
- Nonuniform gas compositions may reduce performance due to incomplete mixing or incomplete combustion.
- Real gas properties may noticeably modify gas composition, that is, actual values of k and \mathfrak{M} cause a small loss in performance by about 0.2 to 0.7%.

When the expansion of the working fluid in a nozzle is sufficiently rapid, its chemical composition may be assumed as invariant throughout the nozzle, meaning, there are no chemical reactions or phase changes and the reaction products composition at the nozzle exit are identical to those of the chamber exit. Such composition

results are known as *frozen equilibrium* rocket performance. This approach, being the simplest, tends to underestimate the system's performance by 1 to 4% [12].

Instantaneous chemical equilibrium among all molecular species may be significant in certain circumstances under the continuously variable pressure and temperature conditions of the nozzle expansion process. Product compositions do shift in this case because the chemical reactions and phase change equilibria occurring between gaseous and condensed phases in all exhaust gas species are fast compared to their nozzle transit time; this results in different gas composition mass fractions at the chamber and nozzle exits. The composition results so calculated are called *shifting equilibrium* performance. This analysis, being more complex, usually overstates real performance values such as c^* or I_s by 1 to 4%.

Correction factors based on experimental data from extant rocket propulsion systems are implemented during the preliminary analysis and design of new rocket propulsion systems in order to account for much of the above non-ideal phenomena [12], such as internal and/or kinetic energy losses, imperfect mixing and/or combustion, heat transfer, friction, etc.

The thrust correction factor ζ_{C_f} ($= F_a/F_i$) is determined from the ratio of thrust measurements to its corresponding ideal values. The c^* correction factor ζ_{c^*} represents a combined effectiveness of the combustion chamber and the injector design while the C_f correction factor ζ_{C_f} represents the effectiveness of the nozzle design at its operating conditions. The discharge correction factor ζ_m ($= \dot{m}_a/\dot{m}_i$) can be determined from the ratio of mass flow rate measurements with the corresponding theoretical values, and is, because of compressible flow properties, somewhat greater than 1.0 [12].

Determining the above correction factors paves the way for estimating efficiencies such as those of the exhaust velocity, specific impulse or of the nozzle itself, and for calculating parameters such as the actual throat and exit areas or the local stagnation temperatures and pressures of the working fluid across the thrust chamber.

2.5 ENGINE NOMENCLATURE

The fundamental components/sections of a thrust chamber are the injector, the combustion chamber, and the (convergent-divergent) nozzle, which in turn is segmented into the inlet, the throat, and the exit. The schematic and convention

our engine design parameters follow are illustrated in figure 2.1 and presented in table 2.1 below.

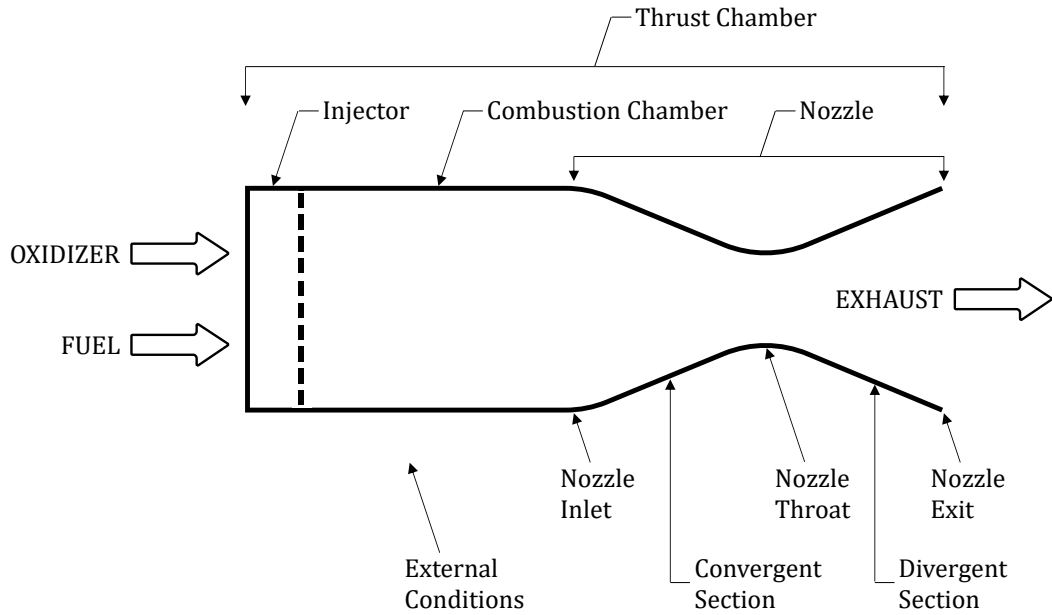


Figure 2.1.: Schematic of a typical liquid propellant rocket engine together with its major components/sections.

Table 2.1.: Convention used for the design parameters of our liquid propellant rocket engine.

Thrust Chamber	<i>tc</i>
Injector	<i>inj</i>
Combustion Chamber	<i>cc</i>
Nozzle	<i>n</i>
Inlet	<i>i</i>
Throat	<i>t</i>
Exit	<i>e</i>
Convergent section	<i>c</i>
Divergent section	<i>d</i>
External conditions	<i>ext</i>
First stage	<i>1ST</i>
Second stage	<i>2ND</i>

3

LIQUID PROPELLANTS

A propellant is largely defined as any substance that undergoes chemical changes and thermodynamical processes within the thrust chamber of a propulsion system in order to generate thrust. A *liquid rocket* is primarily distinguished as a monopropellant system or a bipropellant system according to the number of liquid propellants it employs for achieving propulsion. While a monopropellant system provides propulsive reaction from the decomposition of a single propellant, a bipropellant system comprises an oxidizer and a fuel, and produces resultant thrust from the combustion of the propellant mixture. Based on the temperature range of its storage, a propellant can be classified as a *cryogenic* or a *storable* liquid. Depending on the process of its ignition, a propellant mixture can be classified as a *hypergolic* or a *nonhypergolic* combination. And as a function of its application, a liquid rocket engine may further be categorized as a boost propulsion system (used predominantly for imparting significant total impulses and velocity changes to payloads) or an auxiliary propulsion system (used principally for attitude control, orbit maintenance and minor trajectory corrections).

3.1 PROPELLANT CHARACTERISTICS

The choice of propellants for a liquid bipropellant system has paramount implications on design criteria of the rocket engine and performance metrics of the overall rocket, and significantly influences such considerations as production, storage, handling, cost and even mission compatibility. When it comes to performance, there is no one propellant combination that has an absolute advantage over another combination: selection of a propellant is therefore a compromise between some important aspects and some desirable features.

3.1.1 Important Aspects & Desirable Features

Thrust, as expressed in the equation 2.2, has been defined as the product of propellant mass flow rate and average exhaust velocity. And as specified in the equations 2.14 and 2.13 respectively, mass flow rate and exhaust velocity are in turn dependent on a combination of thrust chamber characteristics and thermochemical reaction properties. With other parameters remaining constant and for a given rate of consumption of propellants, therefore, an increase in the ratio T_{cc}/\mathfrak{M} does result in an increased overall thrust. Because exhaust velocity is directly proportional to combustion chamber temperature and inversely proportional to effective molecular mass of the exhaust jet, a propellant combination that generates the highest adiabatic flame temperature and/or produces the lowest average molecular weight of the combustion products is usually preferred. Additionally, a bipropellant mixture delivering a low specific heat ratio enhances the performance parameters of the rocket engine and is thus favoured [13].

In addition to the above propellant characteristics, there are numerous physical properties which, although don't have any direct consequence on flight performance parameters, are yet of considerable importance during the design of a rocket engine. One such property is the propellant's specific gravity. The higher the specific gravity of a propellant is, the smaller is the volume of tank required for a certain mass of the propellant, the lower, therefore, get the vehicle's structural mass and aerodynamic drag, and the higher, consequently, become the delta-v and payload carrying capacity of the rocket [12]. Moreover, increasing the propellant's density allows for an increase in its mass flow rate, which yet again enables increases in the rocket engine's combustion chamber pressure, total impulse, and thrust. Likewise, heat transfer properties such as high specific heat, high thermal conductivity, low freezing point and high boiling point are of crucial importance for a propellant when it serves as the coolant fluid in a regeneratively cooled thrust chamber. Furthermore, a propellant with low vapour pressure and low viscosity permits effective pump feed system designs and minimizes pressure drops through the plumbing system.

3.1.2 Classification of Propellants

A hypergolic propellant combination is one where the oxidizer and the fuel ignite spontaneously upon contact, and thus do not require any source of ignition after injection for their combustion. While enabling rocket engine designs with great simplicity and reliability, these propellants usually are rather difficult to handle owing to their extreme corrosivity, toxicity and oftentimes carcinogenicity [15]. A

few commonly used *hypergols* include oxidizers like hydrogen peroxide, dinitrogen tetroxide (NTO) and inhibited red fuming nitric acid (IRFNA), and fuels like hydrazine, monomethylhydrazine (MMH) and unsymmetrical dimethylhydrazine (UDMH). Hypergolic propellants typically yield specific impulses between 260 s and 290 s under optimum conditions [12] [13].

Cryogenic propellants in essence are liquefied gases with extremely low boiling points (from -140°C to -260°C) under ambient pressure conditions [13]. And because of such low temperatures, handling and storing these propellants can have certain inherent difficulties: *cryogenics* necessitate elaborate procedures in order to minimize losses due to propellant boiloff. Propellant tanks and plumbing systems, therefore, employ insulating systems to keep the propellants cold and venting systems to dispose of boiloff vapours—two critical measures which, besides adding complexity, increase the inert mass of the rocket. These drawbacks, however consequential, are unqualifiedly eclipsed by high specific impulse and thereby high overall vehicle performance that cryogenic propellants offer as compared to most other storable propellants [15] [16]. Using, for instance, liquid oxygen (LOX) in conjunction with liquid hydrogen (LH₂) can yield specific impulse as high as 465 s under the right circumstances [17] [18]. Combining LOX with liquid methane (LCH₄) is another similar mixture with highly desirable performance parameters [12] [13]. Oftentimes, a non-cryogenic fuel like Rocket Propellant 1 (RP-1) is paired with LOX to produce a combination that yet again delivers satisfactorily high engine performance [12] [13].

3.1.3 Propellant Selection Criteria

In a nutshell, the most important aspects and desirable features used in the selection of liquid propellants have been listed below [13, p. 19], order of importance of which may vary as a function of the application:

- High chemical energy content per unit mass of propellant mixture consumed for higher overall thrust.
- Low molecular mass of the combustion or decomposition products for higher specific impulse.
- High density impulse (total impulse/volume) for minimizing the mass and size of propellant tanks and feed systems.
- Optimum combination of high specific heat, high thermal conductivity and high critical temperature for propellants used as thrust chamber coolants.

- Low viscosity for minimizing pressure drops through feed system and injector.
- Low vapor pressure for low tank mass and low net positive pump suction head requirement.
- Low freezing point to facilitate engine operation at low temperature.
- Stability of combustion.
- Ease of ignition.
- Availability.
- Cost.

3.2 CANDIDATE PROPELLANTS

Having touched on a few fundamental factors influencing the selection of propellants for a liquid rocket propulsion system, this project aims to take propellant combinations that are nonhypergolic and preferably cryogenic in nature into consideration. A few candidate propellants, along with a handful of their pros and cons, have therefore been looked at below.

3.2.1 Liquid Oxygen (LOX)

Among the most widely used oxidizers, liquid oxygen has (at different times throughout history) been combined with such fuels as liquid hydrogen, petroleum derivatives like gasoline, JP-4, LNG and RP-1, organic compounds like methane, dimethoxymethane, methanol, ethanol, ethylene and methylamine, as well as even ammonia, hydrazine, UDMH and hydyne [19]. Being fairly cryogenic (with a normal boiling point of 90.20 K or -182.95°C [20]), LOX cannot be used in applications necessitating storage of the propellant for extended lengths of time. Notwithstanding the drawback, LOX has some quite advantageous properties to offer. It is a stable, non-corrosive and non-toxic fluid that supports combustion vigorously despite itself being non-combustible [12]. It has low molecular mass (of 31.999 g/mol), high specific gravity (of 1.142), low vapour pressure, low viscosity, and delivers relatively high performance with most fuels [20] [21] [22].

We, therefore, use liquid oxygen as the oxidizer of choice in the design of our propulsion system. Doing so, however, essentially limits our fuel options to the

following three: liquid hydrogen (LH₂), Rocket Propellant 1 (RP-1) and liquid methane (LCH₄).

3.2.2 Liquid Hydrogen (LH₂)

Considered an ideal rocket propellant, liquid hydrogen offers the highest performance metrics of all fuels used in chemical rocket propulsion [19] [23]. Hydrogen has the lowest molecular weight of any known substance (2.016 g/mol [24]) and the highest specific energy of any non-radioactive fuel (141.766 MJ/kg [24]) [23]. When paired with an oxidizer, LH₂, consequently, produces relatively low average molecular weight of the combustion products and generates comparatively high adiabatic flame temperature—two factors that help maximize the exhaust velocity and thus the specific impulse of the rocket engine. Moreover, the combustion of LH₂ with LOX is extremely energetic and efficient (producing typically only water vapour), and yields the highest theoretical specific impulse of any conventional bipropellant combination [23]. In addition to the above characteristics, such properties as low viscosity, high specific heat and high thermal conductivity make LH₂ a desirable coolant for thrust chambers [25] [12]. LH₂ is manufactured from gaseous hydrogen by successive compression, cooling and expansion processes [12], and is a non-corrosive, non-toxic, colourless and odourless fluid [24].

LH₂ does come with a few major downsides, however. Firstly, liquid hydrogen has an awfully low density (of only 70.78 kg/m³ at its boiling point under normal pressure [24]). Such low density implies that LH₂ “takes an inordinate tankage volume to hold any great amount of the fuel” [19, p. 106]; requiring voluminous and thus massive propellant tanks in turn compounds drag on the rocket during ascent and detracts mass from that of the payload. Despite hydrogen’s exceptionally high specific energy (energy per unit mass), LH₂ offers a remarkably low volumetric energy density (energy per unit volume)—an attribute that stems solely from its low specific gravity [26]. Secondly, LH₂ is a highly cryogenic liquid (with a normal boiling point of just 20.37 K or -252.78°C [24]). Dealing with the fuel, therefore, poses formidable technical challenges such as adequacy of thermal insulation (to minimize propellant evaporation and boiloff losses), allowance for venting mechanism (to vent any gaseous fluid overboard), and selection of compatible materials (since many materials become brittle at such temperatures) [19]. And thirdly, hydrogen is extremely flammable over a wide range of mixture ratios (thus making it a ferocious fire and explosion hazard) [12].

Despite having its shortcomings, the advantages of liquid hydrogen far outweigh any disadvantages of the fuel. It offers a theoretical specific impulse of about

380 s (under the following conditions: combustion chamber pressure = 1000 psi = 6894.757 kPa; nozzle exit pressure = 1 atm = 101.325 kPa; optimum expansion) when used in conjunction with LOX [27] [12]. And therefore, LH2 finds application in a number of rocket engines worldwide. Some of those engines/rockets include the USA's J-2 (used on Saturn V), RL-10 (used on Alas V, Delta IV, Space Launch System and Vulcan Centaur), RS-25 (used on the Space Shuttle orbiter and Space Launch System) and RS-68 (used on Delta IV); Europe's HM-7B, Vulcain and Vinci (used on the Ariane launch vehicle family); India's CE-7.5 and CE-20 (used on GSLV Mark II and GSLV Mark III respectively); Japan's LE-5 and LE-7 (for H-I and the H-II series of launch vehicles); and China's YF-73, YF-75 and YF-77 (used on the Long March family of rockets) [16] [28] [29]. And it's for the same reason that this project takes performance parameters from the LOX/LH2 combination into account for analysis.

3.2.3 Rocket Propellant 1 (RP-1)

The first experimental flight of a liquid rocket (back in the March of 1926 by Robert Goddard) was fueled by gasoline [19]. And ever since those early days of rocketry, a number of petroleum derivative fuels have been used to power liquid propellant rockets—a handful of which include (variants of) kerosene, gasoline and liquefied natural gas. But these complex hydrocarbon mixtures exhibited wide variance in physical properties and chemical compositions among each fuel of the same class (due to inconsistencies in process of refining and in degree of control exercised during their manufacture), which meant that no two barrels of the fuel were alike enough to produce accurate and precise results across engine tests and to meet “the narrow limits of specified engine performance that is needed for a predictable flight path of many a vehicle” [12] [19] [15]. This led to the requirement of petroleum fuels meeting rather rigorous specifications and ultimately to the development of a highly refined product known as RP-1. As described by Clark, RP-1 is “a kerosene in the C₁₂ region, with a H/C ratio between 1.95 and 2.00, containing about 41 percent normal and branched paraffins, 56 of naphthenes, 3 of aromatics, and no olefins at all” [19, p. 105].

Despite offering only a modest specific impulse, RP-1 is used quite often in combination with liquid oxygen for high-total-impulse applications—perhaps more frequently than even LH2 [28]. This is due in part to the high energy density of RP-1 which produces a significantly energetic reaction for each volume of the fuel consumed, which in turn generates a correspondingly high temperature of combustion [30] [12]. But because it's a hydrocarbon mixture comprising numerous

complex molecular structures, its combustion with LOX yields products with fairly high effective molecular weights, which eventually lowers the ratio T_{cc}/\mathfrak{M} , and consequently delivers only a decent exhaust velocity [31]. Besides energy density, RP-1 has a high specific gravity (within 0.799 and 0.815 at about 15 °C [32]), which allows for pretty small and light propellant tanks for a given mass of the fuel. Additionally, it is a storable, non-corrosive, non-toxic propellant that is, despite being flammable, relatively easy to handle [30].

RP-1, nevertheless, has its own challenges to surmount. Primarily, it has a tendency to undergo polymerization under high enough temperatures [19]. Petroleum derivative fuels, due to the thermal instability of their complex organic compounds, experience thermal cracking (wherein long hydrocarbons chains break down into simpler molecules) as temperature of the fuel rises [30]. This eventually results in the deposition of soot, coke, and other assorted carbonized residues at regions of high heat transfer rates which, while occasionally acting as a thermal insulator, mostly impedes heat transfer, inhibits propellant flow, and ultimately fouls up intricately designed components of (typically regeneratively cooled) rocket engines [19] [15]. Moreover, and much like any other fuel, RP-1 is combusted slightly fuel rich with LOX in order to marginally raise the specific impulse of the bipropellant combination; doing so, however, further exacerbates the polymerization problem.

Notwithstanding the downsides, RP-1 together with LOX continues being the semi-cryogenic combination of choice worldwide. Burning the pair delivers a theoretical specific impulse of about 290 s (under these conditions: combustion chamber pressure = 1000 psi = 6894.757 kPa; nozzle exit pressure = 1 atm = 101.325 kPa; optimum expansion) [27] [12]. The bipropellants have notably been used in the following engines/rockets: the F-1 engine (used on Saturn V); RD-170 (the Energia launch vehicle) and its variants like RD-171 (the Zenit family), RD-180 (Atlas V) and RD-191 (in both Angara and Antares); RD-107 and RD-108 (in different configurations in the R-7 derivative vehicles including Vostok, Voskhod and Soyuz); Merlin (Falcon 9 and Falcon Heavy); and Rutherford (Electron) [16] [28] [31]. This project, therefore, looks at performance parameters from the bipropellant combination for analysis.

3.2.4 Liquid Methane (LCH₄)

Methane, chemically called carbon tetrahydride, is the simplest hydrocarbon molecule, and is composed of four hydrogen atoms attached to one carbon atom. Also known as marsh gas, it is the primary constituent of natural gas, and finds extensive usage as a hydrocarbon fuel owing to its relative abundance on Earth. It is

a colourless and odourless gas with a boiling point of 111.65 K or -161.50°C under normal conditions [33]. Upon stoichiometric combustion, one unit of methane reacts with two units of oxygen to release one unit of carbon dioxide and two units of water [34].

Although the usage of liquid methane as a rocket propellant had been proposed since the 1960s, it has only been recently that the cryogenic fuel accrued any pragmatic thrust chamber operation and/or test flight experience [35]. Methane is regarded as the propellant of choice for future long-duration crewed missions to Mars where it can be synthesized via the Sabatier process using in-situ resources on the planet [27]. When burned with liquid oxygen, LCH₄ generates a high adiabatic flame temperature (of 3953 K or 3679.85°C under stoichiometric and normal temperature and pressure conditions [36]) due to its high heat of combustion (of -55536 kJ/kg [33]). And being the lightest organic compound (with a molar mass of just 16.04 g/mol [33]), molecular weights of its combustion products are comparably low [34]. In addition, methane has a low ratio of specific heat (at 1.306 [33]) which improves both characteristic velocity and thrust coefficient.

Each above characteristic advantages LCH₄ in delivering a remarkably high exhaust velocity and thereby specific impulse. The bipropellant combination yields, as Sutton asserts [15], a theoretical specific impulse of approximately 310 s (under these conditions: combustion chamber pressure = 1000 psi = 6894.757 kPa; nozzle exit pressure = 1 atm = 101.325 kPa; optimum expansion and shifting thermochemical equilibrium in the nozzle).

The remarkably high specific impulse from the LOX/LCH₄ combination is, whilst lower than that of LH₂, higher than that of most storable propellants including RP-1 [27]. Yet unlike LH₂, liquid methane has a relatively high density—nearly six times as much as that of hydrogen—of 422.8 kg/m^3 at its normal boiling point [33]. This implies that LCH₄ offers a higher density impulse than LH₂ does and requires much smaller and lighter propellant tanks and associated systems than LH₂ does. Propulsion systems burning liquid methane, therefore, yield a better overall performance than even liquid hydrogen. Moreover, having the best hydrogen to carbon ratio of all hydrocarbons, methane burns much cleaner and more completely than every other hydrocarbon fuel [30]. This forestalls the negative effects of propellant dissociation and polymerization—which fuels with complex molecular structures like RP-1 typically foster—with a rocket engine and facilitates reusability of the propulsion system [30]. Furthermore, temperature difference between LOX and LCH₄ (about 20K) is much smaller than that between LOX and either LH₂ (roughly 70 K) or RP-1 (nearly 175 K) which permits tank

designs with less stringent requirements for insulation in between the tanks [37]. Additionally, methane has such desirable properties as high specific heat, high critical temperature and low dynamic viscosity, and is a non-corrosive and non-toxic albeit flammable propellant that is relatively inexpensive and abundantly available [38]. The combination of properties above gives LCH₄ an edge over the shortcomings of using either LH₂ or RP-1.

Even though liquid methane has a suite of attractive characteristics to offer, development of a LOX/LCH₄ propulsion system had largely been put off until now [12]. There were a few proposals to build and test methalox rocket engines prior to the 2010s, but the efforts were limited—partly because of bureaucratic quagmire which deemed any urgency of pursuing qualification of such an engine unwarranted—and the projects were cancelled [35]. Over the past decade, however, there has been a renewed interest in the development of LCH₄-fueled propulsion systems. Most notably, the spaceflight company SpaceX has built, tested and flown the Raptor engine for its Starship launch vehicle. The BE-4 is another similar engine undergoing development for use on the New Glenn and the Vulcan Centaur. Respective organizations from Europe, Russia, China and India have also announced their initiatives to develop rocket engines running on methane [16] [28]. Keeping in line with the current interests, and in a quest to further investigate the performance metrics of the bipropellant, this project intends to employ the LOX/LCH₄ combination for the development of our experimental engine.

3.3 PROPELLANT PERFORMANCE ANALYSIS

The generation of thrust in a rocket propulsion system ideally involves the following two processes: combustion and expansion. All species of the propellant mixture undergo a rapid enough combustion reaction within a long enough residence time under an isobaric condition inside a combustion chamber, attaining chemical equilibrium in the process [12]. Then the combustion fluid experiences an adiabatic and reversible expansion process on entering a supersonic nozzle and undergoes a drop in temperature and pressure, reflecting the conversion of thermal energy into kinetic energy [12].

Several methods with varying degrees of complexity have been implemented to analyse relevant chemical and thermodynamical properties associated with the above processes. Yet there typically exist two simplistic approaches in analysing the gas flow characteristics within a supersonic nozzle: *frozen composition flow* and *shifting composition flow*. In a frozen flow condition, the gas expansion is considered

instant and its composition is assumed invariant throughout the nozzle, that is, the combustion fluid experiences no chemical reactions or phase changes during the expansion process and chemical composition of the reaction products is identical at both the combustion chamber and the nozzle exit. This approach tends to underestimate performance values like specific impulse and characteristic velocity of a propulsion system typically by 1 to 4% [12]. For a shifting flow condition, however, the gas is presumed to undergo instantaneous chemical reaction and hence exist in equilibrium among all reaction species during the nozzle flow, i.e., the gas composition does change between the combustion chamber and the nozzle exit. This method usually overestimates performance values by 1 to 4% [12].

Because of the complex chemical and thermodynamical nature of the processes involved, exact dependence of the performance parameters on the propellant mixture is difficult to demonstrate through simple analytical formulae; iterative computing methods have thus been developed to obtain solutions to such problems. The requisite computations in this project are performed using the tool *CEARUN*, an online computer program facilitating use of the NASA code *CEA* (Chemical Equilibrium with Applications) [39]. Published in 1994 by Sanford Gordon and Bonnie J. McBride at the NASA Glenn (formerly Lewis) Research Center, *CEA* employs chemical and thermodynamical equilibrium codes in order to analyse problems involving rocket performance, combustion properties, detonation parameters, shock parameters, and other similar applications [40]. In addition, the software *Rocket Propulsion Analysis* (RPA Standard Edition v.2.x), developed by Alexander Ponomarenko, is used to perform certain conceptual computations in the preliminary design of our chemical rocket propulsion system [41].

All calculations in this project have implemented the frozen composition flow condition in order to obtain slightly conservative values for performance and account for uncertainties in our engine design procedures. Additional assumptions in the project include ideal gas behaviour, one-dimensional forms of the continuity, energy and momentum equations, negligible velocity at the forward end of the combustion chamber, isentropic expansion in the nozzle, and chemical equilibrium in the combustion chamber.

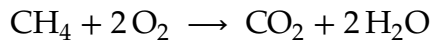
3.4 MIXTURE RATIO

The mixture ratio of a bipropellant combination is the ratio of mass flow of the oxidizer to mass flow of the fuel. For a certain combination of oxidizer and fuel, the highest flame temperature is obtained under the *stoichiometric mixture ratio*,

wherein both the species react in the exact stoichiometric proportion resulting in a complete combustion reaction [42]. However, the maximum exhaust velocity and thus the highest specific impulse from burning the propellants is achieved at the *optimum mixture ratio*, in which the rocket engine typically operates with an excess proportion of the fuel [13]. A “fuel rich” mixture is oftentimes more advantageous than otherwise because it not only leaves unburned fuel species in the combustion fluid (thus lowering effective molecular weight of the exhaust jet) but also burns cooler inside the combustion chamber (thereby mitigating excessive thermal loads on the thrust chamber). Yet occasionally, an *off-optimum mixture ratio* may be preferred when it allows for such desirable characteristics as better combustion stability, improved chemical equilibrium during expansion, required coolant flow rate, or even reduced propellant tank size [13] [42].

3.4.1 Liquid Oxygen & Liquid Methane

The combustion of methane may be summarized as



The reaction above is in stoichiometric proportions, comprising 1 mol of CH₄ and 2 mols of O₂ as reactants and 1 mol of CO₂ and 2 mols of H₂O as products. This implies, with standard atomic weights for the constituent elements being H = 1.008, C = 12.011 and O = 15.999, complete combustion of methane requires 64 kg of O₂ and 16 kg of CH₄ for a stoichiometric mixture ratio of 4 : 1 by mass [42].

Yet by convention, a fuel rich mixture instead of the stoichiometric mixture is employed for the operation of our thrust chamber. In order to determine the best propellant mixture ratio, we examine the variation of parameters like specific impulse, combustion temperature, characteristic velocity and molecular mass with changes in mixture ratio.

Again, the optimum mixture ratio of a propellant mixture is dependent on the pressures at which a thrust chamber operates. We, therefore, preliminarily perform our calculations for mass mixture ratios ranging from 1.0 through 7.0 with an interval of 0.25 and under the following conditions: combustion chamber pressure $P_{cc} = 1000 \text{ psi} = 6894.757 \text{ kPa}$; nozzle exit pressure $P_e = 1 \text{ atm} = 101.325 \text{ kPa}$ (sea level condition); nozzle area ratio $\epsilon = 40$ (vacuum condition); frozen flow characteristic and infinite area combustor option.

The combustion chart, computed in [43], for determining optimum mixture ratio as a function of combustion chamber pressure at two different nozzle exit pressures

for the liquid oxygen and liquid methane combination is presented in figure 3.1.

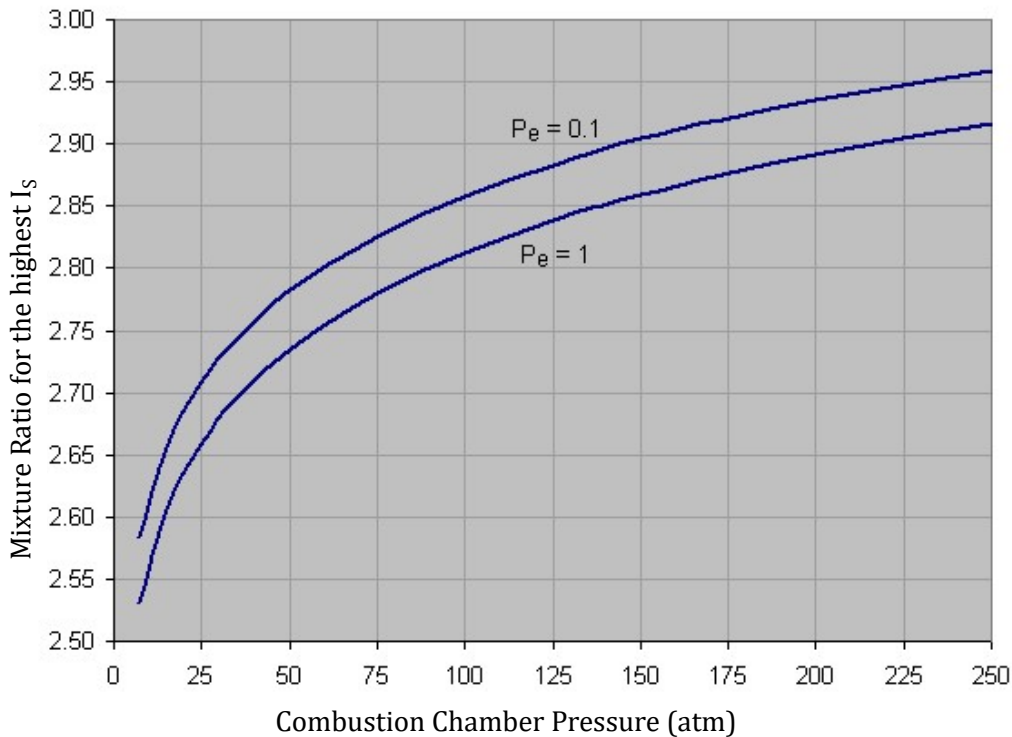


Figure 3.1.: The dependence of optimum mixture ratio as a function of combustion chamber pressure at two different nozzle exit pressures (of 0.1 atm and 1.0 atm) for liquid oxygen/liquid methane [43].

Results depicting the variation of specific impulse (both at sea level and in vacuum), temperature (both inside combustion chamber and at throat), characteristic velocity, and effective molecular mass as a function of mixture ratio are plotted in figures 3.2 to 3.4.

On examining the figures, it is evident that an oxidizer-to-fuel mass mixture ratio of 2.75 yields the highest performance parameters, viz. specific impulse (both at sea level and in vacuum) and characteristic velocity, for the aforementioned operating conditions. In addition, the optimum mixture lowers both the effective molecular mass of combustion fluid by roughly 3 units as well as the temperature (both inside combustion chamber and at throat) by about 200 K in comparison to the respective metrics of the stoichiometric mixture. Figure 3.5 portrays the mixture ratios, optimum and stoichiometric, that respectively produce the highest values of specific impulse (at sea level) and temperature (inside combustion chamber) for the bipropellant combination.

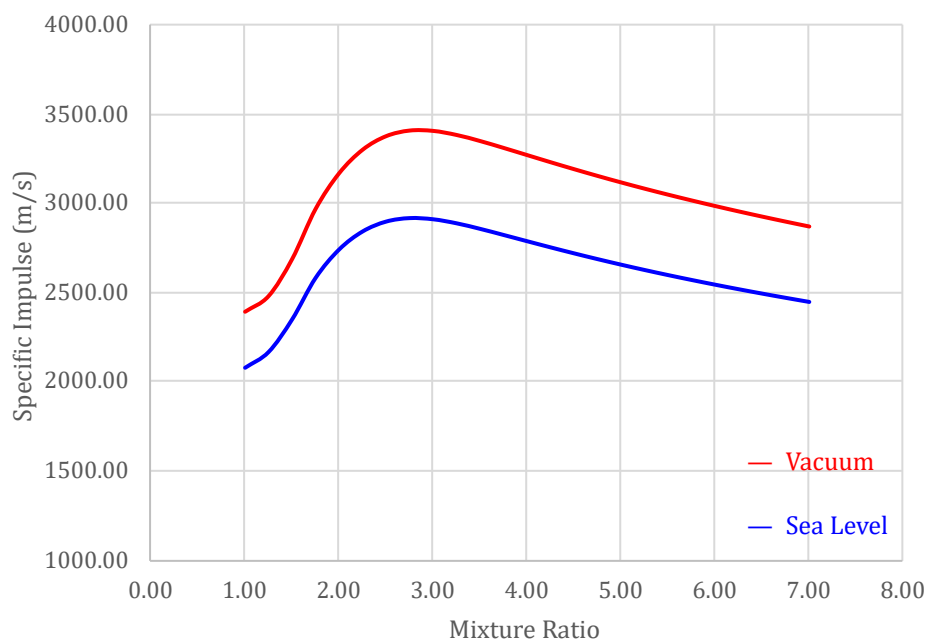


Figure 3.2.: Variation of specific impulse, both at sea level and in vacuum, with mixture ratio.

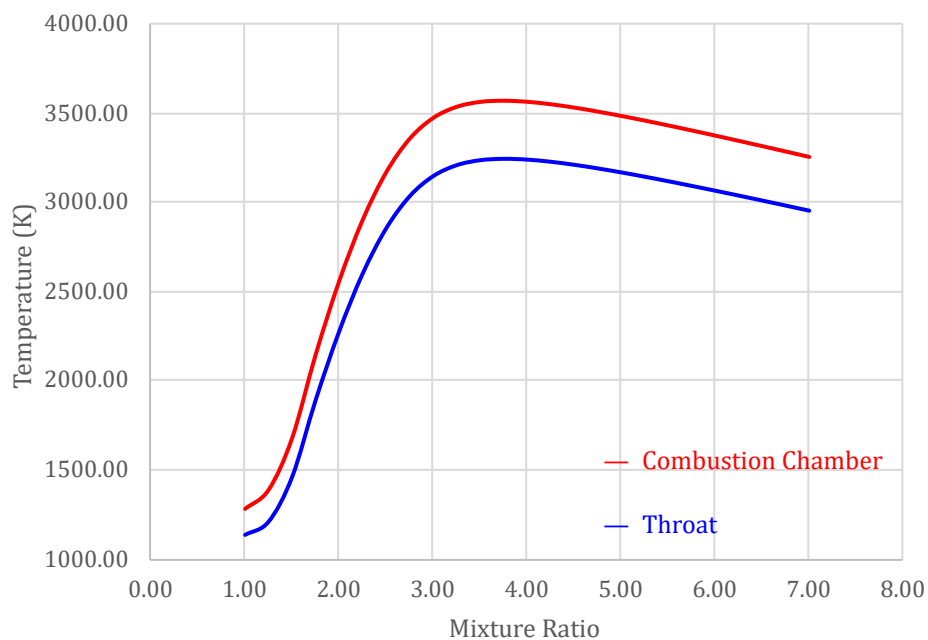


Figure 3.3.: Variation of temperature, both inside combustion chamber and at throat, with mixture ratio.

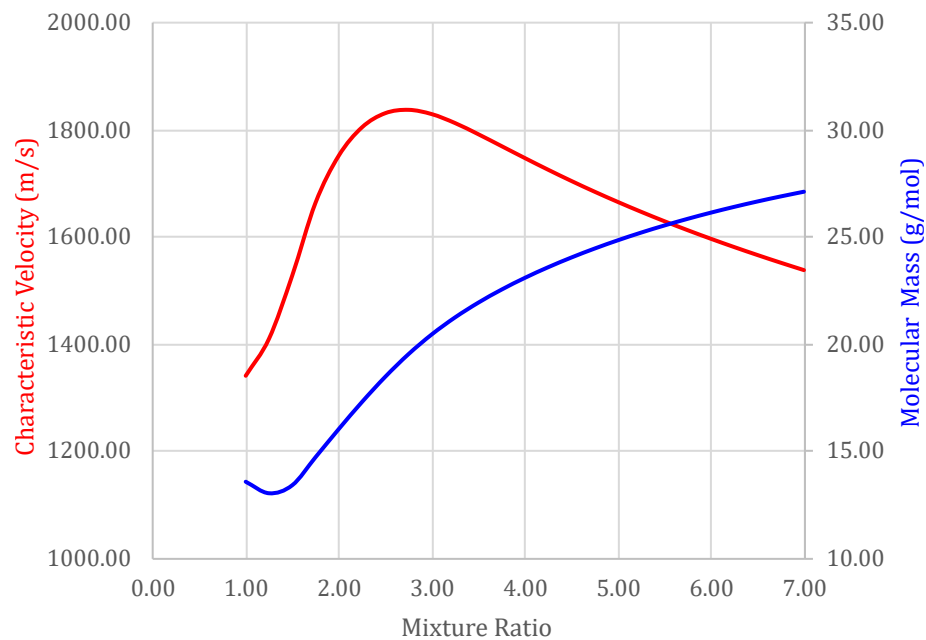


Figure 3.4.: Variation of characteristic velocity and molecular mass with mixture ratio.

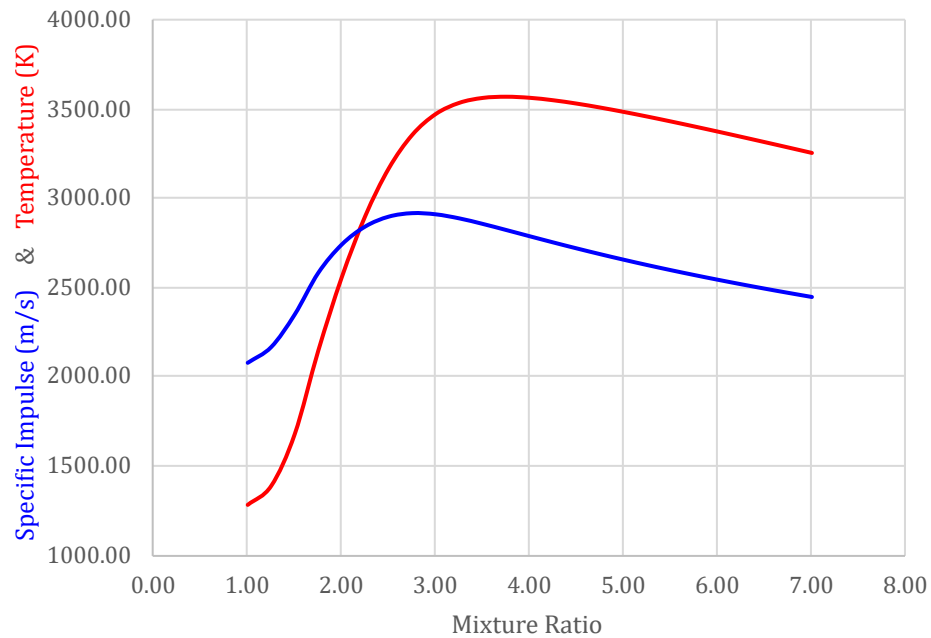


Figure 3.5.: Variation of specific impulse (at sea level) and temperature (inside combustion chamber) with mixture ratio.

3.4.2 Liquid Oxygen & Liquid Hydrogen

As pledged, we take a look at the performance parameters from the LOX/LH₂ combination in this segment. Unlike for other bipropellants, an optimum mixture ratio for liquid oxygen and liquid hydrogen is not necessarily the best mixture ratio for the combination. The highest values of specific impulse usually occur at a mixture ratio of around 3.5 [12]. But because of the awfully low specific gravity of liquid hydrogen, a slight increase in the oxidizer-to-fuel mass mixture ratio results in a significant decrease in the volume of the fuel consumed. Braeunig [43] states that employing a mixture ratio of about 5.5 reduces the tankage volume of the fuel by almost a quarter. And as mentioned before, the smaller the volume of the propellant tank is, the lower are the vehicle's structural mass and aerodynamic drag, and the higher, consequently, become the delta-v and payload carrying capacity of the rocket. Employing a higher (and off-optimum) mixture ratio, therefore, offsets any loss in the specific impulse and results in a better overall vehicle performance. In practice, most liquid oxygen/liquid hydrogen rocket engines typically operate at mixture ratios between 5.0 and 6.0 [43].

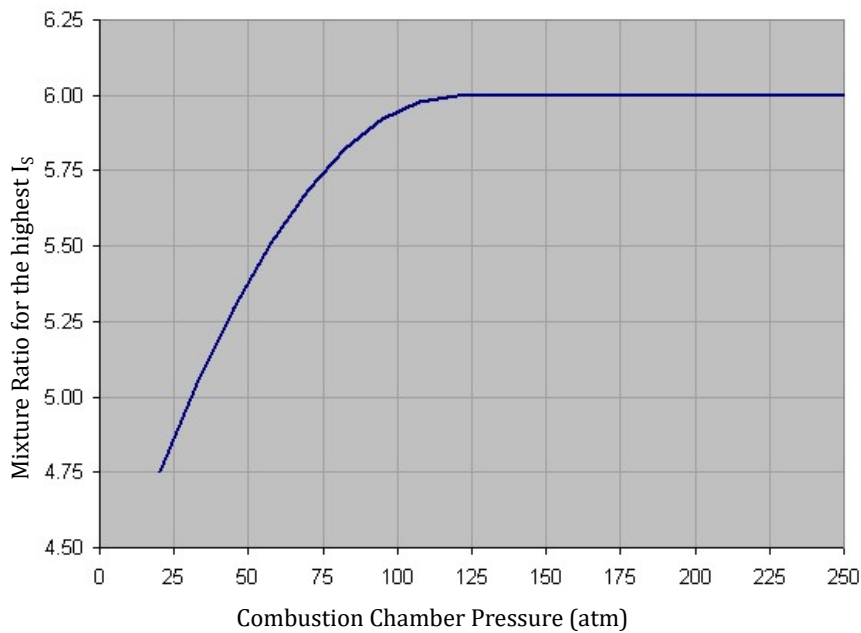


Figure 3.6.: The dependence of optimum mixture ratio as a function of combustion chamber pressure for LOX/LH₂ [43].

The combustion chart, computed in [43], for determining the best mixture ratio as a function of combustion chamber pressure for liquid oxygen and liquid hydrogen is presented in figure 3.6. Regardless, we perform our calculations for specific

impulse, combustion temperature and molecular mass as a function of mixture ratio—for the same range of O/F mass mixture ratios and under the same conditions of thrust chamber operation—as in the subsection 3.4.1. And results of the calculations have been plotted in figure 3.7.

3.4.3 Liquid Oxygen & Rocket Propellant 1

Going ahead, we now look at the performance parameters from the LOX/RP-1 combination here. Since RP-1 does not have any idiosyncrasies that LH2 has, the procedure to compute the best oxidizer-to-fuel mass mixture ratio for this bipropellant combination is fairly straightforward.

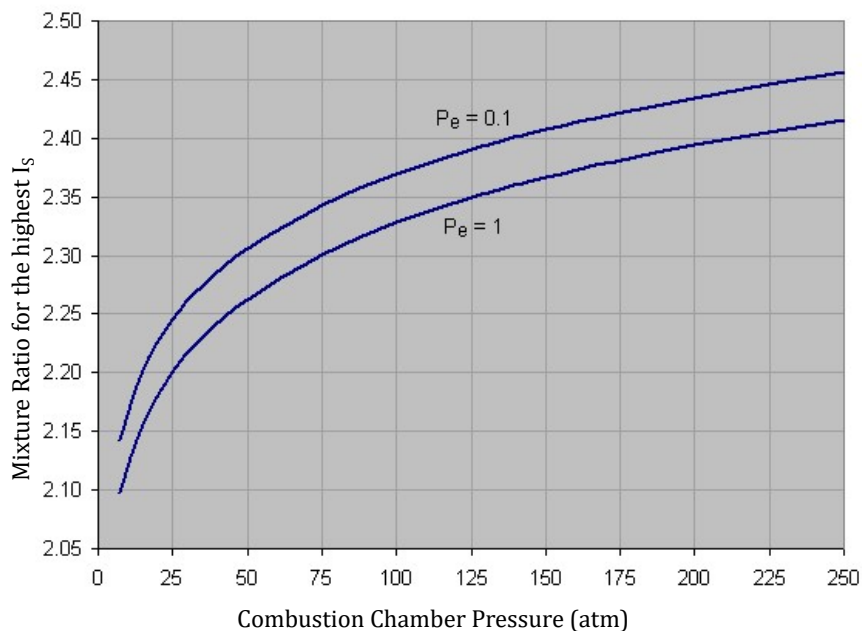


Figure 3.8.: The dependence of optimum mixture ratio as a function of combustion chamber pressure at two different nozzle exit pressures (of 0.1 atm and 1.0 atm) for LOX/RP-1 [43].

The combustion chart, computed in [43], for determining optimum mixture ratio as a function of combustion chamber pressure at two different nozzle exit pressures for LOX and RP-1 is presented in figure 3.8. And as in the previous segment, we perform our calculations for specific impulse, combustion temperature and molecular mass as a function of mixture ratio—for the same range of O/F mass mixture ratios and under the same conditions of thrust chamber operation—as in the subsection 3.4.1. Results of the calculations have been plotted in figure 3.9.

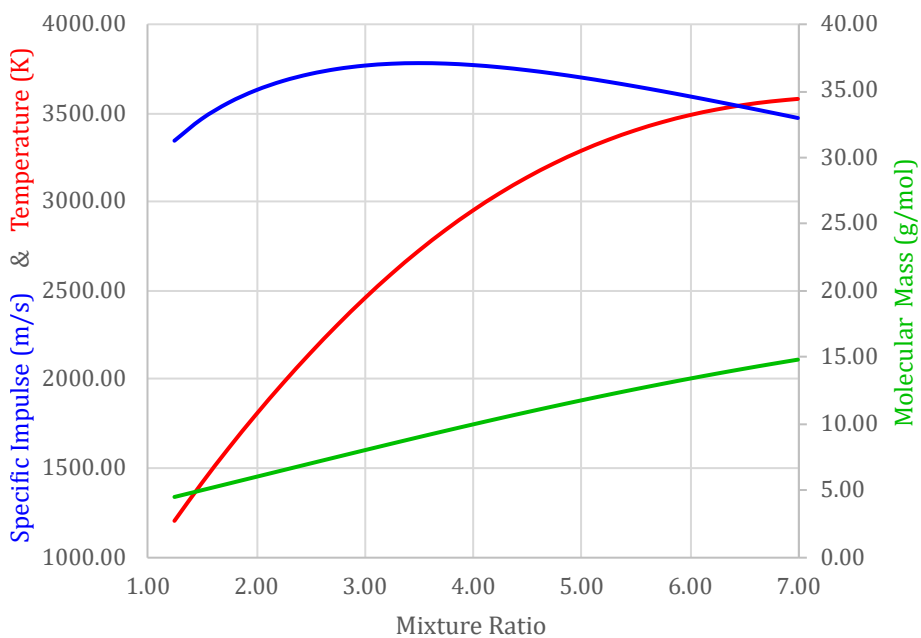


Figure 3.7.: Variation of specific impulse (at sea level), temperature (inside combustion chamber) and molecular mass with mixture ratio for LOX/LH₂.

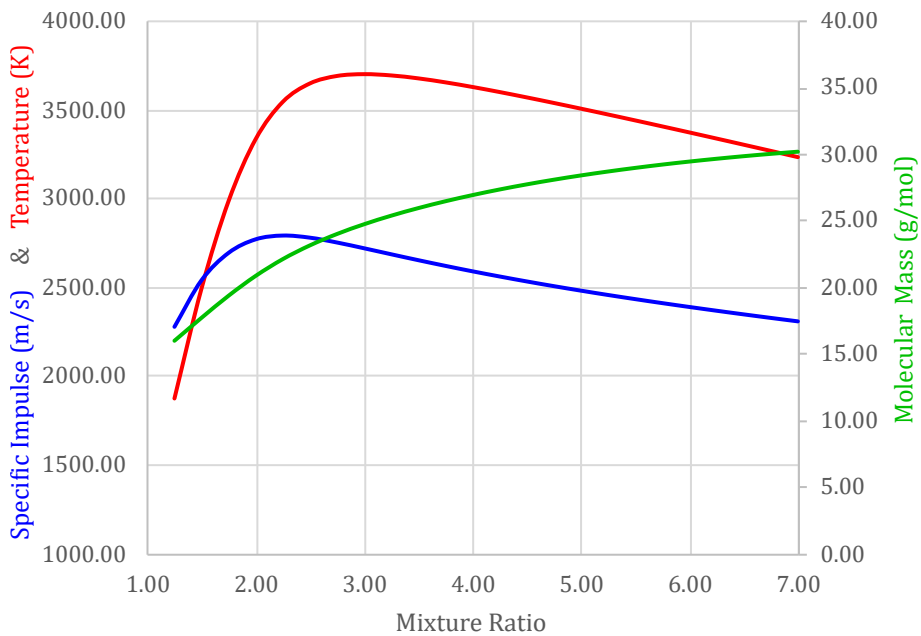


Figure 3.9.: Variation of specific impulse (at sea level), temperature (inside combustion chamber) and molecular mass with mixture ratio for LOX/RP-1.

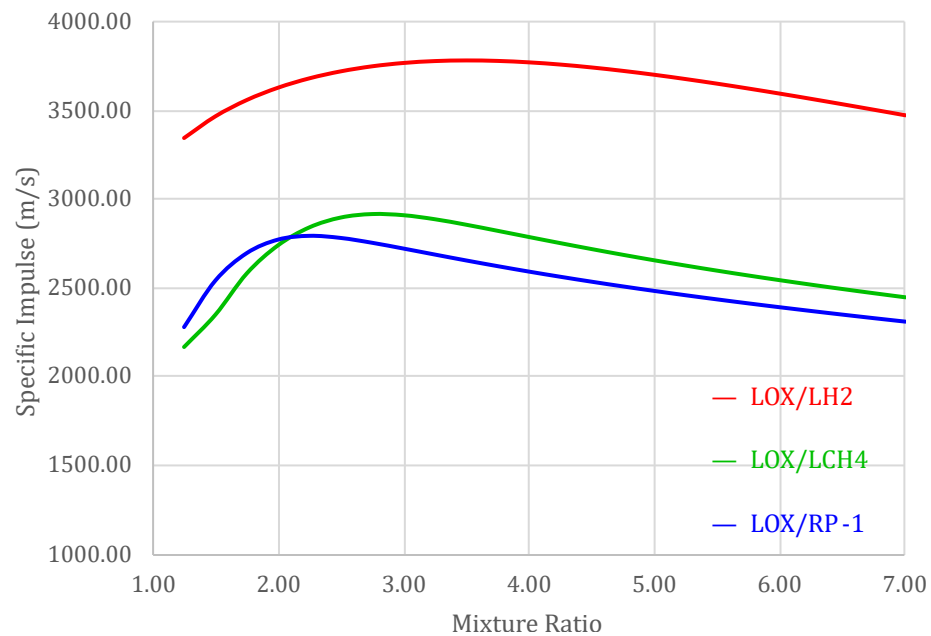


Figure 3.10.: Variation of specific impulse (at sea level) with mixture ratio for all the three bipropellants considered.

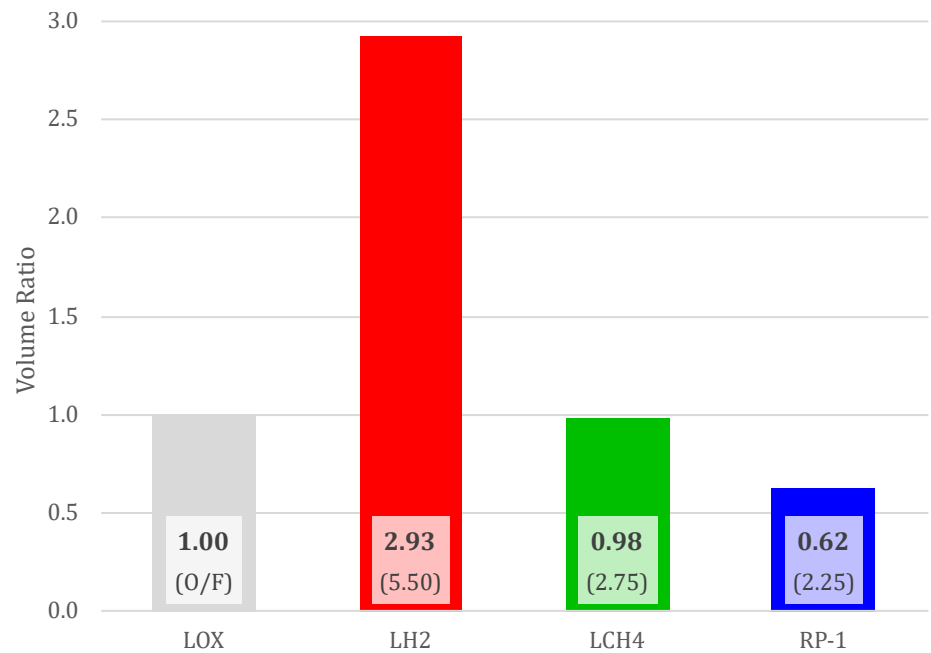


Figure 3.11.: The relative volume of respective fuels per unit volume of the oxidizer for the considered mass mixture ratios.

3.5 SUMMARY

The choice of liquid propellants has phenomenal implications on the design of a rocket engine. Of notable significance for a bipropellant combination are such parameters as specific heat ratio, combustion chamber temperature and effective molecular mass of the exhaust jet. Again, physical properties such as specific gravity, specific heat, thermal conductivity, vapour pressure and viscosity, properties which do not directly improve performance, are also of remarkable importance during propellant selection.

We look in depth at one oxidizer, LOX, and three fuels, LH₂, RP-1 and LCH₄, for our liquid rocket engine. In addition to the experimental prospect, our motivation to employ methalox over the other two bipropellants stems from its suite of properties, both pros and cons, being right between those of hydrolox and kerolox combinations.

Using CEA, we analyse the performance parameters of each mixture for a frozen flow composition along with certain additional assumptions. The optimum mixture ratio for each bipropellant mixture is thus preliminarily determined under the following conditions: combustion chamber pressure $P_{cc} = 1000\text{ psi} = 6894.757\text{ kPa}$; nozzle exit pressure $P_e = 1\text{ atm} = 101.325\text{ kPa}$ (sea level condition); nozzle area ratio $\epsilon = 40$ (vacuum condition); frozen flow characteristic and infinite area combustor option.

From their respective plots, it is observed that the mixture ratios of 2.75, 5.50 and 2.25 yield specific impulses of 296.88 s, 372.75 s and 285.19 s for methalox, hydrolox and kerolox combinations. Corrected for a 4% over-performance, we obtain specific impulses of 285.00 s, 357.84 s and 273.78 s for the bipropellant combinations respectively. Figure 3.10 depicts the variation of specific impulse as a function of mixture ratio for all three bipropellant mixtures considered. Figure 3.11 helps visualize the relative volume of each fuel with respect to that of liquid oxygen at our considered mixture ratio: the volume of liquid methane is almost equal to that of LOX for a mixture ratio of 2.75. Moving ahead, we carry the optimum mixture ratio of LOX/LCH₄ forward to the subsequent chapter(s).

4

PROPELLANT FEED SYSTEMS

Transfer of liquid propellants from their tanks to the thrust chamber at the desired flow rates and injection pressures requires a feed system (also called an engine cycle). The selection of one feed system over another depends on a multitude of factors: from propellant combination and performance specification of the engine to mission requirement and operational envelope of the vehicle. Even the choice of a sub-type of feed system—regulated vs blowdown pressurization system or staged combustion vs gas generator turbopump mechanism—is influenced by aspects such as complexity, controllability, reliability and reusability. Largely, a propellant feed system can be classified as a pressure feed system or a pump feed system; and depending on how power is derived to run the pump, the latter can again be classified as a turbopump feed system or an electropump feed system.

4.1 TYPES OF FEED SYSTEMS

In a nutshell, a pressure feed system needs a difference in pressure between the propellant tank and the combustion chamber in order to drive the propellant downstream. A pump feed system, contrarily, keeps the tank pressurization comparatively low and utilizes a pump near the thrust chamber inlet in order to maintain adequate propellant flow rate and raise the fluid pressure to the desired level.

As a rule, liquid rocket propulsion systems involving fairly high thrust magnitudes and/or long operation durations typically employ a pump feed system [12] [13]. Because the more powerful propulsion systems require relatively high combustion chamber pressures to operate, accommodating propellant tanks that are capable of withstanding such high tank pressurization, as with pressure feed systems,

results only in an inordinate inert mass penalty, which is hardly feasible for a flight vehicle. Notwithstanding the foregoing, designing a rotodynamic pump along with all associated components can permit little margin for uncertainties, and employing a pump feed system can present tremendous operational complications if not downright unforgiving circumstances.

Each propellant feed system comes with a suite of benefits and drawbacks. The preference of one to another therefore entails a compromise between some critical design parameters and some crucial performance metrics. The more common types of feed systems, viz. gas-pressure feed systems, turbopump feed systems and electrically-driven-pump feed systems, along with some major sub-types, have been looked at below.

4.1.1 Pressure Feed Systems

Perhaps the simplest among all engine cycles, a pressure feed system uses a pressurant fluid to pressurize the propellant tank and expel the propellant into the combustion chamber. The pressurant can either be a gas stored in a tank, a gas generated through chemical reaction or even the evaporated propellant itself [13]. Mere actuation of the start/shutoff valves delivers the pressurant into the propellant tanks and/or drives the propellants into the combustion chamber, making the system extremely reliable [12].

There are two common types of pressure feed systems: regulated systems and blowdown systems [12]. A regulated pressurization system includes a high-pressure gas-supply tank and uses a pressure regulator in the feed line to maintain constant propellant tank pressurization, and thus operates the thrust chamber essentially at constant pressure and constant thrust. A blowdown pressurization system, on the other hand, contains the pressurant gas within the propellant tank at an initial maximum pressure and loses pressurization steadily with consumption of the propellant, resulting in a gradual decrease in thrust over time.

Pressure feed systems have practical limitations on propellant tank pressurization which in turn limits engine output and vehicle performance. These systems, however, offer superior performance to pump feed systems when the total impulse is relatively low, the propellant mass is relatively low, the combustion chamber pressure is relatively low, the engine thrust-to-weight ratio is relatively low, and when repeated short-duration thrust pulses are the requirement [12]. A few renowned engines that have employed the pressure feed system include the Service Propulsion System (SPS) engine on the Apollo Command/Service Module; the Descent

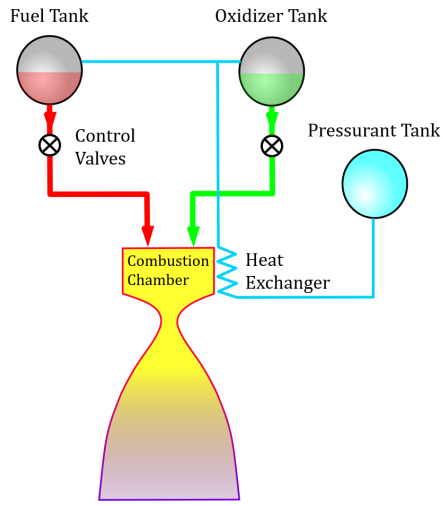


Figure 4.1.: Schematic diagram of a generic blowdown-type pressure feed system.

Source: Wikimedia Commons

Propulsion System (DPS) and the Ascent Propulsion System (APS) engines on the Apollo Lunar Module; and the Orbital Maneuvering System (OMS) engines on the Space Shuttle orbiter [44] [28]. Figure 4.1 shows the schematic diagram of a typical pressure feed system.

4.1.2 Turbopump Feed Systems

A turbopump feed system is, by definition, a combination of one or more gas turbine(s) and rotodynamic pump(s). The turbine derives its energy from the expansion of a high-enthalpy gaseous working fluid which imparts a rotational *impulse* and/or *reaction* force on the rotor assembly [45]; this mechanical energy provides the shaft power, with or without a gear transmission, for driving the propellant pump at the desired speeds and torques. Turbines are classified into radial-flow turbines and axial-flow turbines; the latter again are sub-classified into reaction turbines and impulse turbines, which in turn have multiple types such as single-rotor impulse turbines, velocity-compounded impulse turbines, pressure-compounded impulse turbines, and the like [13].

The rocket propellant pump imparts kinetic energy from the rotor to the propellant fluid flow and converts the energy into hydrostatic pressure necessary for the thrust chamber operation [45]. Pumps principally are categorized as radial (or centrifugal) pumps and axial pumps. The fundamental elements of a pump are the rotor assembly (which usually comprises an inducer, an impeller, a shaft and

bearings) and the stator assembly (which consists of a casing with diffuser vanes, a volute with discharge ducts, wear rings and shaft seals). The inducer, an axial-flow rotor positioned at the pump inlet, provides the propellant fluid entering the main pump section with an increased total pressure sufficient to permit non-cavitating operation of the impeller. The impeller of a radial pump is a rotating wheel with blades that discharges the flow radially outwards, whereas that of an axial pump is a cylindrical rotor with multiple rows of rotating blades which keeps the fluid flowing largely axial. While the impeller blades accelerate the fluid flow by imparting kinetic energy to it, the diffuser vanes decelerate, or *diffuse*, the flow to convert the fluid's velocity head into pressure head. The volute collects and redirects the pressurized fluid to the pump's discharge outlet.

The engine cycle of a turbopump feed system defines the source of the energetic drive fluid to power the turbopump assembly and the destination of the turbine exhaust fluid after doing the work, and outlines propellant flow paths through major engine components. Based on how the working fluid from the turbine exhaust is handled, an engine cycle may be classified as open or closed [12]. In an open cycle engine, the turbine working fluid is discharged into the diverging nozzle section of the thrust chamber at a location downstream of the nozzle throat or is ejected overboard altogether usually after undergoing expansion through its own low-area-ratio nozzle. The turbine working fluid in a closed cycle engine, however, is injected into the combustion chamber through the injector and undergoes expansion through the entire pressure ratio across the thrust chamber nozzle. While a closed cycle engine offers somewhat better specific impulse than its open cycle counterpart, the performance advantage occurs at the expense of engineering complexity from ducting the turbine exhaust fluid into the combustion chamber at the flow rates and injection pressures necessary for the engine operation [12].

For any engine cycle, an increased flow rate of the working fluid into the turbine increases the power output of the pump, therefore increasing flow rate of the propellants into the combustion chamber, and consequently increasing the thrust magnitude from the engine. Moreover, the working fluid comprises a less-than-optimal mixture ratio—either very fuel-rich or very oxidizer-rich—so as to preclude excessive fluid temperatures and to provide a more benign environment for the turbine elements [12].

A key component of all high-total-impulse rocket engines, the turbopump is a highly intricate piece of high-precision high-accuracy high-shaft-speed machinery. High reliability, along with high performance and high efficiency, is therefore of the utmost importance for the operation of the turbopump feed system. Selection of a

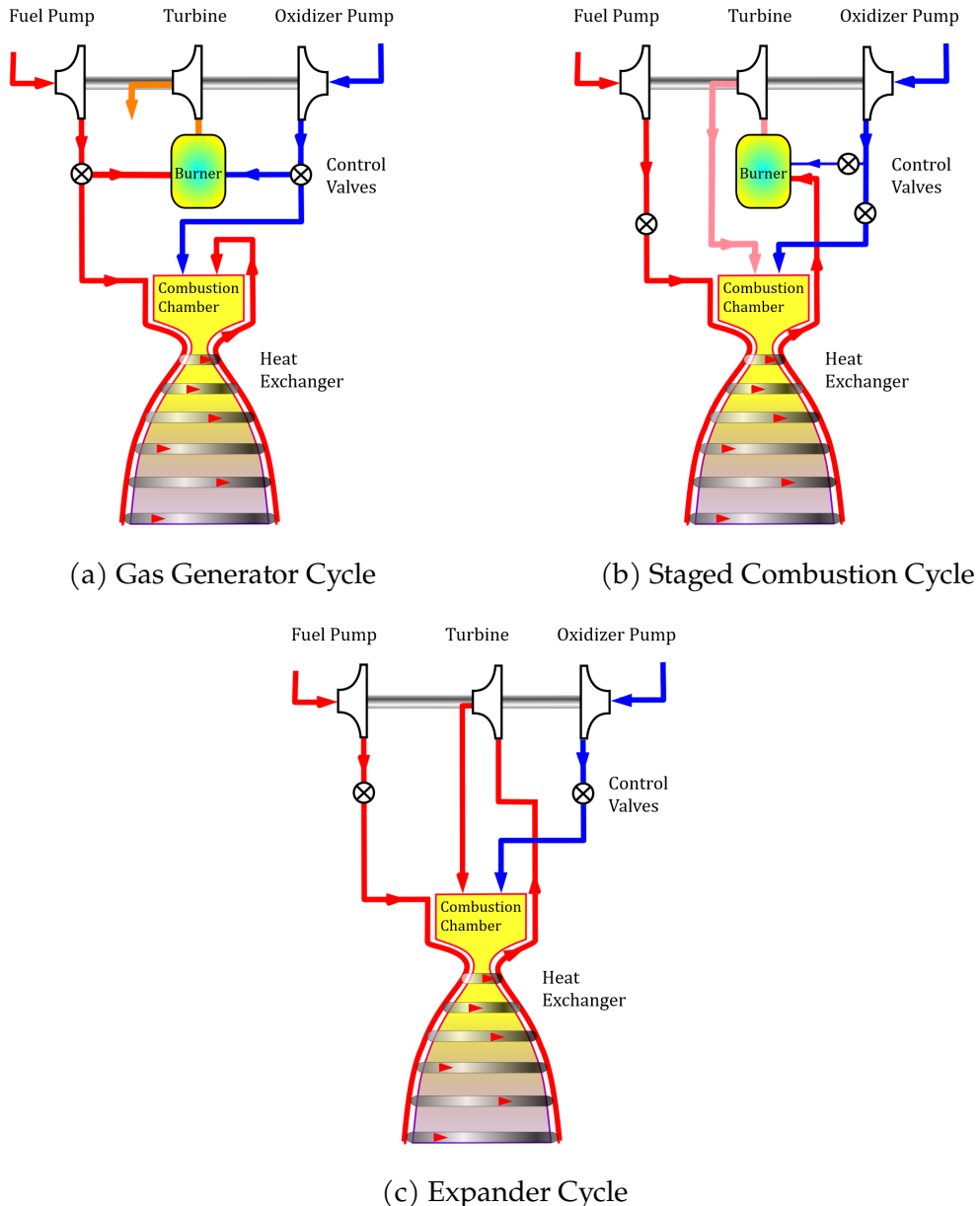


Figure 4.2.: Schematic diagrams of typical turbopump feed system cycles.

Source: Wikimedia Commons

specific turbopump configuration is consequently dependent on factors such as desired flow rate, required discharge pressure, propellant combination, operation duration, throttling range, among others.

The three most common types of turbopump feed systems include the gas generator cycle, the staged combustion cycle and the expander cycle. Schematic diagrams of the engine cycles are shown in figure 4.2.

Gas Generator Cycle

In a gas generator engine cycle, the working fluid constitutes a tiny percentage of the total oxidizer and fuel flow quantities, and undergoes combustion inside the gas-generator in order to generate the high-enthalpy gases for the turbine. The engine derives little performance advantage from the turbine exhaust and subsequently dispenses with the fluid, making the system an open cycle type. The gas generator cycle operates with a high pressure ratio and a low flow rate in order to minimize propellant loss and maximize engine efficiency [45].

Staged Combustion Cycle

In a staged combustion engine cycle, the working fluid comprises a small quantity of one propellant type and a large quantity of the other, and, true to its name, undergoes combustion in stages. The fluid is initially burned inside the preburner, which produces the energetic fuel-rich or oxidizer-rich gas mixture for the turbopump. The entire turbine exhaust fluid is injected into the combustion chamber, along with the remainder propellant, and is eventually burned at the designed bipropellant mixture ratio. A variant of this is the full flow staged combustion engine cycle, where two working fluids, one fuel-rich and another oxidizer-rich, are burned in separate preburners to drive separate turbopump assemblies; both the exhaust fluids are subsequently ducted and injected into the combustion chamber for combustion [42].

Expander Cycle

In an expander cycle, the working fluid consists usually of a cryogenic fuel, such as liquid hydrogen or liquid methane, and flows through the cooling jackets of the thrust chamber. The absorbed heat serves to vaporize and expand the propellant flow and, in the process, produces the gases to power the turbine. The entire exhaust fluid is then either ducted into the combustion chamber (allowing for a high specific impulse) or bled overboard (allowing for a high thrust). Nonetheless, the limited availability of heat for the turbine drive fluid, due to the square–cube rule, limits the turbopump power, which in turn limits the thrust of an expander cycle engine [42].

4.1.3 Electropump Feed Systems

Much like a turbopump feed system, an electropump (a portmanteau for electric-pump or electrically-driven-pump) feed system uses propellant pumps in order

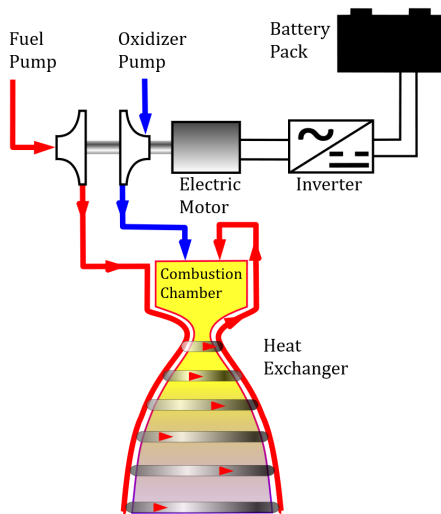


Figure 4.3.: Schematic diagram of a generic electropump feed system.

Source: Wikimedia Commons

to drive the propellants into the combustion chamber. Yet unlike the former, the latter swaps out the gas turbine and utilizes electric motors powered by battery packs in order to run the propellant pumps. The inherent advantage of the system lies in its operational ease owing to its reduced part count, from doing away with the gas turbine and all associated components, and to its lack of complexity, from not having to deal with the high-enthalpy turbine drive fluid.

Nonetheless, the mass penalty from the battery pack had historically been a major bottleneck in the development of electric-pump-fed rocket engines: the battery mass is dictated by both the electrical power and the electrical energy available to drive the propellant pump throughout the burn time of the engine [30] [46]. However, with advancement in battery technologies and refinement in electric motors, adopting such a system has only recently become feasible. This system offers a comparable performance to—or even outperforms—a gas generator cycle engine for applications where the thrust-to-weight ratio is moderate and the operation duration is long [47] [46].

To date, electric pump drive systems have successfully been tested on experimental rocket engines [46]. And yet more remarkably, such an engine cycle has reliably been employed on a small-lift orbital-class launch vehicle called Electron, referred to in figure 1.7 [7]. Developed by Rocket Lab, Electron uses ten Rutherford engines—nine sea-level versions on the booster stage and one vacuum-optimized variant on the upper stage—to loft a payload mass of 300 kg to LEO or 200 kg to

500 km SSO. And the Rutherford is an electric-pump-fed engine, i.e., its propellant pumps are driven by brushless DC motors which are powered from lithium polymer batteries. Running on the LOX/RP-1 combination, the first-stage engine variant produces a thrust of 5600 lbf (roughly 24 kN), delivers a specific impulse of 311 s, and weighs in at 35 kg.

Under the right conditions, as stated in references [48] and [47], an electropump feed system is a viable alternative to both the pressure feed system and the turbopump feed system [30] [46]. Owing to its rather limited flight experience, this project has an impetus to look into the development of such a system for our experimental rocket engine running on liquid oxygen and liquid methane. The schematic diagram of such a system is illustrated in figure 4.3.

4.2 FEED SYSTEM SELECTION CRITERIA

The selection of a propellant feed system for any application is a multifaceted procedure entailing numerous conditions and considerations [12]. Of paramount importance are the features that influence the mission design: bipropellant combination, mixture ratio, propellant physical properties, hardware inert mass, engine reusability, system reliability, engine operating environment, and so on. Of even more importance are factors dependent on the engine operation: thrust, burn duration, combustion chamber pressure, nominal flow rate, feed line pressure losses, and the like. But because the fundamental function of a feed system is to ensure propellant flow into the combustion chamber at the required pressure, basing the selection criteria of the system on combustion chamber pressure is perhaps a prudent approach.

There currently exists a considerable overlap of applicability in the upper limit of pressure feed systems and the lower limit of pump feed systems [13]. Combustion chamber pressures as high as 400 psi and as low as 350 psi have been achieved by employing pressure feed systems and pump feed systems respectively [15]; (1 psi = 6894.757293168 Pa). Yet, just because a feed system can operate near its limits does not make it an ideal choice for a propulsion system. Rather, every feed system type/sub-type has a range of combustion chamber pressures which it is the most suited for [30] [45].

Prior to selecting a feed system, we need to ascertain the combustion chamber pressure for our thrust chamber from its optimum pressure ratio condition. And subsequently, we compare the performance parameters of the selected system with other major types and examine its suitability for our application.

4.2.1 Optimum Pressure Ratio

It has been established that an improved pressure ratio—by increasing the combustion chamber pressure and/or decreasing the nozzle exit pressure—results in an enhanced overall engine performance. Because the exit pressure is dictated by the ambient pressure external to the thrust chamber and can only be modified so much, the usual practice therefore is to raise the chamber pressure. With all other parameters remaining constant, a higher combustion chamber pressure not only increases the thrust coefficient (by reducing the external-to-chamber pressure ratio) but also increases the characteristic velocity (by raising the adiabatic flame temperature) [13]. In addition to directly improving specific impulse and overall thrust, the higher combustion chamber pressure allows for a reduction in the thrust chamber dimensions (for the same nozzle expansion area ratio) by permitting a shorter nozzle divergent section with a smaller nozzle exit diameter, which saves the vehicle inert mass and further enhances its performance [12].

Nonetheless, an unreasonably high combustion chamber pressure comes with disadvantages as well [15] [12]. Firstly, the rate of heat transfer is approximately proportional to the chamber pressure; the increased pressure, thus, raises heat fluxes and thermal stresses on the thrust chamber, thereby necessitating elaborate cooling procedures in order to keep the engine from overheating. Secondly, the power required to drive a propellant pump (in a pump feed system) rises nearly linearly with the chamber pressure; increasing the pressure, thus, marginally reduces the system performance, since the power for the pumps is obtained either from electric motors running on battery packs or from turbines deriving energy from propellant preburners/combustion chambers. And thirdly, as does the combustion chamber pressure increase, so does the inert mass of the propulsion system from, say, increased wall dimensions of ducts and valves or heavier components such as regulators and manifolds. The optimum chamber pressure for a given application is, therefore, a compromise between the higher performance of the propulsion system and the operational complexity of such a system [15] [12].

In order to determine our combustion chamber pressure, we first scrutinize the variation of thrust coefficient and specific impulse with changes in pressure ratio across the nozzle. We preliminarily perform the calculations for a combustion chamber pressure of $P_{cc} = 1000 \text{ psi} = 6894.757 \text{ kPa}$ using CEARUN [39] for liquid oxygen/liquid methane at a mass mixture ratio of 2.75 (assuming optimum expansion, frozen composition flow condition and infinite area combustor option as before). Additionally, we examine how nozzle expansion area ratio varies with pressure ratio, since an area ratio greater than 20 is hardly reasonable for a thrust

chamber operating near sea level [12].

The results are plotted in figures 4.4 and 4.5 respectively. It is observed that a pressure ratio between 75 and 150 delivers good enough performance values for the above combustion chamber pressure [12] [13]: the thrust coefficient is neither too much nor too little for sea level conditions, the specific impulse is about right for atmospheric flight regimes, and the expansion area ratio of less than 15 permits room for a cluster of thrust chambers on the booster stage.

4.2.2 Combustion Chamber Pressure

With pressure ratios across the nozzle narrowed down, we cannot help but realize from figure 4.5 that the nozzle exit pressure drops below the ambient sea level pressure even towards the lower pressure ratios. A substantial decrease in exit pressure, to around 25 to 35% of local ambient pressure, does result in flow separation instabilities (along with compression wave formation) within the divergent nozzle section [13]; and during start and stop transients when the thrust is not always axially symmetric, such instabilities may momentarily produce side loads on the nozzle wall from uneven oscillations of the exhaust jet, which potentially can damage the nozzle due to excessive forces and resonant frequencies [12]. Even a slight decrease in exit pressure contributes to a noticeable reduction in thrust and specific impulse from the thrust chamber.

In order to forestall flow separation without having to adopt an unreasonably high chamber pressure, we need a minimum exit pressure that is nearly 40% of the ambient pressure at sea level. We examine numerous combinations of exit pressures (from 0.4 atm to 0.8 atm) and pressure ratios (from 75 to 150) to obtain our chamber pressure (between 30 bar and 120 bar), and compare the values with resultant area ratio (between 14 and 16). This helps us corroborate our engine parameters with those of prior successful engines of similar configurations.

With a nozzle exit pressure of $P_e = 40$ kPa, we tentatively opt for a pressure ratio of 150, and settle on a combustion chamber pressure of $P_{cc} = 6000$ kPa (= 60 bar); this yields an expansion area ratio of about 15. We finally run CEA again to verify values of all the metrics calculated/considered thus far for sea level operation, and summarize the results in table 4.1.

Having selected the chamber pressure helps us decide between the type/sub-type of feed system best suited for our application. And the selected mixture ratio in conjunction with propellant flow rates lets us design and/or determine the pumps' components and/or parameters, if need be.

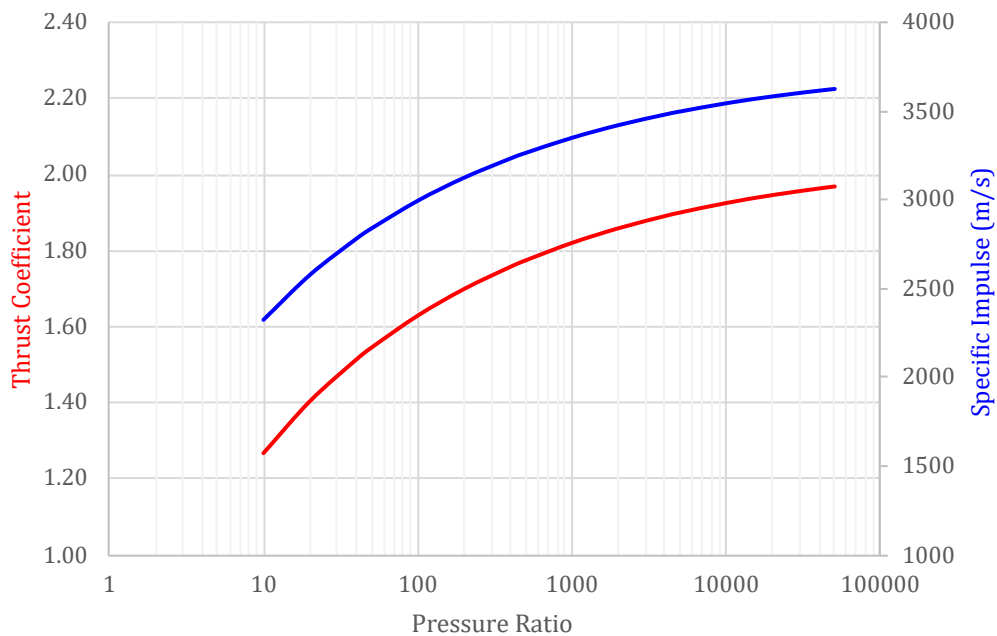


Figure 4.4.: Variation of thrust coefficient and specific impulse with pressure ratio.
 $P_{cc} = 1000 \text{ psi} = 6894.757 \text{ kPa}$.

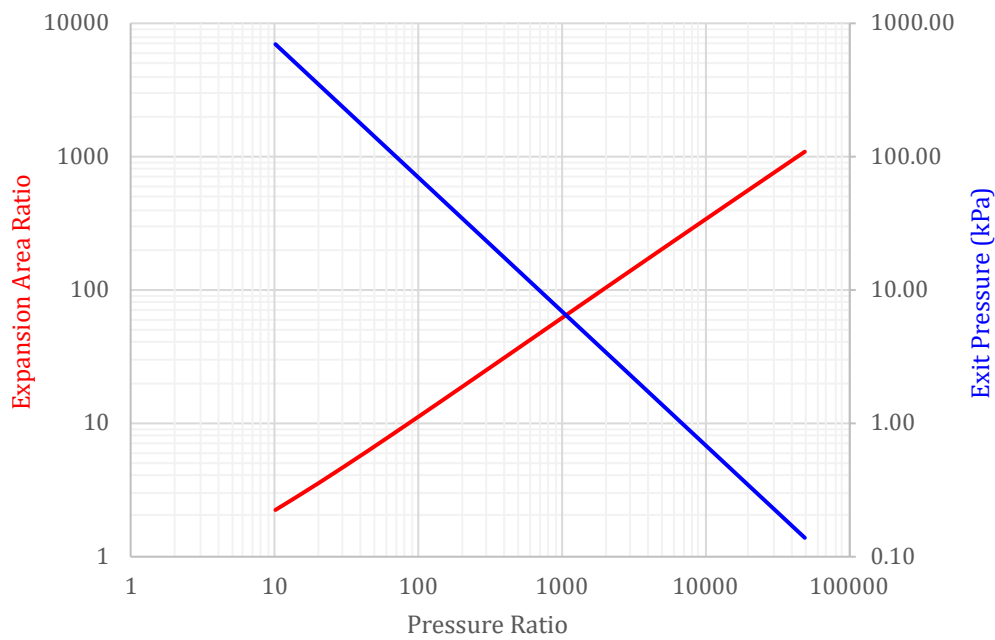


Figure 4.5.: Variation of nozzle expansion area ratio and nozzle exit pressure with pressure ratio. $P_{cc} = 1000 \text{ psi} = 6894.757 \text{ kPa}$.

Table 4.1.: Preliminary parameters for thrust chamber operation at sea level. [39]

Oxidizer	Liquid oxygen	
Fuel	Liquid methane	
Mixture ratio O/F	2.75	
Combustion chamber pressure P_{cc}	6000	kPa
Specific impulse I_s	3068.30	m/s
Thrust coefficient C_f	1.6723	
Characteristic velocity c^*	1834.80	m/s
Nozzle exit pressure P_e	40	kPa
Pressure ratio P_{cc}/P_e	150	
Nozzle expansion area ratio ϵ	14.966	

4.3 SUITABILITY OF FEED SYSTEMS

As specified earlier, the objective of our hypothetical mission is to deliver a light payload into LEO using a two-stage rocket. The delta-v budget of the launch vehicle is 9500 m/s, with the assumed delta-v distribution as 4500 m/s for the first stage and 5000 m/s for the second stage. And delta-v—the most significant parameter in the performance assessment of a launch vehicle—is immensely influenced by the mass ratio of a rocket stage. In order to minimize inert mass and/or maximize payload capacity, evaluation of the feed system mass serves as the foundation for establishing its suitability for our application. The analysis for doing so follows the framework laid out in references [48], [47] and [46].

4.3.1 Pressure Feed System

The practicality of a pressure feed system is considered first. This project intends to operate our experimental engine not only on the upper stage but also on the booster stage of our launch vehicle. And a pressure feed system powering the first stage of a rocket is hitherto unheard of.

This is because, in order to preclude undesirable flow separation instabilities, a thrust chamber operating from the sea level can afford a minimum nozzle exit

pressure of around, or only slightly below, 0.4 atm (40.530 kPa). This means that, for any decent values of thrust coefficient and specific impulse (for the LOX/LCH₄ propellant combination), the propulsion system can have a minimum combustion chamber pressure of roughly 75 times the nozzle exit pressure. This in turn implies that, even with a minimum propellant tank pressurization of nearly 1.5 times the combustion chamber pressure (to ensure adequate flow rate and injection pressure into the chamber [13]), the tank pressurization can become immoderately high. So, for a chamber pressure of, say, 3000 kPa, the required tank pressurization can be upwards of 4500 kPa. Again, the pressurization required for pressurant tanks can easily be manyfold more [48] [13].

Moreover, mass of the propellant tank (for a given wall material density) is determined by both its surface area (from its volume) and its wall thickness, which in turn are dictated by the propellant mass and the Laplace's law respectively [48]. Again, added to that mass is the mass of the pressurant tank. Now, for high-total-impulse applications (like at liftoff, where the propellant mass is monumental and at its maximum), an inordinately high mass from the propellant tank(s) exacerbates the propellant mass fraction and does not lend itself to good delta-v values for the stage.

Merely through qualitative reasoning and without much quantitative inspection, it can unequivocally be asserted that employing the pressure feed system for our rocket engine would not result in a sound solution. Therefore, we disregard this engine cycle and consider the pump feed systems for our application.

4.3.2 Turbopump Feed System

The feasibility of a turbopump feed system is examined here. Turbopump cycle engines are capable of accomplishing the highest figures in terms of thrust, thrust-to-weight ratio or combustion chamber pressure, as is evident from engines such as the RD-170 (highest thrust engine), the F-1 (highest thrust single-chamber engine), the Merlin (highest thrust-to-weight ratio engine) and the Raptor (highest combustion chamber pressure engine). For more moderate performance requirements, however, turbopump-fed engines are oftentimes bested by the other engine cycles. Regardless, we follow the convention here and predicate the gas generator cycle as the benchmark for good performance.

For the evaluation of overall mass, only masses of the major components are considered while those of the minor and common components are neglected. It is to be noted that helium is used as the pressurant fluid here for pressurizing both

oxidizer and fuel tanks and preventing cavitation in the propellant pumps.

The mass of the turbopump feed system (TPFS) is defined as the combined masses of oxidizer (o), fuel (f), pressurant (prs), oxidizer tank (o.t), fuel tank (f.t), pressurant tank (prs.t), turbopump assembly (tp) and gas generator (gg).

$$\begin{aligned} m_{TPFS} = & m_o + m_f + m_{prs} + m_{o.t} + m_{f.t} + m_{prs.t} \\ & + m_{tp} + m_{gg} \end{aligned} \quad (4.1)$$

Turbopump Assembly Mass

Assuming no mechanical losses between the turbine and the pumps, the turbopump power equals the power generated from the turbine or the power consumed by the pumps.

$$p_{tp} = p_{tu} = p_{pu} = p_{o.p} + p_{f.p} \quad (4.2)$$

The turbopump power is proportional to the propellant mass flow rate times the head rise in both the pumps [46].

$$p_{tp} = \frac{\dot{m}_{o.p} \Delta P_{o.p}}{\eta_{o.p} \rho_o} + \frac{\dot{m}_{f.p} \Delta P_{f.p}}{\eta_{f.p} \rho_f} \quad (4.3)$$

where, $\dot{m}_{o.p}$, $\dot{m}_{f.p}$, $\Delta P_{o.p}$, $\Delta P_{f.p}$, $\eta_{o.p}$ and $\eta_{f.p}$ represent mass flow rates, head rises and efficiencies for both the propellant pumps respectively.

Because turbopump mass is related to its power via its power density (power per unit mass), the turbopump mass can be expressed in terms of mass flow rate and pump head rise as [46]

$$\begin{aligned} m_{tp} &= \frac{1}{\delta_{tp}} p_{tp} = \frac{1}{\delta_{tp}} p_{tu} = \frac{1}{\delta_{tp}} (p_{o.p} + p_{f.p}) \\ &= \frac{1}{\delta_{tp}} \left(\frac{\dot{m}_{o.p} \Delta P_{o.p}}{\eta_{o.p} \rho_o} + \frac{\dot{m}_{f.p} \Delta P_{f.p}}{\eta_{f.p} \rho_f} \right) \end{aligned} \quad (4.4)$$

Gas Generator Mass

Mass of the gas generator is proportional to its volume and its wall thickness.

The gas generator volume can be determined by the stay time t_s method as

$$V_{gg} = \frac{\dot{m}_{gg} t_s}{\rho_{gg}} \quad (4.5)$$

where, \dot{m}_{gg} and ρ_{gg} are the mass flow rate and the density of the gas generator working fluid respectively.

And assuming a spherical shape, the gas generator mass can be expressed as [46]

$$m_{gg} = \frac{3}{2} \frac{\rho_{gg.m}}{\sigma_{gg.m}} \frac{\dot{m}_{gg} t_s}{\rho_{gg}} P_{gg} \kappa_{gg} \quad (4.6)$$

where, $\rho_{gg.m}$, $\sigma_{gg.m}$, P_{gg} and κ_{gg} represent material density, material yield strength, pressure and structural safety factor of the gas generator respectively.

Now, for a single stage supersonic impulse turbine undergoing an adiabatic process, the turbine power is given as

$$p_{tu} = \dot{m}_{gg} c_{P,gg} \eta_{tu} T_{tu.inlet} \left(1 - \left(\frac{P_{tu.inlet}}{P_{tu.outlet}} \right)^{\left(\frac{1-k_{gg}}{k_{gg}} \right)} \right) \quad (4.7)$$

where, $c_{P,gg}$, k_{gg} , T_{tu} and P_{tu} are specific heat of constant pressure, specific heat ratio, turbine temperature and turbine pressure respectively. The subscript gg here represents the gas generator working fluid.

Propellant Masses

The mass of each propellant consumed for propulsion is proportional to the mass flow rate through its pump and the burn time t_b of the engine [46].

$$m_o = \dot{m}_{o,p} t_b \kappa_p \quad (4.8a)$$

$$m_f = \dot{m}_{f,p} t_b \kappa_p \quad (4.8b)$$

where, κ_p represents the margin of residual propellant mass trapped inside pipes, valves, fittings, filters, pumps, etc. after engine operation.

The total propellant mass therefore is given as

$$\begin{aligned} m_p &= m_o + m_f \\ &= (\dot{m}_{o,p} + \dot{m}_{f,p}) t_b \kappa_p \end{aligned} \quad (4.9)$$

Propellant Tank Masses

Mass of a propellant tank can be expressed as the product of its surface area, its wall thickness and its material density.

For the sake of simplicity, it is assumed that each propellant tank is spherical. Additionally, it is assumed that the pressurant tank is immersed and integrated inside the oxidizer tank, as is common practice for propellant tank arrangements.

Volumes of the oxidizer tank and the fuel tank are, therefore, defined as

$$V_{o.t} = V_o \kappa_u + V_{prs.t} \quad (4.10a)$$

$$V_{f.t} = V_f \kappa_u \quad (4.10b)$$

where, κ_u is a factor representing the ullage volume within the tank.

Thus, radius and surface area of the oxidizer tank, respectively, can be written in terms of its volume as

$$r_{o.t} = \left(\frac{3}{4\pi} V_{o.t} \right)^{1/3} \quad (4.11a)$$

$$S_{o.t} = 4\pi \left(\frac{3}{4\pi} V_{o.t} \right)^{2/3} \quad (4.11b)$$

Now, the maximum pressure exerted on the lower and the upper hemispheres of the propellant tank is different due to differences in fluid head from different loading conditions, and can be expressed as [46]

$$P_{o.t.lower} = P_{o.t.internal} + \rho_o g_{max} h_{o.initial} \quad (4.12a)$$

$$P_{o.t.upper} = P_{o.t.internal} + \rho_o g_{max} (h_{o.initial} - r_{o.t}) \quad (4.12b)$$

where, $P_{o.t.internal}$, g_{max} and $h_{o.initial}$ represent internal tank pressure, maximum vehicle acceleration and initial fluid head respectively. Consequently, the thickness of the lower and the upper tank hemispheres is different, and can be calculated from the thin wall theory.

Mass of the oxidizer tank can, therefore, be expressed as

$$m_{o.t} = \frac{3}{4} \frac{\rho_{o.t.m}}{\sigma_{o.t.m}} \kappa_t V_{o.t} (P_{o.t.lower} + P_{o.t.upper}) \quad (4.13)$$

Mass of the fuel tank can, likewise, be expressed as

$$m_{f.t} = \frac{3}{4} \frac{\rho_{f.t.m}}{\sigma_{f.t.m}} \kappa_t V_{f.t} (P_{f.t.lower} + P_{f.t.upper}) \quad (4.14)$$

Pressurant Mass

In order to suppress cavitation within the propellant pumps, it is necessary to pressurize both the propellant tanks up to the required pump inlet pressure. Mass of the pressurant fluid can be determined assuming ideal gas and adiabatic expansion properties.

$$m_{prs} = \kappa_{prs} \frac{k_{prs}}{R_{prs} T_{prs.initial}} \left(\frac{PV}{1 - \frac{P_{prs.final}}{P_{prs.initial}}} \right) \quad (4.15)$$

where, κ_{prs} , k_{prs} , R_{prs} , T_{prs} and P_{prs} represent mass margin, specific heat ratio, gas constant, temperature and pressure of the pressurant fluid respectively.

Additionally, P and V above represent propellant tank internal pressure and propellant volume, expanding which for both the oxidizer and the fuel yields [46]

$$m_{prs} = \kappa_{prs} \kappa_u \frac{k_{prs}}{R_{prs} T_{prs.initial}} \left(\frac{P_{o.t.internal} V_o + P_{f.t.internal} V_f}{1 - \frac{P_{prs.final}}{P_{prs.initial}}} \right) \quad (4.16)$$

Pressurant Tank Mass

Volume of the pressurant tank is given as

$$V_{prs.t} = m_{prs} R_{prs} \frac{T_{prs.initial}}{P_{prs.initial}} \quad (4.17)$$

And assuming a spherical pressurant tank, mass of the tank can thus be expressed as [46]

$$m_{prs.t} = \frac{3}{2} \frac{\rho_{prs.t.m}}{\sigma_{prs.t.m}} \kappa_{prs.t} \kappa_{prs} \kappa_u k_{prs} \left(\frac{P_{o.t.internal} V_o + P_{f.t.internal} V_f}{1 - \frac{P_{prs.final}}{P_{prs.initial}}} \right) \quad (4.18)$$

where, $\kappa_{prs.t}$, $\rho_{prs.t.m}$ and $\sigma_{prs.t.m}$ represent mass margin, material density and material yield strength of the pressurant tank respectively.

Turbopump Feed System Mass

Total mass of the turbopump feed system, therefore, may be obtained from substituting the individual mass expressions above in the equation 4.1. The total turbopump feed system mass, expressed here in terms of pump power and burn-

ing time after rearranging and recombining the above expressions, is as follows

$$\begin{aligned} m_{TPFS} = & \left(\frac{1}{\delta_{tp}} + X_1 P_{gg} \right) \left(\frac{\dot{m}_{o,p} \Delta P_{o,p}}{\eta_{o,p} \rho_o} + \frac{\dot{m}_{f,p} \Delta P_{f,p}}{\eta_{f,p} \rho_f} \right) \\ & + \left(X_o + \kappa_p \rho_o + P_{o.t.internal} (X_2 + X_o X_3) \right) \frac{\dot{m}_{o,p} t_b}{\rho_o} \\ & + \left(X_f + \kappa_p \rho_f + P_{f.t.internal} (X_2 + X_f X_3) \right) \frac{\dot{m}_{f,p} t_b}{\rho_f} \end{aligned} \quad (4.19)$$

where, the new variables can be expanded as

$$X_o = \kappa_p \kappa_u \kappa_t \frac{3}{4} \frac{\rho_{o.t.m}}{\sigma_{o.t.m}} (P_{o.t.lower} + P_{o.t.upper}) \quad (4.20)$$

$$X_f = \kappa_p \kappa_u \kappa_t \frac{3}{4} \frac{\rho_{f.t.m}}{\sigma_{f.t.m}} (P_{f.t.lower} + P_{f.t.upper}) \quad (4.21)$$

$$X_1 = \frac{3}{2} \frac{\rho_{gg.m}}{\sigma_{gg.m}} \frac{\kappa_{gg} t_s}{\rho_{gg}} \left[c_{P.gg} \eta_{tu} T_{tu.inlet} \left(1 - \left(\frac{P_{tu.inlet}}{P_{tu.outlet}} \right)^{\left(\frac{1-k_{gg}}{k_{gg}} \right)} \right) \right]^{-1} \quad (4.22)$$

$$X_2 = \kappa_p \kappa_u \kappa_{prs} \left(\frac{k_{prs}}{1 - \frac{P_{prs.final}}{P_{prs.initial}}} \right) \left(\frac{1}{R_{prs} T_{prs.initial}} + \frac{3}{2} \frac{\rho_{prs.t.m}}{\sigma_{prs.t.m}} \kappa_{prs.t} \right) \quad (4.23)$$

$$X_3 = \frac{\kappa_{prs} k_{prs}}{P_{prs.initial} - P_{prs.final}} \quad (4.24)$$

4.3.3 Electropump Feed System

The viability of an electropump feed system is scrutinized now. As mentioned before, the lack of a breakthrough in battery technology over the recent decades has perhaps been the greatest impediment in the widespread adoption of electric vehicles—from rockets and airplanes to cars and boats [49] [50]. Yet, as is established in references [48], [47] and [46], and as is evident from the launch vehicle Electron [7], electropump feed systems are indeed practicable under the proper circumstances and/or requirements of engine operation. Our objective, therefore, is to optimize the performance parameters from the electropump feed system.

Among the most crucial factors dictating the mass of a battery pack is its critical density in terms of both power and energy. Both power and energy are in turn influenced by the required discharge time of the battery pack. Again, because the efficiency of a battery cell is rather sensitive to its environmental temperature,

the use of a coolant (usually the fuel) to keep the battery pack within the desired temperature range becomes a necessity.

For the mass of the electropump feed system (EPFS), the masses of oxidizer (o), fuel (f), pressurant (prs), oxidizer tank (o.t), fuel tank (f.t), pressurant tank (prs.t), oxidizer pump (o.p), fuel pump (f.p), electric motor (mot), inverter (inv) and battery pack (bat) are considered.

$$\begin{aligned} m_{EPFS} = & m_o + m_f + m_{prs} + m_{o.t} + m_{f.t} + m_{prs.t} \\ & + m_{o.p} + m_{f.p} + m_{mot} + m_{inv} + m_{bat} \end{aligned} \quad (4.25)$$

Propellant Pump Masses

As described for the turbopump assembly mass, mass of each propellant pump is related to its power via its power density, and can be expressed in terms of mass flow rate and pump head rise [46].

$$m_{o.p} = \frac{p_{o.p}}{\delta_{o.p}} = \frac{1}{\delta_{o.p}} \frac{\dot{m}_{o.p} \Delta P_{o.p}}{\eta_{o.p} \rho_o} \quad (4.26a)$$

$$m_{f.p} = \frac{p_{f.p}}{\delta_{f.p}} = \frac{1}{\delta_{f.p}} \frac{\dot{m}_{f.p} \Delta P_{f.p}}{\eta_{f.p} \rho_f} \quad (4.26b)$$

Electric Motor Mass

Assuming no mechanical losses between the motor and the pumps, the output power from the motor equals the power consumed by both the propellant pumps. For a motor mechanical output power density δ_{mot} , mass of the motor is given as

$$m_{mot} = \frac{1}{\delta_{mot}} p_{mot.output} = \frac{1}{\delta_{mot}} (p_{o.p} + p_{f.p}) \quad (4.27)$$

Inverter Mass

Now, the efficiency of the motor is defined as the ratio of motor mechanical output power to inverter electrical output power [46]. Likewise, the inverter efficiency is the ratio of its electrical output power to its electrical input power [46].

$$\eta_{mot} = \frac{p_{mot.output}}{p_{inv.output}} \quad (4.28a)$$

$$\eta_{inv} = \frac{p_{inv.output}}{p_{inv.input}} \quad (4.28b)$$

Mass of the inverter is therefore given as [46]

$$\begin{aligned} m_{inv} &= \frac{1}{\delta_{inv}} p_{inv.output} = \frac{1}{\delta_{inv} \eta_{mot}} p_{mot.output} \\ &= \frac{1}{\delta_{inv} \eta_{mot}} (p_{o.p} + p_{f.p}) \end{aligned} \quad (4.29)$$

Battery Pack Mass

A battery is constrained in both its power and its energy capacities. Therefore, depending on the requirement for either power or energy, either power density or energy density dictates the mass of a battery pack.

The electrical power of the battery pack required to run the propellant pumps is given as [46]

$$\begin{aligned} p_{bat} &= p_{inv.input} = \frac{1}{\eta_{inv} \eta_{mot}} p_{mot.output} \\ &= \frac{1}{\eta_{inv} \eta_{mot}} (p_{o.p} + p_{f.p}) \end{aligned} \quad (4.30)$$

Likewise, the electrical energy required to run the pumps for the entire engine operation duration t_b is given as [46]

$$\begin{aligned} e_{bat} &= \frac{1}{\eta_{bat}} t_b p_{bat} \\ &= \frac{1}{\eta_{bat} \eta_{inv} \eta_{mot}} t_b (p_{o.p} + p_{f.p}) \end{aligned} \quad (4.31)$$

where, η_{bat} is the energy efficiency of the battery.

Upon introducing power density $\delta_{bat,p}$ and energy density $\delta_{bat,e}$ of the battery, the power-constrained mass and the energy-constrained mass of the battery pack can, respectively, be expressed as [46]

$$m_{bat,p} = \frac{1}{\delta_{bat,p}} \kappa_{bat} p_{bat} = \frac{1}{\delta_{bat,p} \eta_{inv} \eta_{mot}} \kappa_{bat} (p_{o.p} + p_{f.p}) \quad (4.32a)$$

$$m_{bat,e} = \frac{1}{\delta_{bat,e}} \kappa_{bat} e_{bat} = \frac{1}{\delta_{bat,e} \eta_{bat} \eta_{inv} \eta_{mot}} \kappa_{bat} t_b (p_{o.p} + p_{f.p}) \quad (4.32b)$$

In the equations 4.32, κ_{bat} represents a mass margin adopted to account for the necessary sub-component masses of the battery pack, such as battery management

systems, wires, casing, etc.

Mass of the battery pack is therefore given as

$$\begin{aligned} m_{bat} &= \text{MAX} [m_{bat.p}, m_{bat.e}] \\ &= \frac{1}{\eta_{inv} \eta_{mot}} \kappa_{bat} (p_{o.p} + p_{f.p}) \text{MAX} \left[\frac{1}{\delta_{bat.p}}, \frac{t_b}{\delta_{bat.e} \eta_{bat}} \right] \end{aligned} \quad (4.33)$$

Propellant Masses

Now, because no quantity of propellant from the pump outlet is diverted out into the gas generator before being exhausted overboard, the revised oxidizer and fuel masses for the electropump cycle can be given as

$$m_o = (\dot{m}_{o,p} - \dot{m}_{o,gg}) t_b \kappa_p \quad (4.34a)$$

$$m_f = (\dot{m}_{f,p} - \dot{m}_{f,gg}) t_b \kappa_p \quad (4.34b)$$

where, $\dot{m}_{o,gg}$ and $\dot{m}_{f,gg}$ represent oxidizer and fuel mass flow rates through the gas generator, and can be computed using \dot{m}_{gg} and the mixture ratio (O/F)_{gg} of the gas generator working fluid. The gas generator mass flow rate typically varies between 1 to 7% of the total propellant flow [12] [13].

Electropump Feed System Mass

For masses of the other four terms in the equation 4.25, the same expressions from the turbopump feed system mass can be applied. Therefore, total mass of the electropump feed system, expressed in terms of pump power and burning time as before, is as follows

$$\begin{aligned} m_{EPFS} &= \left(\frac{1}{\delta_{o,p}} + X_4 \right) \left(\frac{\dot{m}_{o,p} \Delta P_{o,p}}{\eta_{o,p} \rho_o} \right) + \left(\frac{1}{\delta_{f,p}} + X_4 \right) \left(\frac{\dot{m}_{f,p} \Delta P_{f,p}}{\eta_{f,p} \rho_f} \right) \\ &\quad + (X_o + \kappa_p \rho_o + P_{o.t.internal} (X_2 + X_o X_3)) \frac{(\dot{m}_{o,p} - \dot{m}_{o,gg}) t_b}{\rho_o} \\ &\quad + (X_f + \kappa_p \rho_f + P_{f.t.internal} (X_2 + X_f X_3)) \frac{(\dot{m}_{f,p} - \dot{m}_{f,gg}) t_b}{\rho_f} \end{aligned} \quad (4.35)$$

where, the new variable can be expanded as

$$X_4 = \frac{1}{\delta_{mot}} + \frac{1}{\delta_{inv} \eta_{mot}} + \frac{1}{\eta_{inv} \eta_{mot}} \kappa_{bat} \text{MAX} \left[\frac{1}{\delta_{bat.p}}, \frac{t_b}{\delta_{bat.e} \eta_{bat}} \right] \quad (4.36)$$

4.3.4 Analysis of the Feed System Mass

For a comparative evaluation of both the feed system masses, we neglect every common element between the systems and enumerate specifications for each parameter above. The two total mass expressions stated in their respective exclusive terms are presented again below.

$$\begin{aligned}
 m_{TPFS} &= m_o + m_f + m_{tp} + m_{gg} \\
 &= \dot{m}_{o,p} t_b \kappa_p \\
 &\quad + \dot{m}_{f,p} t_b \kappa_p \\
 &\quad + \frac{1}{\delta_{tp}} \left(\frac{\dot{m}_{o,p} \Delta P_{o,p}}{\eta_{o,p} \rho_o} + \frac{\dot{m}_{f,p} \Delta P_{f,p}}{\eta_{f,p} \rho_f} \right) \\
 &\quad + \frac{3 \rho_{gg,m} \dot{m}_{gg} t_s}{2 \sigma_{gg,m} \rho_{gg}} P_{gg} \kappa_{gg}
 \end{aligned} \tag{4.37}$$

$$\begin{aligned}
 m_{EPFS} &= m_o + m_f + m_{o,p} + m_{f,p} + m_{mot} + m_{inv} + m_{bat} \\
 &= \left(\dot{m}_{o,p} - \dot{m}_{gg} \frac{(O/F)_{gg}}{(O/F)_{gg} + 1} \right) t_b \kappa_p \\
 &\quad + \left(\dot{m}_{f,p} - \dot{m}_{gg} \frac{1}{(O/F)_{gg} + 1} \right) t_b \kappa_p \\
 &\quad + \frac{1}{\delta_{o,p}} \frac{\dot{m}_{o,p} \Delta P_{o,p}}{\eta_{o,p} \rho_o} \\
 &\quad + \frac{1}{\delta_{f,p}} \frac{\dot{m}_{f,p} \Delta P_{f,p}}{\eta_{f,p} \rho_f} \\
 &\quad + \frac{1}{\delta_{mot}} \left(\frac{\dot{m}_{o,p} \Delta P_{o,p}}{\eta_{o,p} \rho_o} + \frac{\dot{m}_{f,p} \Delta P_{f,p}}{\eta_{f,p} \rho_f} \right) \\
 &\quad + \frac{1}{\delta_{inv} \eta_{mot}} \left(\frac{\dot{m}_{o,p} \Delta P_{o,p}}{\eta_{o,p} \rho_o} + \frac{\dot{m}_{f,p} \Delta P_{f,p}}{\eta_{f,p} \rho_f} \right) \\
 &\quad + \frac{1}{\eta_{inv} \eta_{mot}} \kappa_{bat} \left(\frac{\dot{m}_{o,p} \Delta P_{o,p}}{\eta_{o,p} \rho_o} + \frac{\dot{m}_{f,p} \Delta P_{f,p}}{\eta_{f,p} \rho_f} \right) \text{MAX} \left[\frac{1}{\delta_{bat,p}}, \frac{t_b}{\delta_{bat,e} \eta_{bat}} \right]
 \end{aligned} \tag{4.38}$$

From the values laid out in references [48], [47] and [46], we obtain power densities for the turbopump, the oxidizer pump and the fuel pump as 12.50 kW/kg, 20 kW/kg and 15 kW/kg respectively. The efficiencies of the oxidizer pump and the fuel pump are adopted as 0.66 and 0.60 respectively, and both their pressure increments are assumed to be 1.25 $P_{cc} = 7500$ kPa and 1.50 $P_{cc} = 9000$ kPa respectively; the additional pressure is necessary to account for any pressure drop within

the injector assembly as well as, in case of fuel, within the thrust chamber heat exchanger.

Now, power density and efficiency of the electric motor are taken as 5.50 kW/kg and 0.95 respectively. The electric motor used is a permanent magnet synchronous motor (PMSM) with a rated power of around 340 kW and a rotational speed of about 45000 rpm. Likewise, power density and efficiency of the inverter are taken as 60 kW/kg and 0.85 respectively. The inverter properties are assumed the same as in the study [47].

For the battery pack, the structural mass margin is assumed to be 25%. Desirable characteristics of the battery cell include both higher power densities and higher energy densities for a lighter battery pack. A lithium polymer cell with an efficiency of 0.90, a power density of 6.50 kW/kg and an energy density of 300 Wh/kg is therefore adopted.

For the gas generator subassemblies, we use Inconel 625 [51] as the construction material, which has a yield strength of 500 MPa and a density of 8440 kg/m³, and opt for a structural safety factor of 2.50. A mass mixture ratio of 0.333 is selected for the gas generator working fluid, which corresponds to a density of 12.624 kg/m³; the fuel rich mixture ensures a low combustion temperature of 931.41 K and averts any erosion of the turbine blades [39]. Referring to [12] and [13], we adopt a working fluid mass flow rate of 0.0075 times the total propellant flow rate through the thrust chamber.

The mass margin for residual propellant after the thrust chamber operation is rationally assumed to be 5%. The pressure within the gas generator is considered same as that within the combustion chamber, while the stay time of the working fluid is assumed to be 0.01 s. The operation duration for the rocket engine is varied from 0 s to 1000 s so as to analyse the mass dependence of both the feed systems on engine burn time.

All pertinent specifications considered thus far are summarized in table 4.2, with the attendant plots from our calculations presented further below. From figure 4.6, we can observe that the mass of the feed system (i.e., the entire pump feed system mass without the thrust chamber propellant mass) varies, for the most part, linearly with the engine burn duration. This is because, for the turbopump system, the gas generator working fluid mass is directly proportional to the burn time and outweighs the combined masses of other feed system components. In case of the electropump system, however, the battery pack mass dominates the masses of all other feed system components and is dictated by its critical parameter in terms of

Table 4.2.: Specifications used for the estimation of feed system mass.

Oxidizer Pump		
Power density $\delta_{o,p}$	20.00	kW/kg
Efficiency $\eta_{o,p}$	0.66	
Pressure increment $\Delta P_{o,p}$	7500	kPa
Fuel Pump		
Power density $\delta_{f,p}$	15.00	kW/kg
Efficiency $\eta_{f,p}$	0.60	
Pressure increment $\Delta P_{f,p}$	9000	kPa
Electric Motor		
Power density δ_{mot}	5.50	kW/kg
Efficiency η_{mot}	0.95	
Inverter		
Power density δ_{inv}	60.00	kW/kg
Efficiency η_{inv}	0.85	
Battery Pack		
Power density $\delta_{bat,p}$	6.50	kW/kg
Energy density $\delta_{bat,e}$	300.00	Wh/kg
Efficiency η_{bat}	0.90	
Mass margin κ_{bat}	25%	
Turbopump Assembly		
Power density δ_{tp}	12.50	kW/kg
Gas Generator		
Material density $\rho_{gg,m}$	8440	kg/m ³
Material strength $\sigma_{gg,m}$	500	MPa
Safety factor κ_{gg}	2.50	
Gas Generator Working Fluid		
Mixture ratio $(O/F)_{gg}$	0.333	
Density ρ_{gg}	12.624	kg/m ³
Mass flow rate \dot{m}_{gg}	0.08	kg/s
Stay time t_s	0.01	s
Mass margin κ_p	5%	

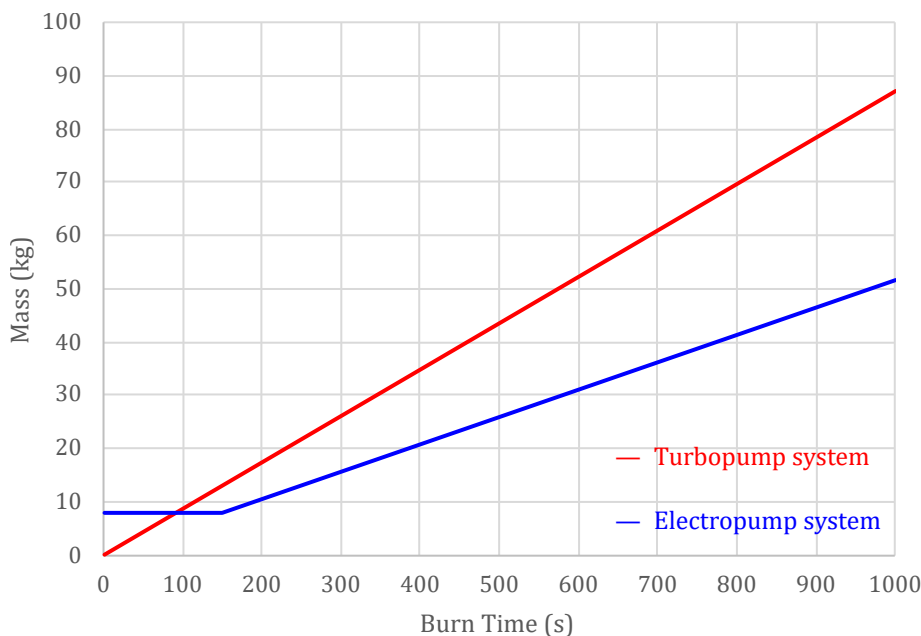


Figure 4.6.: Variation of mass of both the feed systems (without thrust chamber propellant) with engine burn time.

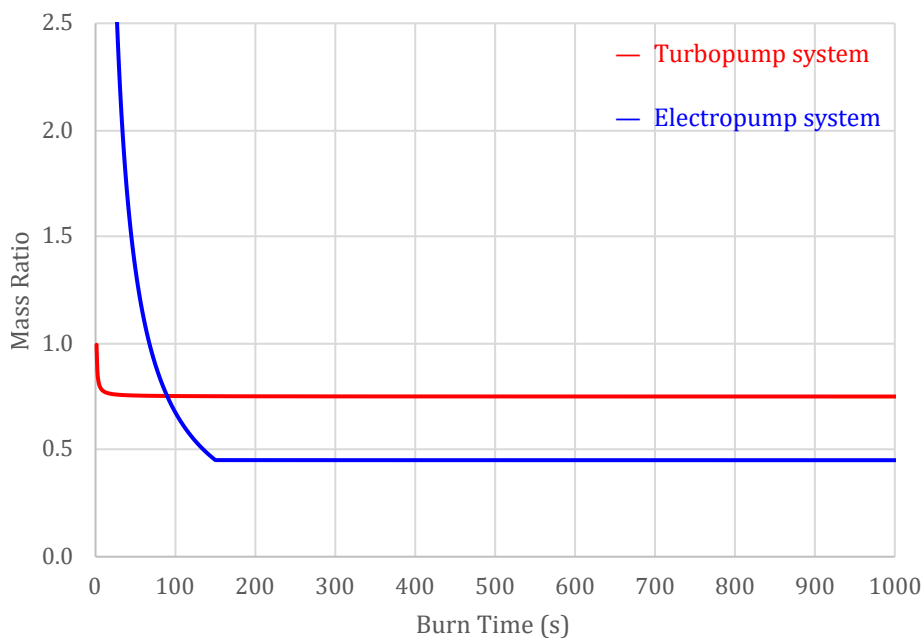


Figure 4.7.: Variation of the ratio of feed system mass to thrust chamber propellant mass with engine burn time.

both power and energy densities. When the burn times are short, the minimum battery cell discharge time imposed from its critical power density warrants the need for a larger number, and thus mass, of battery cells for the engine operation; this is evident from the horizontal segment of the electropump system plot in figure 4.6. For long burn times, the functional energy capacity of the battery pack, which is proportional to the energy necessary for engine operation, establishes the total mass of the battery pack. In our case, the switch from critical power density to critical energy density occurs around 150 s.

Figure 4.7 illustrates the variation of the ratio of feed system mass to thrust chamber propellant mass as a function of engine operation duration. Noticeably, the power-imposed and the energy-imposed burn times for the electropump system are signified by the curved and the straight sections of the plot. Overall, we recognize that, for our configuration of the feed systems, the mass fraction of the turbopump system is lighter than that of the electropump system up to a burn time of about 88 s after which the electric pump feed system yields a lighter overall mass.

These results conclusively validate that an electric-pump-fed engine cycle can indeed outperform a turbopump feed system under the proper circumstances of engine operation. Since typical rocket engine burn durations vary anywhere between 180 s and 300 s, our feed system is never constrained by the power density of the battery pack. We, therefore, unqualifiedly employ the above configuration of the electropump feed system for our liquid rocket propulsion system requirements.

4.4 SUMMARY

A liquid rocket propulsion system can be categorized according to its engine cycle, that is, the manner power is derived to feed propellants to the thrust chamber. A pressure feed system, although is of the simplest type, needs a high tank pressurization to drive the propellant downstream. A pump feed system, at the expense of simplicity however, utilizes a rotodynamic pump near the thrust chamber inlet to maintain the desired flow rate and injection pressure. With each feed system having its suite of benefits and drawbacks, our preference of one to another encompasses a compromise between some critical design parameters and some crucial performance metrics. And we fairly quickly deem the pressure feed system unsuitable for our application owing to our range of thrust magnitudes and thereby combustion chamber pressures.

We delve into the operational details of turbopump and electropump systems next, and work out the fundamental elements of the pump assembly. With regard to

the turbopump feed system, we define the engine cycle based on the source of the energetic drive fluid to power the turbopump assembly and the destination of the turbine exhaust fluid after doing the work. The three most common turbopump systems, viz. the gas generator cycle, the staged combustion cycle and the expander cycle, are outlined in the process. We realize that increasing the turbine working fluid flow rate increases the pump power output which translates into an increased combustion chamber propellant flow rate and an increased engine thrust magnitude. In an electropump feed system, the gas turbine assembly is swapped out for electric motors powered by battery packs that drive the propellant pumps instead. While the mass penalty from such a system had historically been an impediment, rocket engines employing electric-pump-fed cycles are at present feasible by dint of advancement in battery technologies and refinement in electric motors. And under the right set of circumstances, an electropump system can even outperform a turbopump system.

In our assessment of the practicality of each feed system type for our engine application, we settle on a combustion chamber pressure of $P_{cc} = 6000\text{kPa}$ and head rises of 9000kPa and 7500kPa for the oxidizer pump and the fuel pump respectively. Eventually, the overall mass and mass fractions of turbopump and electropump systems are evaluated for a multitude of component characteristics exclusive to the feed system, like those of gas generator or battery pack for instance. We observe that our electropump feed system does indeed outperform the turbopump feed system for our requirements of engine operation.

5

DESIGN OF THE THRUST CHAMBER

The design of a thrust chamber assembly presents among the most elaborate tasks in the realization of a liquid rocket propulsion system. Intertwined with the overall development of a number of rocket subsystems and subassemblies, such a procedure necessitates numerous iterations and optimizations in order to accomplish adequate performance parameters. In addition to performance, it entails a multitude of rationalizations behind the selection of engine components and component arrangements that help satisfy stringent mission objectives with minimum life cycle cost.

Yet, any design, unless verified experimentally, is at best considered preliminary—primarily because the myriad physical, chemical and thermodynamical processes of combustion within a thrust chamber are impossible to model exactly, making any analytical approach imperfect, and in turn making any designed specification approximate [13] [12]. Regardless, the defining criteria in the preliminary design of a rocket engine stem from the performance metrics of the propulsion system, which in turn derive from the objectives of the mission.

5.1 DESIGN REQUIREMENTS

Our hypothetical mission, as specified earlier, requires us to deliver a light payload of nearly 200 kg into LEO using a two-stage rocket. With the delta-v budget from the launch vehicle being 9500 m/s, we decide to target for a generated thrust of approximately 30 kN from each thrust chamber. Additionally, the outer diameter of our launch vehicle is capped at 1.25 m, which but constrains the size and/or number of thrust chamber(s) per stage. Moreover, the delta-v for the first stage is

presumed to be about 4500 m/s, whereas that for the second stage is presumed to be around 5000 m/s.

We, therefore, are required to design two thrust chamber versions—a sea-level variant for the booster stage and a vacuum-optimized variant for the upper stage. Both propulsion systems are obligated to be as similar as pragmatically possible, allowing only for minimal modifications to accommodate the disparate pressure conditions of sea level and vacuum.

The second stage, consequently, requires an engine with a high expansion-area-ratio nozzle. And the first stage, in order to generate the necessary thrust for liftoff and ascent, requires a cluster of thrust chambers in a parallel burn arrangement. In addition, to meet the total impulse requirements of the stage, and following a typical flight profile, the booster stage engines are required to nominally operate for a duration of up to 180 s.

Furthermore, a high thrust-to-weight ratio and a high specific impulse, being highly desirable characteristics of a propulsion system, are what we aspire to obtain. With all the initial conditions laid out, we now can work out the parameters for designing both our thrust chambers.

5.2 DESIGN PARAMETERS

It has heretofore been settled on that our propulsion system runs on the liquid oxygen/liquid methane combination at a mass mixture ratio of $O/F = 2.75$ and operates at a combustion chamber pressure of $P_{cc} = 6000 \text{ kPa}$ ($= 60 \text{ bar}$). Now, we need to determine the thrust chamber operating parameters such as combustion chamber temperature, effective molecular mass, and specific heat ratio. Prior to doing so however, we ascertain the expansion area ratios of both the nozzles.

5.2.1 Expansion Area Ratios

The ideal values of thrust chamber performance for a given ambient pressure are obtained under the conditions of optimum expansion. With ambient pressure varying substantially during the ascent of launch vehicles, trajectory computations typically determine the optimum exit pressure for booster-stage engines. And because ambient pressure is rather low at high altitudes, upper-stage engines employ nozzles with high expansion area ratios so as to achieve close to optimum expansion.

While the expansion ratio ought to approach infinity in order to satisfy ideal expansion at zero or near zero ambient pressure, the maximum theoretical exhaust velocity remains but finite (since it corresponds to an exhaust fluid with finite energy content) [12]. Besides, an increase in expansion area ratio in vacuum, even though increases performance, yields diminishing returns in terms of payload due to an increased engine size and thus an increased stage mass [13]. An optimization between engine performance and payload capacity, therefore, dictates the optimum expansion area ratio of a nozzle.

Standard values of expansion area ratio are between 3 and 30 for nozzles operating from sea level and between 40 and 400 for those optimized for vacuum operation [12] [13]—in practice, however, the opted ratios tend to be towards the lower margin of their respective ranges. Thrust chamber parameters exclusive to the first/booster stage and the second/upper stage are hereinafter designated with the subscripts $1ST$ and $2ND$ respectively.

After some scrutiny into propulsion systems of comparable performance, we settle on nozzle expansion area ratios of $\epsilon_{1ST} = 15$ and $\epsilon_{2ND} = 100$ for the sea-level engine and the vacuum-optimized engine. And from CEA [39], we figure out that the chosen expansion area ratios result in nozzle exit pressures of $P_{e.1ST} = 39.878$ kPa and $P_{e.2ND} = 3.058$ kPa for the respective engine variants. We, therefore, obtain pressure ratios of $(P_{cc}/P_e)_{1ST} = 150.459$ and $(P_{cc}/P_e)_{2ND} = 1962.067$ across the respective nozzle variants.

Because performance is negatively affected by ambient pressure, we consider the maximum ambient pressure in all our performance calculations. The maximum external pressure for the booster-stage nozzle equals $P_{ext.1ST} = 101325.0$ Pa (at sea level). For a typical flight profile, wherein stage separation occurs at about 75 km and engine ignition commences at around 80 km, the maximum external pressure for the upper-stage nozzle equals $P_{ext.2ND} = 0.886280$ Pa (at an altitude of 80 km) [52]. All thrust chamber parameters obtained above are tabulated below.

	1ST STAGE	2ND STAGE	
Expansion area ratio ϵ	15	100	
Exit pressure P_e	39878.0	3058.0	Pa
Pressure ratio P_{cc}/P_e	150.458900	1962.066710	
External pressure P_{ext}	101325.0	0.886280	Pa

Furthermore, the dimensions of a thrust chamber—of vacuum-optimized thrust chambers in particular—are often constrained by the outer diameter as well as the interstage length of a launch vehicle. With the diameter of our vehicle being 1250 mm, it is but prudent to restrict the maximum diameter of the upper-stage nozzle to 750 mm so as to accommodate any support structure and/or additional component within the rocket interstage. We preliminarily select an exit diameter of 600 mm for the aforesaid nozzle, thereby leaving us a margin of some 300 mm radially between the thrust chamber and the interstage fairing.

Now, from the exit diameter of $D_{e,2ND} = 600.0$ mm and the expansion ratio of $\epsilon_{2ND} = 100$, we obtain a throat diameter of $D_{t,2ND} = 60.0$ mm for the second-stage engine variant. Because the throats of the upper-stage nozzle and the booster-stage nozzle are dimensionally identical, the expansion ratio of $\epsilon_{1ST} = 15$ gives us an exit diameter of $D_{e,1ST} = 232.379$ mm for the first-stage engine variant.

With major external parameters now preliminarily ascertained, we next proceed with determining all thrust chamber performance parameters, and later move on to scrutinizing and optimizing the obtained values.

5.2.2 Performance Parameters

Without delving deep into solving the chemical/thermodynamical quantities of combustion, we run CEA [39] to figure out the following crucial parameters: combustion chamber temperature T_{cc} , effective molecular mass \mathfrak{M} , and specific heat ratio k .

Combustion chamber temperature T_{cc}	3338.670	K
Effective molecular mass \mathfrak{M}	19.503	g/mol
Specific heat ratio k	1.207	

Because these metrics form the basis of all subsequent calculations, we run RPA [41] and corroborate the accuracy of the values; in addition, combustion charts computed in [43] and presented in figure 5.1 only help validate our values.

From the obtained values, and using equations from chapter 2, we compute the following performance parameters for the first-stage thrust chamber variant: gas constant R , characteristic velocity c^* , thrust coefficient C_f , and effective exhaust velocity c .

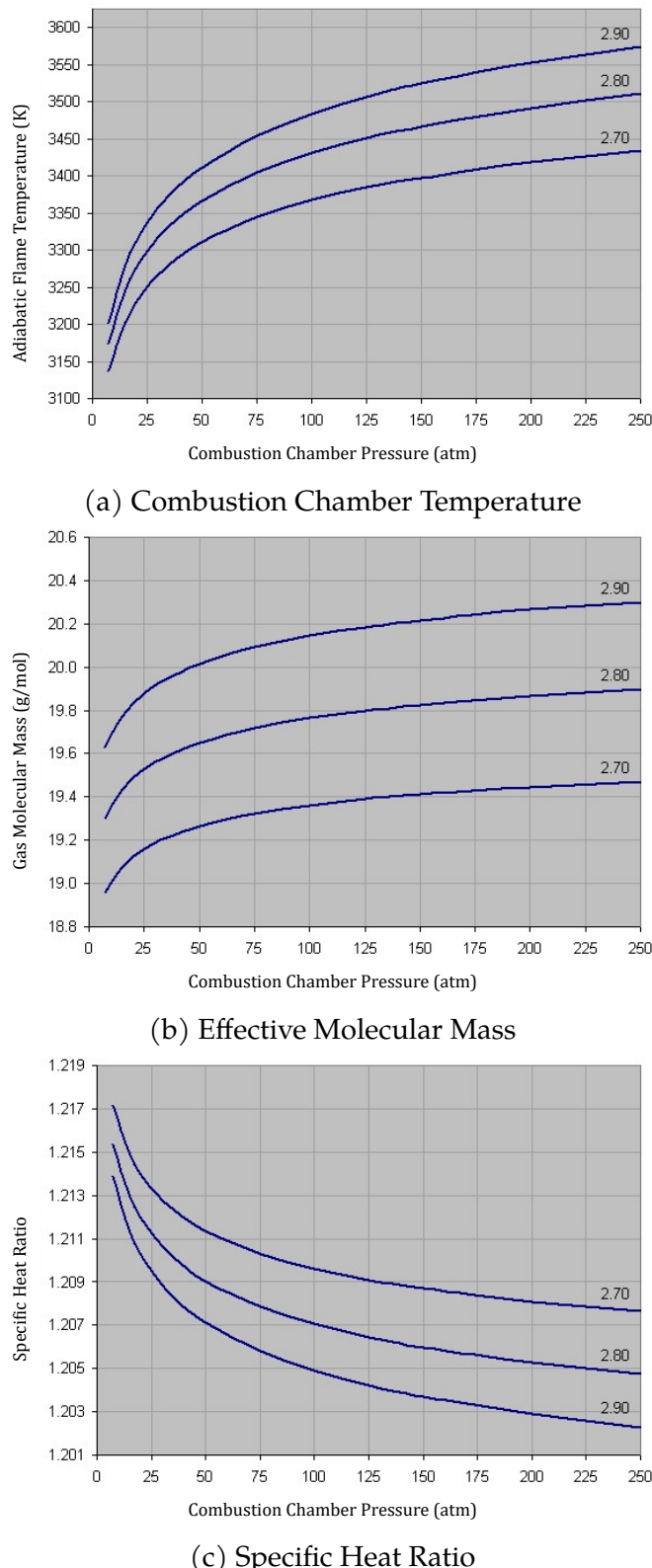


Figure 5.1.: Variation of the three crucial combustion parameters with chamber pressure. [43]

1ST STAGE		
Gas constant R	426.317111	J/K/kg
Characteristic velocity c^*	1835.757507	m/s
Thrust coefficient C_f	1.531862	
Effective exhaust velocity c	2812.128075	m/s

Now, propellant mass flow rate for the first-stage thrust chamber calculated in terms of combustion chamber pressure, characteristic velocity and throat area (using equation 2.14) equals $\dot{m}_{1st} = 9.241199$ kg/s. However, the mass flow rate when calculated as minimum rated thrust (at sea level) divided by effective exhaust velocity equals $\dot{m}_{1st} = 10.668077$ kg/s. The significant mismatch in flow rate persists for the second-stage thrust chamber, which but confirms that our initial assumptions of nozzle dimensions are incorrect. Therefore, we redetermine the nozzle throat diameter to be $D_t = 65.0$ mm, which yields a nozzle throat area of $A_t = 0.003318307240$ m². The corrected throat dimension results in propellant mass flow rate variations of less than 2% (and is essential to account for design uncertainties and correction factors). The thrust chamber dimensions determined thus far are tabulated here.

	1ST STAGE	2ND STAGE	
Throat diameter D_t	65.0	65.0	mm
Exit diameter D_e	251.744	650.0	mm
Exit area A_e	0.049775	0.331831	m ²

The ideal values of mass flow rate \dot{m} , specific impulse I_s , and thrust F for the first-stage thrust chamber variant are presented below.

1ST STAGE		
Mass flow rate \dot{m}	10.845574	kg/s
Specific impulse I_s	286.757259	s
Thrust F	30499.142443	N

5.2.3 Performance Correction Factors

Prior to proceeding with ascertaining the remaining thrust chamber parameters, we correct our ideal values of performance using, in the absence of any experimental data, rather reasonable correction factors. Because our assumption for flow characteristic across the nozzle involves frozen composition at the throat (which tends to underestimate performance typically by 1 to 4%), we presume relatively optimistic figures for all correction factors and yet expect to obtain theoretical performance somewhat close to actual numbers.

Characteristic velocity ζ_{c^*}	0.99
Thrust coefficient ζ_{C_f}	0.97
Mass flow rate $\zeta_{\dot{m}}$	1.01
Effective exhaust velocity ζ_c	0.960300
Thrust ζ_F	0.969903

The following corrected performance parameters are adopted hereinafter in the calculation of all additional thrust chamber metrics.

	1ST STAGE	2ND STAGE	
Characteristic velocity c^*	1817.399932	1817.399932	m/s
Thrust coefficient C_f	1.485907	1.885631	
Effective exhaust velocity c	2700.486590	3426.945580	m/s
Mass flow rate \dot{m}	11.064676	11.064676	kg/s
Specific impulse I_s	275.372996	349.451197	s
Thrust F	28980.711195	36776.824036	N

5.3 DESIGN OF THE NOZZLE

With the primary performance metrics ascertained, we now look into the shape of the convergent-divergent nozzle. Because the flow of the combustion fluid is subsonic within the convergent nozzle section, fine details in the profile of the convergent section do not appreciably affect nozzle performance. On the

contrary, the contour of the divergent section is of profound significance to nozzle performance owing to the supersonic velocities of the exhaust jet contained within.

There primarily exist two configurations of supersonic nozzles: conical-shaped nozzles and bell-shaped nozzles. While a conical nozzle entails little design complexity and allows ease of manufacture, it undergoes an appreciable performance loss due to the nonaxial component of the exhaust gas velocity. A bell nozzle, on the other hand, provides an efficient expansion of the supersonic exhaust gas flow with a shorter and lighter divergent section, albeit at the expense of a complex contour design. A few geometries for the divergent nozzle section have been analysed below.

5.3.1 Ideal Nozzle

The flow within a convergent-divergent nozzle—which is considered compressible, isentropic, irrotational, inviscid, steady and uniform—may again be assumed quasi-one-dimensional. Even though the flow intrinsically is three-dimensional, variations in the flow variables are far more pronounced in the axial (x) direction than in the radial (y and z) direction due to the varying cross-sectional area of the nozzle along its axis [53]; the flow variations along y and z are neglected and the fluid properties are considered as functions of x only. Although merely an approximation to the actual flow, the quasi-one-dimensional analysis approach can help determine flow properties within a rocket nozzle to a fair degree of accuracy. The theory of the method of characteristics is further applied in analysing the flow processes and designing the divergent section of a supersonic nozzle.

For a supersonic flow in a two-dimensional space, the flow variables are continuous and the governing partial differential equations are hyperbolic. Now, there exist unique curves in the x - y space, called *characteristic* curves, on which derivatives of the flow variables are indeterminate and may as well be discontinuous [54]; such curves transform the nonlinear partial differential equations into integrable ordinary differential equations and, as a result, generate the compatibility equations with exact solutions that remain constant along the characteristics [54]. Besides, because it relies on developing a network of curves in the 2-D space, application of the method of characteristics is inherently a graphical technique. Figure 5.2 illustrates the existence of two characteristics through a point A . Since exploring the entire mathematical theory of hyperbolic equations is beyond the scope of this study, only the essential elements of the method of characteristics have been summarized below.

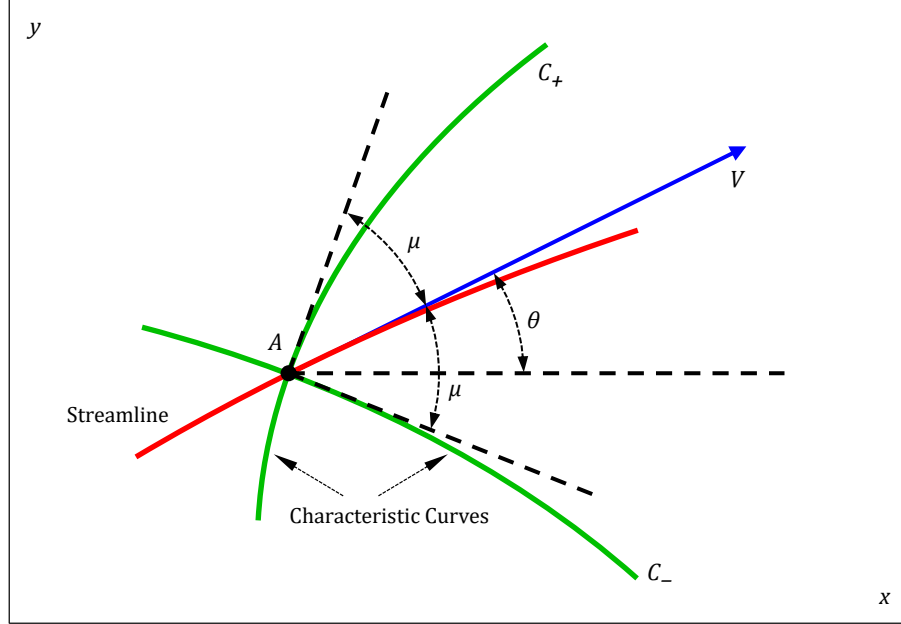


Figure 5.2.: Definition sketch of the velocity field and the local characteristic curves for a point in a supersonic flow.

The velocity potential equation of a streamline defined by a velocity field \vec{V} through Cartesian coordinates can be expressed as

$$\left(1 - \frac{u^2}{a^2}\right) \frac{\partial^2 \phi}{\partial x^2} + \left(1 - \frac{v^2}{a^2}\right) \frac{\partial^2 \phi}{\partial y^2} - \frac{2uv}{a^2} \frac{\partial^2 \phi}{\partial x \partial y} = 0 \quad (5.1)$$

where, ϕ is the velocity potential, a is the local speed of sound, and u and v are the velocity components along x and y for the point A on the streamline.

Because the velocity potential and its derivatives are functions of x and y , the differential relations are given as follows

$$d\left(\frac{\partial \phi}{\partial x}\right) = du = \frac{\partial^2 \phi}{\partial x^2} dx + \frac{\partial^2 \phi}{\partial x \partial y} dy \quad (5.2a)$$

$$d\left(\frac{\partial \phi}{\partial y}\right) = dv = \frac{\partial^2 \phi}{\partial x \partial y} dx + \frac{\partial^2 \phi}{\partial y^2} dy \quad (5.2b)$$

On examining the system of equations 5.1 and 5.2 and solving for the ensuing second order derivatives as described by Anderson in [53], it becomes apparent that there are values of dx and dy for which the velocity derivative $\partial^2 \phi / (\partial x \partial y)$ becomes undefined. This characterizes the presence of specific directions through the point A which satisfy the condition for indeterminacy of the characteristic lines.

The precise direction of the characteristic can, therefore, be formulated as

$$\left(\frac{dy}{dx}\right)_{char} = \frac{-\frac{uv}{a^2} \pm \sqrt{\left(\frac{u^2+v^2}{a^2}\right) - 1}}{1 - \frac{u^2}{a^2}} \quad (5.3)$$

where, $u = V \cos \theta$, $v = V \sin \theta$, and (dy/dx) denotes the slope of the characteristic.

Using the Mach angle μ , the expression for the slope can subsequently [53] be obtained as

$$\left(\frac{dy}{dx}\right)_{char} = \tan(\theta \mp \mu) \quad (5.4)$$

The result signifies that two characteristic curves run through the point A : one with a slope of $\tan(\theta - \mu)$ and labelled as C_- (inclined *below* the streamline), and the other with a slope of $\tan(\theta + \mu)$ and labelled as C_+ (inclined *above* the streamline).

After substantial mathematical manipulation of the system of above equations as described in [53], the compatibility equations along the characteristic lines can be expressed in terms of the Prandtl–Meyer function ν as follows

$$\theta + \nu = K_- = \text{constant} \quad [\text{along } C_- \text{ characteristic}] \quad (5.5a)$$

$$\theta - \nu = K_+ = \text{constant} \quad [\text{along } C_+ \text{ characteristic}] \quad (5.5b)$$

In essence, the characteristic lines symbolize the Mach lines through a point in a supersonic flow [53]. Accordingly, an *expansion fan* is formed whenever the flow encounters a convex corner and is turned away from itself. And correspondingly, an *oblique shock* is formed whenever the flow encounters a concave corner and is turned into itself. Thus, the function of these waves is to gradually change the local flow direction within the divergent section so as to achieve an axial wave-free flow with an exit Mach number M_e . Although an infinite number of Mach waves crisscross the flow field, only a finite number of characteristic curves are deemed adequate for determining the divergent section contour [54].

Application of the method of characteristics is depicted schematically in figure 5.3. While the sketch here is rather coarse, the characteristic network used in practice is developed significantly finer in an effort to generate an optimum profile for a supersonic nozzle. The profile of the expanding section, as [53] states, is somewhat arbitrary and is typically a circular arc of a large radius. Of paramount importance, however, is the contour of the straightening section since it serves to cancel the expansion waves produced within the expanding section. Taking advantage of

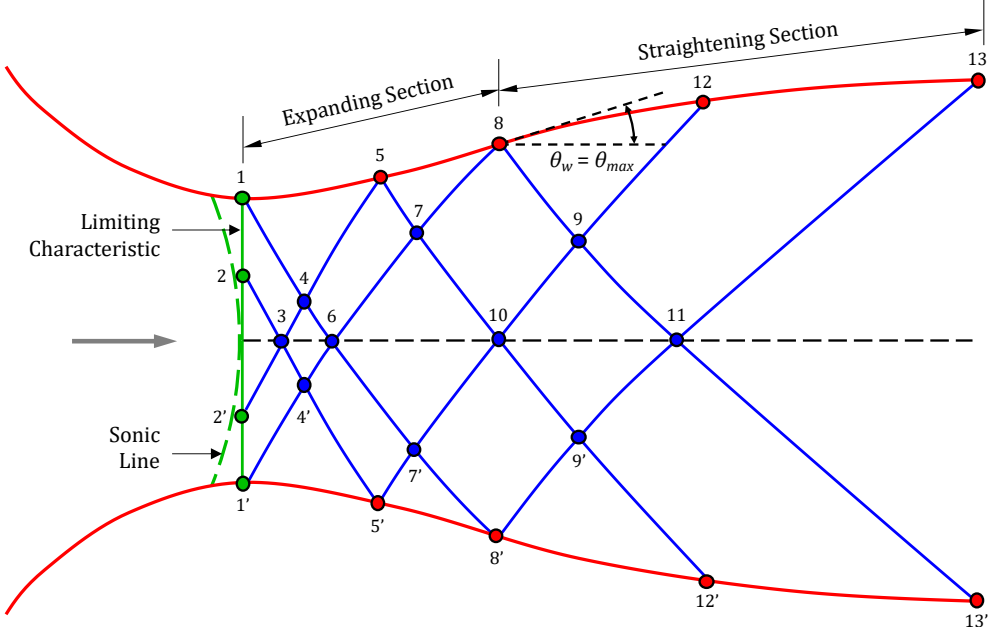


Figure 5.3.: Design schematic of a supersonic nozzle contour from a network of crisscrossing characteristics and intersecting grid points.

flow symmetry with respect to the nozzle axis, only the upper half of the divergent section is commonly analysed, wherein the centerline is treated as a solid wall and the characteristics emanating through it are treated as reflections of the upper centered expansion waves.

Mapping of the supersonic flow field, therefore, begins at internal and/or wall grid points on an initial data line of known properties (usually at the throat) and propagates downstream along characteristic directions C_+ and C_- . This establishes local flow angle θ and local Prandtl–Meyer angle ν from respective compatibility constants K_+ and K_- , and in turn obtains the local Mach number M . Additional flow parameters (like pressure P , temperature T and specific volume V) at each grid point within the flow field can subsequently be computed using the relations for isentropic condition and frozen composition [12]. The methods outlined above, along with any steps in between as discussed in [54], can be implemented in a computer program to design a proper divergent section contour for our thrust chamber.

We use MATLAB to generate an ideal ‘minimum length nozzle’ contour for a uniform inlet flow at the throat. Employing 100 characteristic lines for our analysis, we obtain expansion area ratios of $\epsilon_{1ST} = 14.016$ and $\epsilon_{2ND} = 108.229$ from exit Mach numbers of $M_{e,1ST} = 3.724$ and $M_{e,2ND} = 5.952$ for both our thrust chamber variants respectively. Results of the computation are plotted in figure 5.4, where

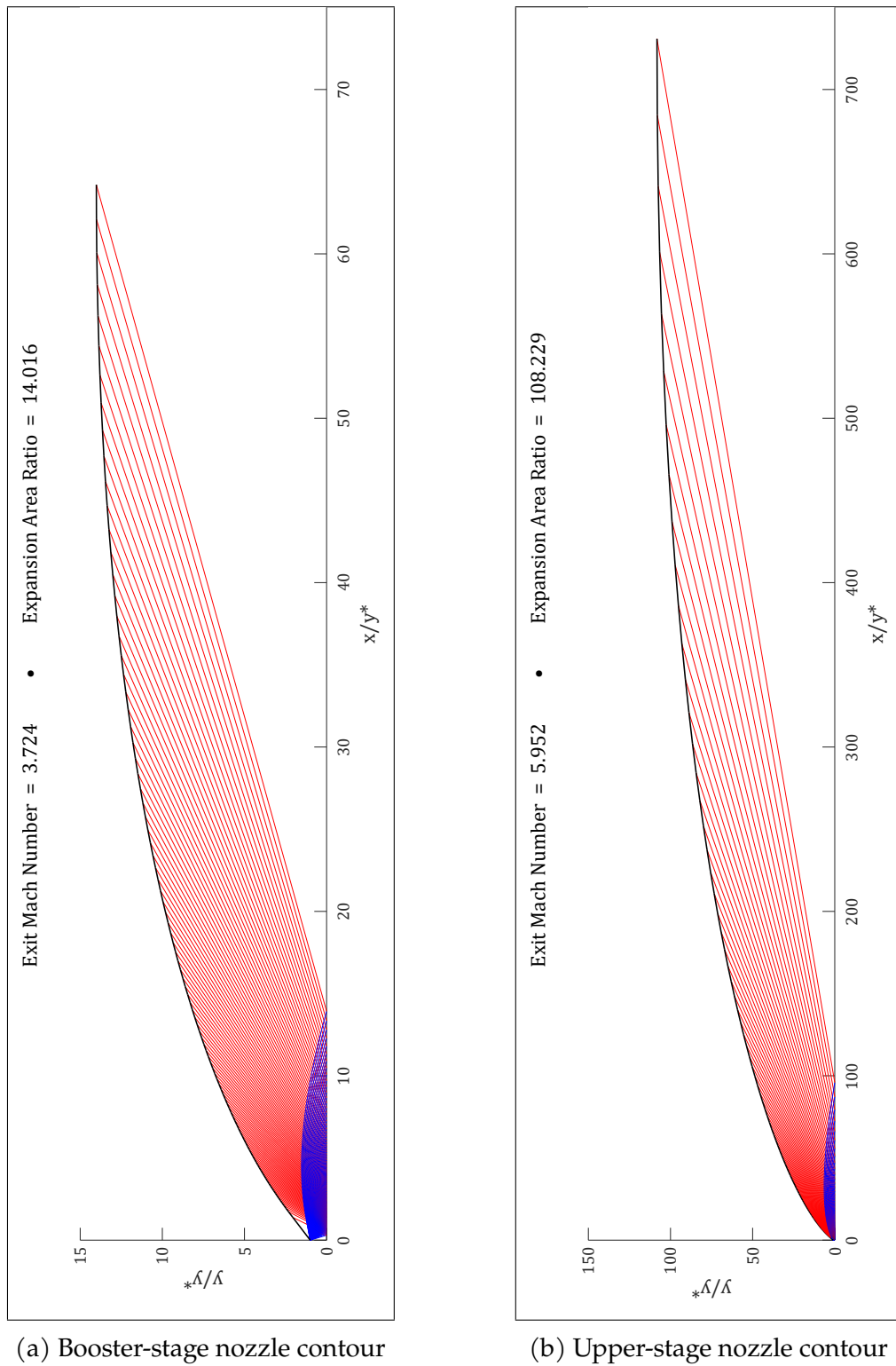


Figure 5.4.: The ‘minimum length nozzle’ contours for our thrust chamber variants computed using the method of characteristics. The scale of the plot 5.4a is one-tenth that of the plot 5.4b above.

the x - y plane represents the ratio of corresponding nozzle dimension to throat dimension for a 2-D nozzle. Contour coordinates of the exit wall point, therefore, are at (64.210, 14.016) and (730.838, 108.229) for nozzles of the booster stage and the upper stage respectively, with the throat wall point being at (0.0, 1.0) for each nozzle. Moreover, the obtained area ratios are within 0.166% and 0.297% of their respective theoretical values for both the nozzle configurations. This signifies that the degree of accuracy of our graphical solutions, even when computed with only 100 characteristic lines, is remarkable.

Yet, an ideal contour design for our divergent sections is anything but practicable. Coordinates of the exit wall points above imply that our nozzles are disproportionately long for rocket applications. Besides, the supersonic flows accomplish the exit Mach numbers along the centerline only at 21.672% and 13.110% of their respective nozzle lengths. Furthermore, any adverse effects of chemical kinetics are mitigated by employing a circular arc instead of a sharp corner at the throat, which only lengthens the nozzle some more [55]. Such a long divergent contour, although produces a one-dimensional exhaust profile thereby maximising the geometric efficiency, also raises viscous drag, inert mass and heat flux of the nozzle thus reducing its overall efficiency. The factors above validate that an ideal contour design does little good to our engine configurations and warrant the need for a more optimum nozzle contour.

5.3.2 Truncated Ideal Contoured (TIC) Nozzle

Although an ideal nozzle is necessary to produce an axial uniform exit flow condition, any thrust generated towards the end of the straightening section is negligible owing to the small divergence angles near the exit. It is, therefore, prudent to truncate the nozzle to attain a more feasible contour design; the contour thus obtained is called a truncated ideal contour (TIC). A graphical technique for selecting the optimum contour from a family of TIC nozzles is presented in [56]. A complete set of ideal contours along with lines representing constant length, vacuum thrust coefficient, surface area and exit diameter is initially synthesised in a plot. An optimisation process is finally implemented to determine where the contour has to be truncated so as to maximise performance for a given constraint such as nozzle length or exit diameter. Figure 5.5 illustrates an enlarged section of such a plot to help visualize the optimisation procedure. Point *A*, which is where the thrust coefficient line is tangent to a line of constant radius, is the optima representing the nozzle exit point that yields the maximum thrust for a given expansion ratio. Point *B*, which is where the thrust coefficient line is tangent to the constant surface

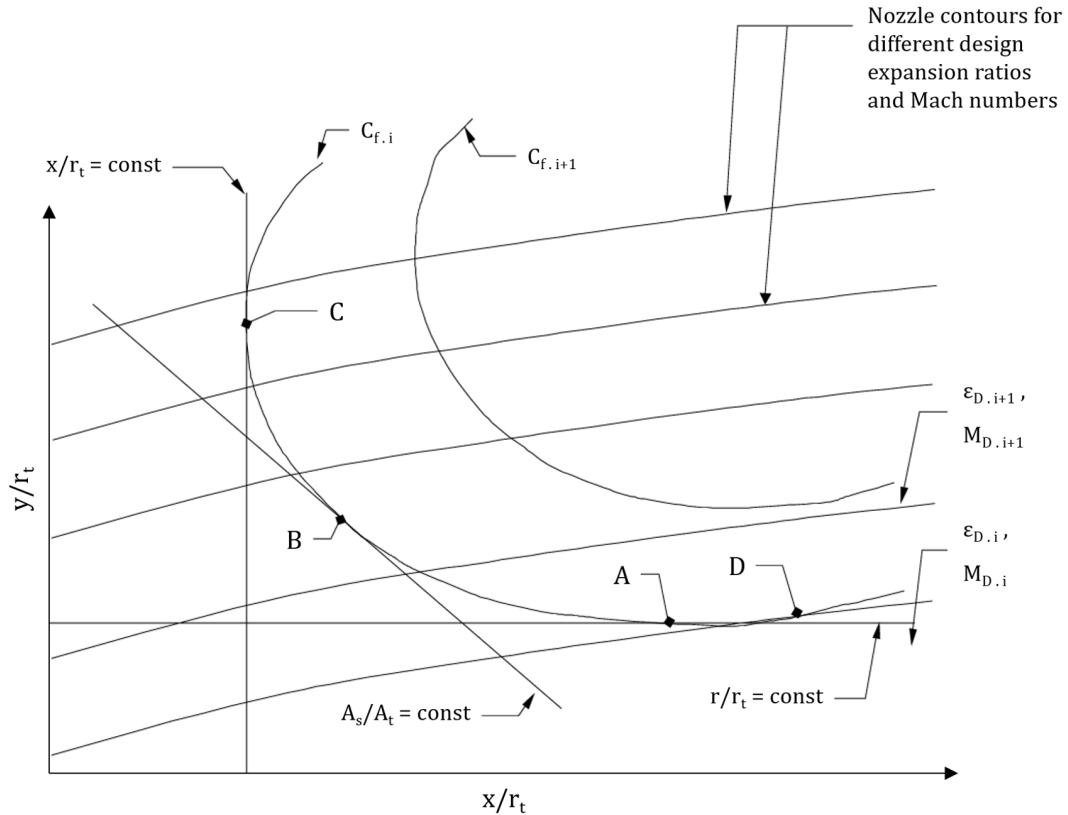


Figure 5.5.: Illustration of an optimum TIC nozzle for given constraints. [55]

area line, represents the optima of a nozzle contour for a given surface area. Point C represents the contour of a nozzle with the maximum performance for a given length. Point D represents the exit point at which the maximum thrust is attained from any given nozzle contour. Among these, the TIC nozzle represented by point A is of the most practical interest.

Gogish in [57] presents a method to further shorten the nozzle length, the basis of which is to linearly compress a TIC nozzle in the axial direction to produce a compressed truncated ideal contour (CTIC). Any discontinuity in the CTIC nozzle wall slope produced as a result is eliminated by a cubic equation which smoothly connects the linearly compressed curve with the initial circular curve. The above compression yields a nozzle with a more rapid initial expansion followed by a more severe turn back, therefore resulting in the propagation of strong compression waves into the flow field. With a strong enough compression, the characteristic lines can coalesce to form a right-running oblique shock wave that increases the static pressure of the supersonic flow across it. When the shock wave lies near the nozzle wall, the increased local pressure along the wall helps marginally increase

the thrust. And under the right circumstances, a CTIC nozzle may even yield a higher performance than a Rao nozzle [55].

5.3.3 Thrust Optimised Contoured (TOC) Nozzle

The application of the calculus of variations provides a direct and elegant approach of designing the optimal nozzle contour. A complicated method formulated to produce a nozzle with a thrust optimised contour (TOC) for prescribed values of nozzle length was simplified significantly by Rao in [58] and was later adopted extensively for rocket propulsion applications; the TOC nozzle is hence commonly referred to as a Rao nozzle, and the procedure to design one is as follows.

A constant Mach number line TO is first generated at the throat using transonic flow analysis. With the solid boundary at TN and the flow condition along TO defined, a kernel flow field $TNKO$ is developed next using the method of characteristics for specified values of radius of curvature $R_{t,d}$ and angle of divergence $\theta_{t,d}$ downstream of the throat. Location of the exit wall point E is established now from the given design parameters of nozzle length and expansion area ratio. The characteristic line NK is determined next by concurrently satisfying the following conditions:

- A control surface PE is created between the exit point E and a select point P along the kernel line NK .
- The mass flow across PE equals the mass flow across NP .
- The thrust obtained from the nozzle is the maximum.

The contour NE is ultimately constructed by selecting points P' , P'' , etc. along the line NK that create a series of control surfaces $P'E'$, $P''E''$, etc. as described above

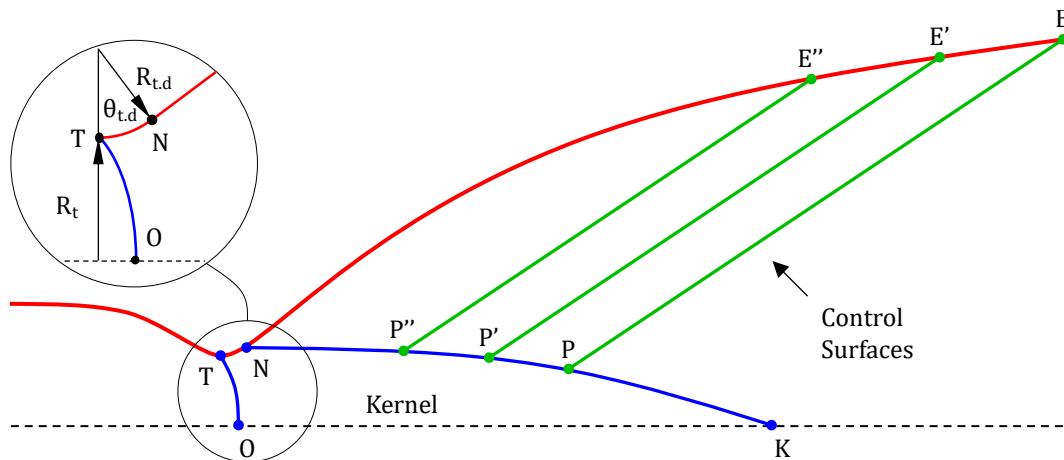


Figure 5.6.: Schematic of a thrust optimised contoured (TOC) nozzle.

which define points E' , E'' , etc. on the contour NE . The design procedure detailed above is illustrated in figure 5.6.

Compared to a TIC nozzle, a TOC nozzle features a greater initial expansion and, as a result, induces a more drastic turning of the flow [55]. The corresponding values of wall angle and Mach number are, consequently, higher immediately downstream of the throat and lower near the exit. The ensuing compression waves formed in the region NPE coalesce into a right-running shock downstream of the control surface PE and, in the process, keep the region shock free. By definition, a TIC nozzle is created when point P equals point K .

5.3.4 Thrust Optimised Parabolic (TOP) Nozzle

Because the computation necessary to construct a TOC nozzle is rather complex, Rao in [59] proposed a simple geometric approach to design a nozzle with a thrust optimised parabolic (TOP) contour. Also known as a parabolic bell nozzle, the profile of such a nozzle involves two circular arcs at the throat T and a parabolic curve from the inflection point I to the exit point E . Figure 5.7 portrays the design configuration of a TOP nozzle. The convergent contour immediately upstream of the throat is an arc having a radius of $R_{t,u} = 1.5 R_t$. And the divergent contour is composed of an arc with a radius of $R_{t,d} = 0.4 R_t$ immediately downstream of the throat followed by a parabola that can be defined with the following five variables: throat radius R_t , exit radius R_e , wall slope at the inflection point θ_i , wall slope at the exit point θ_e , and nozzle length from the throat plane to the exit plane L_n .

The bell nozzle length is typically specified as a fractional length of an equivalent standard conical nozzle with a 15° divergence half angle. The two parabolic contour

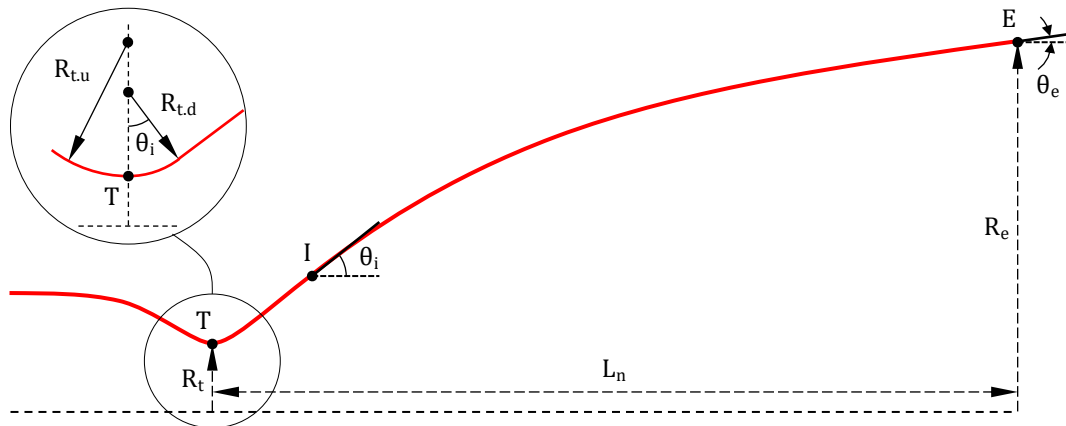


Figure 5.7.: Design schematic of a thrust optimised parabolic (TOP) nozzle.

angles θ_i and θ_e are functions of nozzle length fraction L_f and expansion area ratio ϵ , and can be determined from figure 5.8. With careful selection of the input parameters, a parabolic contour can accurately approximate an optimum contour generated using the method of characteristics. Yet, minor variations in the above variables incur only a minuscule loss in nozzle performance, making the design of a TOP nozzle somewhat forgiving.

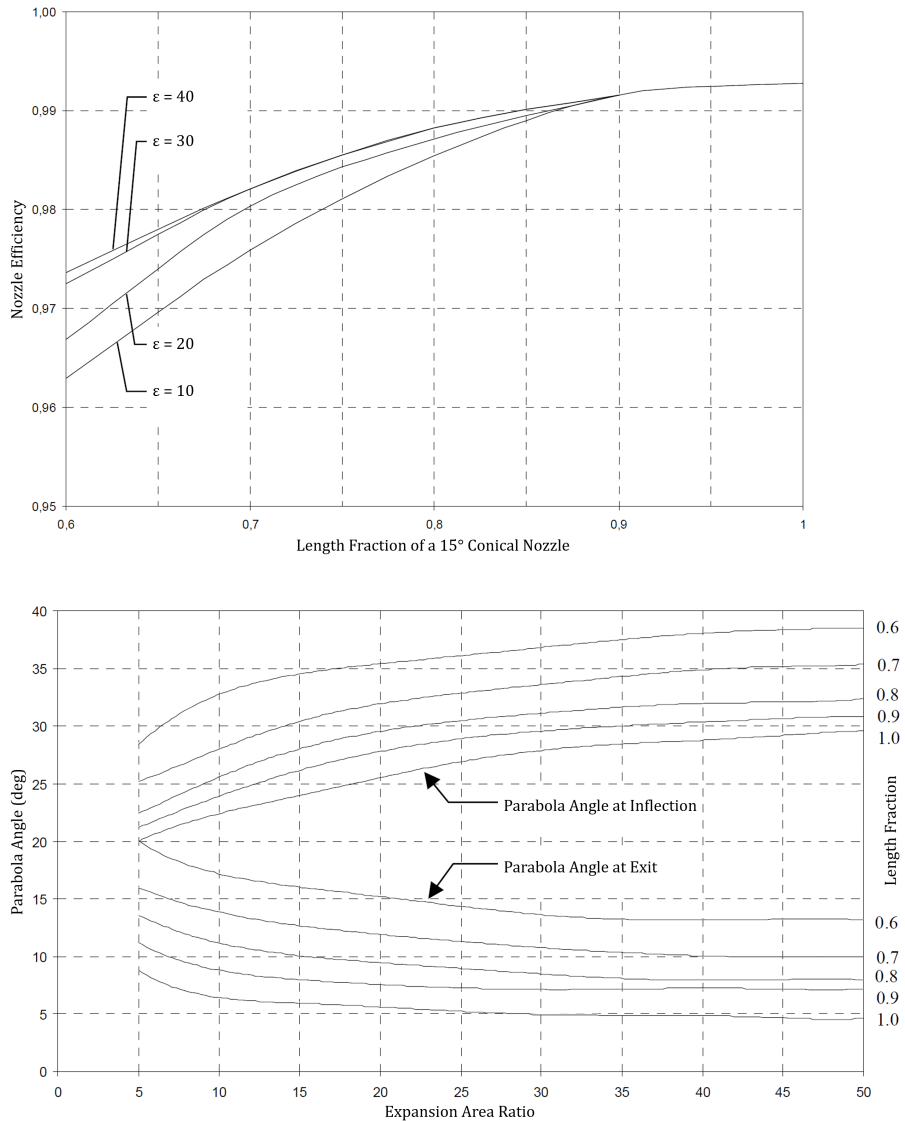


Figure 5.8.: The upper plot shows variation of geometric efficiency of a TOP nozzle with fractional length of a 15° conical nozzle. Optimal values for inflection θ_i and exit θ_e contour angles as functions of nozzle length fraction and expansion area ratio are shown with the lower set of curves. [55]

Now, strong compression waves are formed due to the discontinuity in the contour curvature at the point I where the circular arc transitions into the parabolic curve. These waves coalesce into a right-running oblique shock wave upstream of the last left-running characteristic line (unlike as in a TOC nozzle) and, in consequence, marginally raise the wall pressure at the nozzle exit. This additional margin in exit pressure can, to an extent, avert any adverse effects of flow separation in sea-level thrust chambers and, in turn, may even offset any loss in the performance of a TOP nozzle.

Having scrutinized the crucial characteristics of each nozzle configuration, we can avow that a TOP nozzle yields the most favourable contour—not only in terms of performance but also with regard to convenience—for a range of requirements and a variety of applications. Even when a single engine is required to operate throughout the disparate lower and upper atmospheric pressure conditions (such as the SSME), thrust chambers with parabolic bell nozzles have proven to be the most useful [12]. Moreover, the entire contour geometry can be ascertained from the mere determination of the above contour variables. These aspects only serve to underscore the advantages of the TOP contour over the others even in the absence of any empirical data.

We, therefore, employ the TOP nozzle for both our thrust chamber variants. And in doing so, we strive to as meticulously choose values for each contour variable as theoretically possible. Now, the dimensions of throat and exit for each nozzle variant have already been established. For the length of the nozzle, decent values range anywhere from 75% to 85% of an equivalent standard conical nozzle length [12], with 80% bell offering a good compromise between efficiency and penalty for both sea-level nozzles and vacuum-optimized nozzles [13]; this can not only be verified from the upper plot in figure 5.8 but may also be evidenced by the ubiquity of 80% bell nozzles across the rocket industry. From trigonometric analyses, we obtain lengths of $L_{n.1ST} = 278.775$ mm and $L_{n.2ND} = 873.300$ mm for the respective nozzle variants.

The two divergence angles of the parabolic segment can be established from the lower plot in figure 5.8. For our expansion ratios of interest, the inflection and exit angles for the sea-level nozzle are $\theta_{i.1ST} = 28.0^\circ$ and $\theta_{e.1ST} = 10.0^\circ$, while those for the vacuum-optimized nozzle are $\theta_{i.2ND} = 34.0^\circ$ and $\theta_{e.2ND} = 8.0^\circ$. As stated above, the convergent and divergent sections immediately upstream and downstream of the throat are, for each nozzle variant, circular arcs of 1.5 times and 0.4 times the respective radius of the throat. And for the convergent section, we rationally choose a nozzle convergence angle of $\theta_c = 30.0^\circ$ for each thrust chamber configuration.

With all nozzle variables now ascertained, we tabulate the pertinent data below and proceed with designing the combustion chamber.

	1ST STAGE	2ND STAGE	
Throat radius R_t	32.50	32.50	mm
Exit radius R_e	125.87	325.00	mm
Nozzle length L_n	278.78	873.30	mm
$= 0.8 \times$	348.468894	1091.624861	mm
Throat upstream radius $R_{t.u}$	48.75	48.75	mm
Throat downstream radius $R_{t.d}$	13.00	13.00	mm
Nozzle inflection angle θ_i	28.0°	34.0°	
Nozzle exit angle θ_e	10.0°	8.0°	
Nozzle convergence angle θ_c	30.0°	30.0°	

5.4 DESIGN OF THE COMBUSTION CHAMBER

The process of dimensioning a combustion chamber can—in the absence of any experimental data from prior successful engines of similar design configurations and operating conditions—be somewhat arbitrary. While chamber geometries can theoretically take any shape, actual design approaches tend to keep the combustor proportions neither too long and thin nor too short and fat but not of spherical proportions either [13]. Customarily, chambers feature a moderate longer-length smaller-diameter proportion so as to favour combustion stability and enhance combustion efficiency [13]. An optimum combustor volume, therefore, provides an adequate stay time for complete combustion while trying to minimize both inert mass and heat flux.

Because our chamber pressure is quite high, we can afford to adopt a marginally smaller combustor volume for our thrust chamber. With standard values anywhere between 0.56 m to 0.76 m for our propellant combination, we judiciously select a characteristic length of $L^* = 0.7$ m. And in order to restrict pressure losses, we examine contraction area ratios of similar engine designs [13] [12], and tentatively select a combustion chamber area of $A_{cc} = 4.0 A_t = 0.013273 \text{ m}^2$. These dimensions correspond to a stay time of $t_s = 0.885 \text{ ms}$, which corroborates well with

the experimental evaluations performed in [60]. Having computed all internal dimensions for both our thrust chamber variants, we tabulate the data and present configuration layouts and visual renders of both the variants.

Characteristic length L^*	0.7	m
Contraction area ratio ϵ_c	4.0	
Chamber diameter D_{cc}	130.00	mm
Chamber area A_{cc}	0.013273	m^2
Chamber volume V_{cc}	0.002323	m^3
Stay time t_s	0.885	ms
Cylindrical section length L_c	142.16	mm
Frustum section length L_f	56.29	mm
Combustion chamber length L_{cc}	198.45	mm

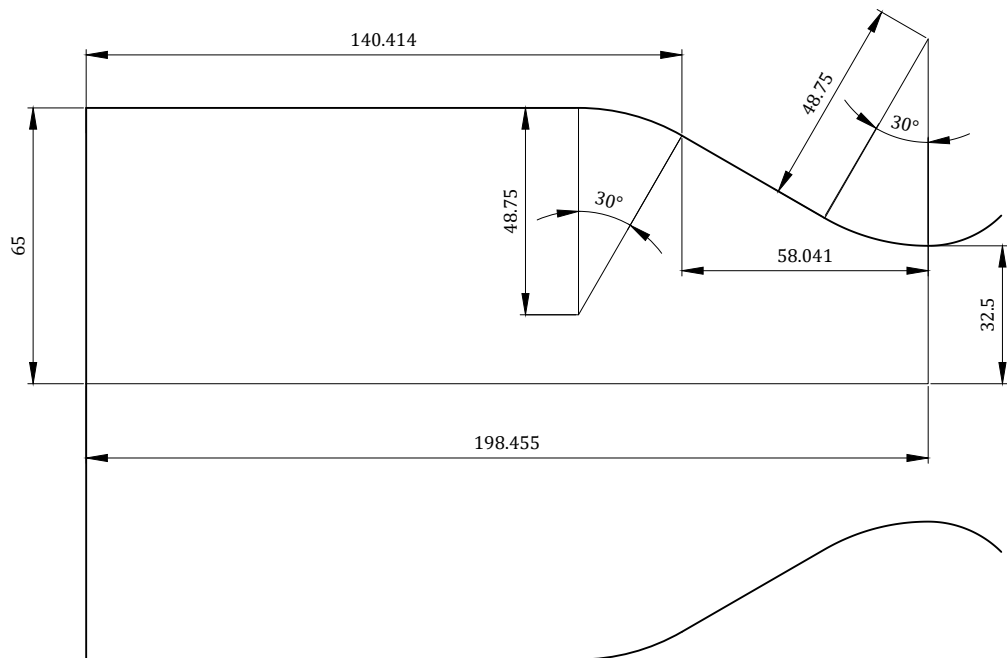


Figure 5.9.: Internal configuration layout of the combustion chamber. All dimensions are in mm.

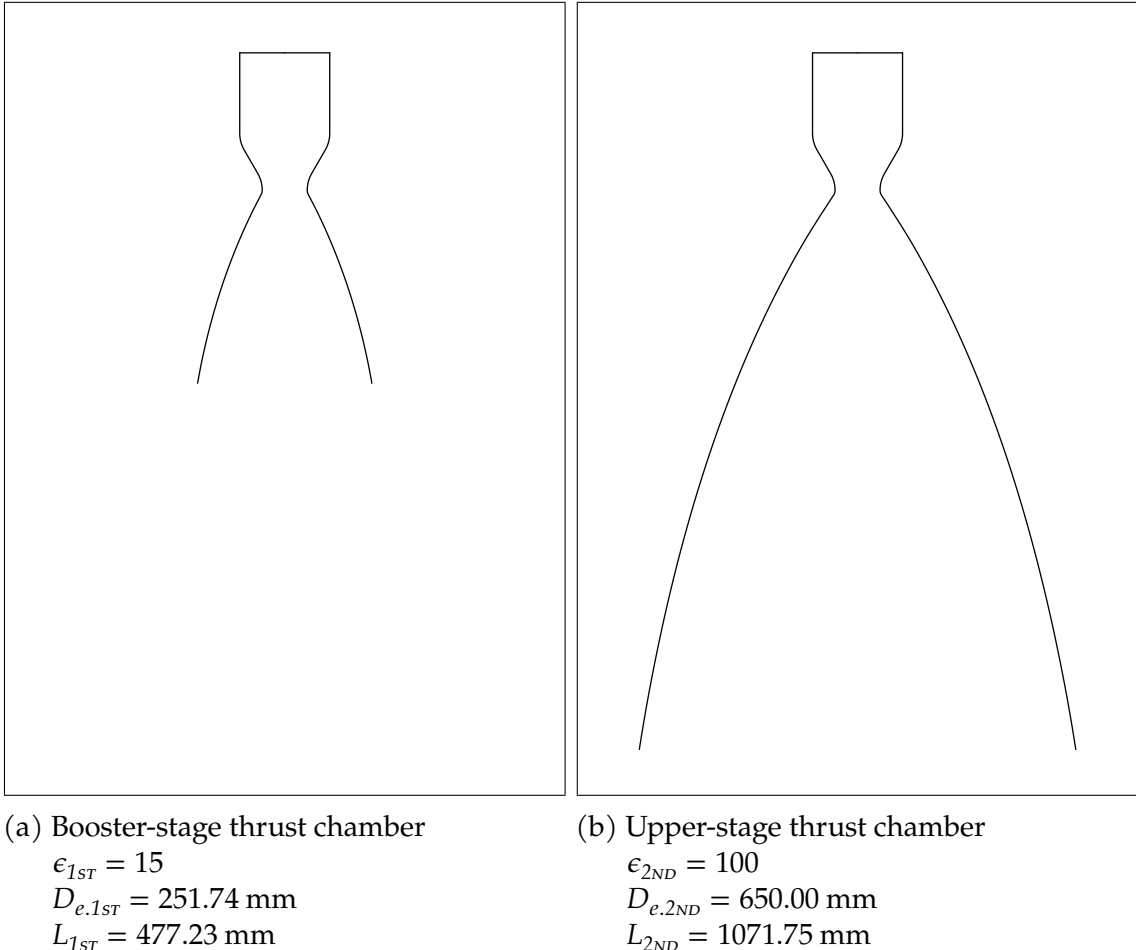


Figure 5.10.: Internal cross-sectional profiles for our thrust chamber variants. All dimensions are identical up to the throat, and the scale is equal for both the schematics.

5.5 SUMMARY

From the initial conditions outlined and the operational metrics ascertained, we incorporate methodologies to preliminarily design two thrust chamber versions for our rocket—a sea-level variant for the booster stage and a vacuum-optimized variant for the upper stage—with both propulsion systems obligated to be as similar as pragmatically possible. To do so, we determine the thrust chamber performance parameters such as expansion area ratio, combustion chamber temperature, effective molecular mass, and specific heat ratio. We settle on nozzle expansion area ratios of $\epsilon_{1ST} = 15$ and $\epsilon_{2ND} = 100$ for our thrust chamber variants, which lets us compute, using CEA, the other parameters listed. Because we have implemented procedures to underestimate performance typically by 1 to 4%, we account for our

theoretical performance values using relatively optimistic correction factors. Doing so ultimately helps us obtain rather realistic values of characteristic velocity, thrust coefficient, effective exhaust velocity, mass flow rate, specific impulse, and thrust for both the thrust chamber variants.

Further, we scrutinize the shape of the convergent-divergent nozzle, of the divergent section in particular. The expansion and shock characteristics of the supersonic exhaust jet are examined for an ideal nozzle using the method of characteristics, a truncated ideal contoured (TIC) nozzle, a thrust optimised contoured (TOC) nozzle, a thrust optimised parabolic (TOP) nozzle, as well as a conical nozzle. We subsequently adopt the TOP contour for our nozzle variants.

With the nozzle throat diameter of $D_t = 65.0$ mm, we next work out the exact dimensions of our nozzles. For the combustion chamber size, we adopt a marginally smaller combustor volume—with a characteristic length of $L^* = 0.7$ m and a contraction ratio of $A_{cc} = 4.0 A_t$ —albeit with an adequate propellant stay time for complete combustion. Detailed dimensions of both our thrust chamber variants are tabulated/presented in figures 5.9 and 5.10.

6

THRUST CHAMBER DESIGN SPECIFICS

For any engineering task, there are almost always more than one design approaches that could produce an excellent design outcome. This notion is especially true when the applications encompass thermal management and propellant injection of a liquid rocket propulsion system.

We have, over the previous chapters, designed the propellant feed system and the thrust chamber configurations for our twin-staged rocket. The topic of heat transfer together with material selection and the process of metering, injection, atomization, vaporization and mixing of propellants for their effective combustion are addressed in this chapter. And, of course, the design results unless validated through experimental investigations of engine hot-fire testing may only be regarded preliminary.

6.1 THERMAL MANAGEMENT

The high temperatures generated from the combustion fluid together with the high heat fluxes convected to the thrust chamber wall in consequence necessitate management of the high thermal energy within an engine to an adequate degree so as to obviate any failure during its operation. While there are sophisticated FEA tools to compute the distribution of thermal loads throughout the thrust chamber assembly, we analyse one-dimensional steady-state heat transfer rates only at the most critical wall sections, such as around key regions of the chamber, at and near the throat, and towards the exit of the nozzle. Further, we attempt to forestall any overheating through the adoption of appropriate cooling techniques as well as with the selection of suitable wall materials for the thrust chamber.

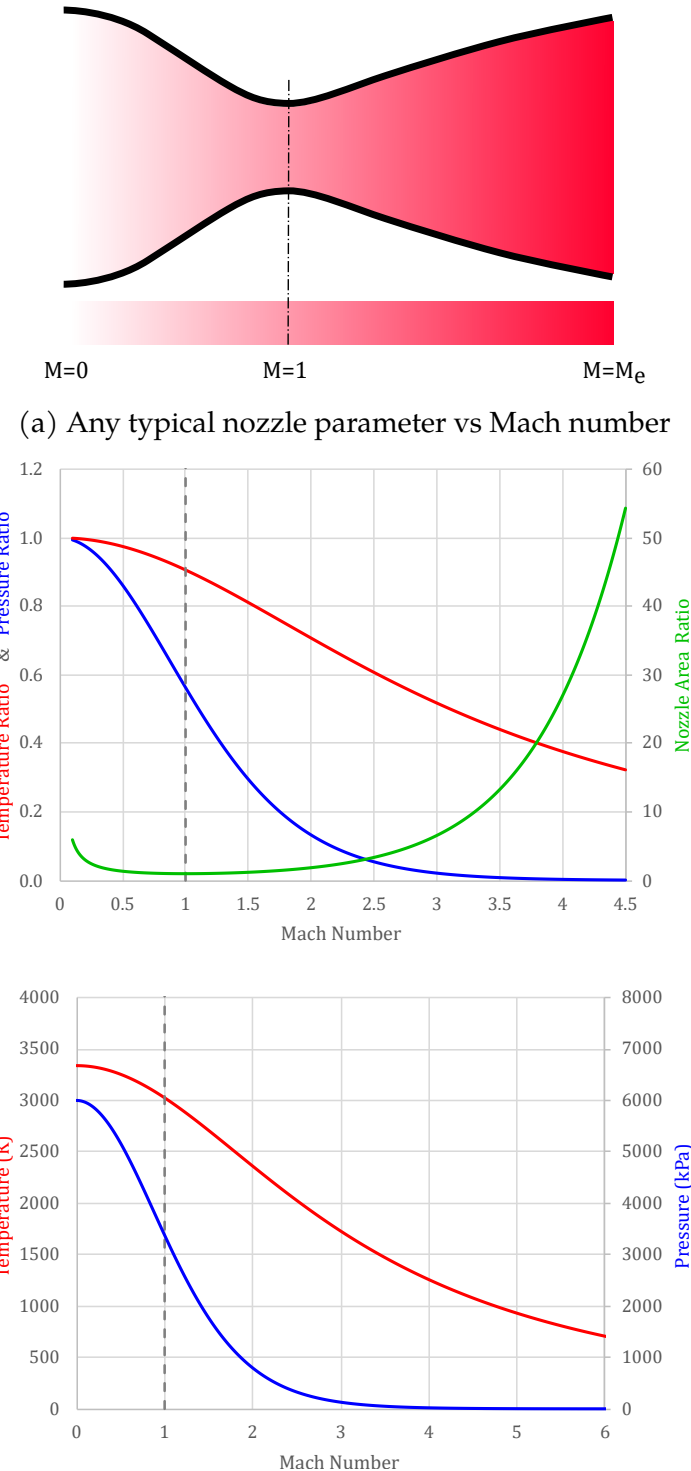


Figure 6.1.: Variation of nozzle area ratio, temperature (with its ratio) and pressure (with its ratio) with Mach number across the nozzle. The gradient in the topmost plot showcases variation of any typical nozzle parameter with Mach number—from stagnation to exit.

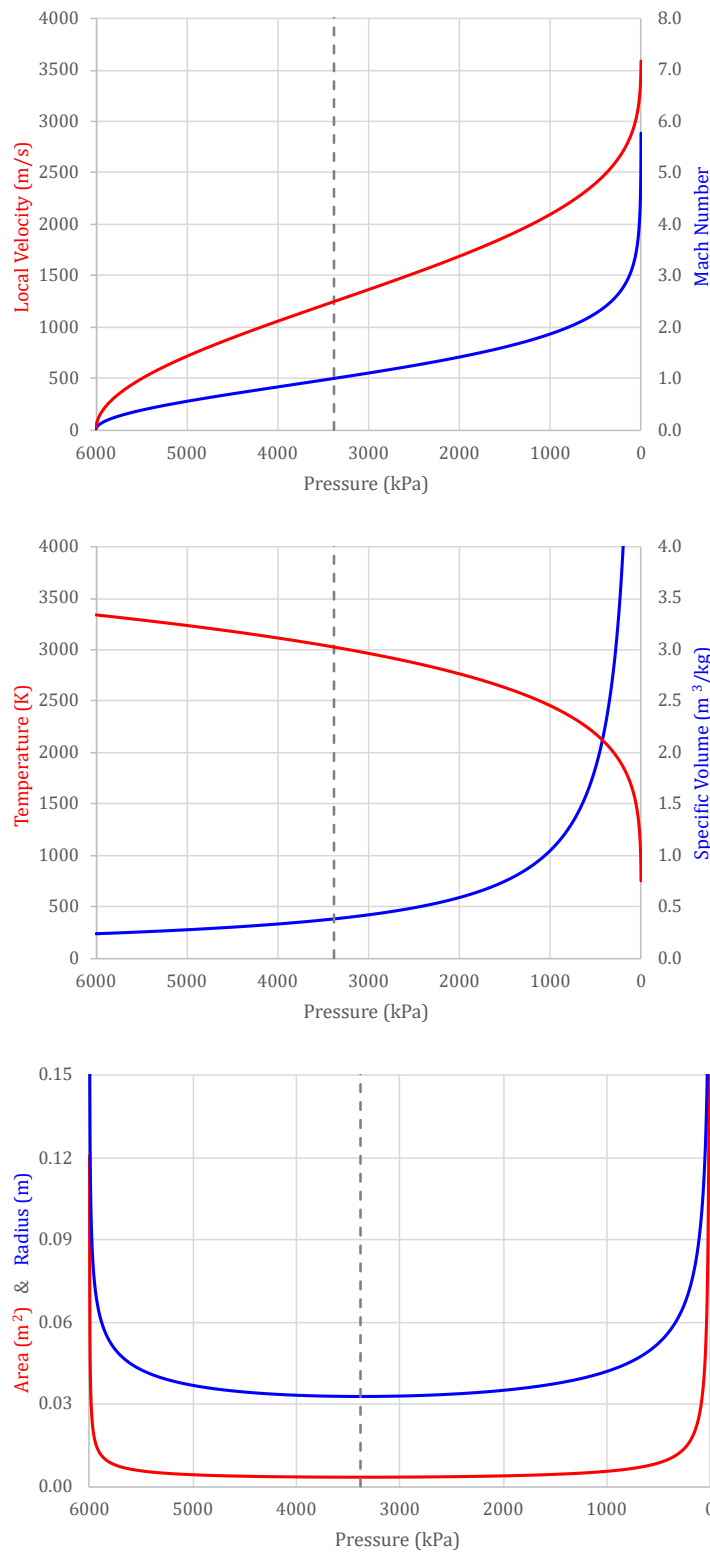


Figure 6.2.: Variation of Mach number, local velocity, temperature, specific volume, radius and area with pressure across the nozzle.

The exhaust gas temperatures at the above locations for both our thrust chamber configurations, as determined from CEA and using the equations for isentropic flow, are $T_{cc} = 3339$ K and $T_t = 3021$ K while $T_{e.1st} = 1190$ K and $T_{e.2nd} = 564$ K for nozzle expansion area ratios of 15 and 100 respectively. Because the temperatures up to a nozzle area ratio of approximately 10 are substantially high—as is evidenced from the plots in figures 6.1 and 6.2—for most conventional high-temperature materials to comfortably withstand, we need to regeneratively cool the thrust chamber at least down to this expansion area ratio. Beyond this area ratio, the free-stream gas temperatures and the wall heat fluxes are adequately low for us to radiatively cool the divergent nozzle section until the exit. For the sake of convenience, and keeping in line with design similarity, we decide to employ regenerative cooling throughout the booster-stage engine, and adopt radiative cooling after the area ratio of 15 for the upper-stage nozzle.

6.1.1 Booster-Stage Thrust Chamber

A suite of attractive physical properties such as high specific heat and high thermal conductivity make liquid methane a good coolant for rocket propulsion applications [33] [60]. In our regeneratively cooled thrust chamber, therefore, the entire fuel flow is circulated as the coolant fluid through the cooling jacket prior to its injection for combustion. Incidentally, whether the fuel is injected in a liquefied state or a supercritical phase depends on the net heat energy it absorbs from the walls [60]; this absorbed heat in being returned for combustion replenishes the thermal energy of the system that can be utilized to supplement engine performance [12].

With heat flux being the highest at the throat of a nozzle, the cooling channels at this region require the maximum coolant flow velocity and the minimum cumulative cross-sectional area compared to at any other location [12]. Heat transfer can be augmented by injecting fresh subcooled coolant into the jacket at or near the throat from where the flow usually turns both up towards the injector and down within the divergent section before returning up through adjacent channels near the exit. Any turbulence and/or surface roughness within the channels further improves heat transfer rates to the coolant.

In our thrust chamber, the main fuel feed is injected through the inlet manifold at the exit to flow unidirectionally upward within the longitudinal channels after which it enters directly into the injector manifold. And instead of a brazed tubular wall configuration, our engine employs a milled slot jacket design, where the smooth rectangular machined grooves are enclosed within and bonded to an outer structural shell using electrolytic plating techniques. Selection of the number of

milled slots, the channel dimensions and the wall thicknesses is dependent on the coolant pressure, its mass flow rate, its local flow velocity, as well as on the wall material [12].

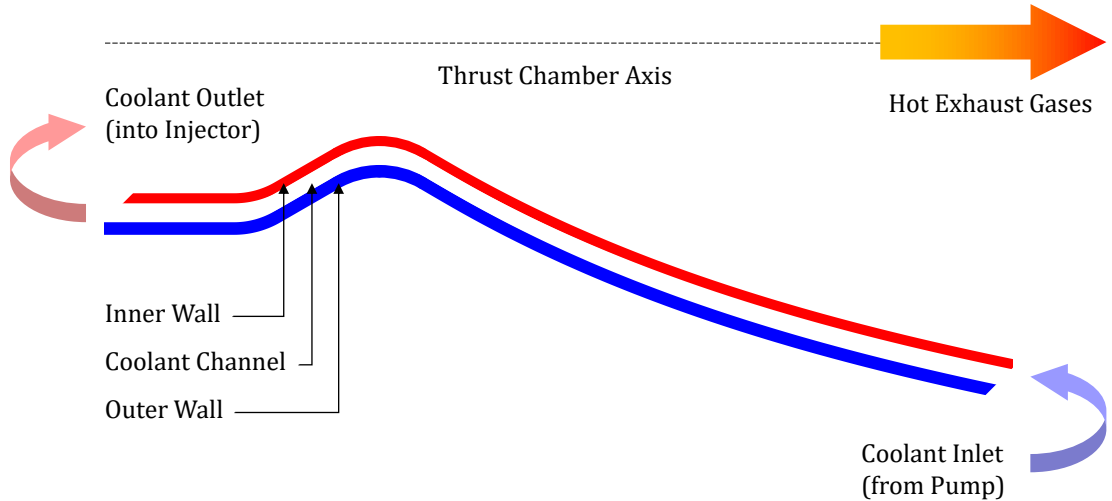


Figure 6.3.: Schematic diagram of the thrust chamber coolant channel.

We choose Inconel 625—a nickel-based superalloy with a chromium-molybdenum component—as the wall material for both the inner jacket as well as the outer shell. With its marvellous mechanical properties and fantastic thermal properties, Inconel 625 [51] finds prevalent usage in extreme environments of aerospace applications, like turbine blades and afterburner combustors inside jet engines. Besides, Inconel 625 [51] possesses such desirable characteristics as a high melting point (of about 1560 K), high design strengths at high service temperatures, good density, excellent fabricability, easy availability, and lends itself to additive manufacturing techniques (which this project intends to explore the possibility of). All pertinent properties of Inconel 625 are presented in table 6.1.

The thrust chamber coolant, which constitutes the entire fuel flow, has a mass flow rate of $\dot{m}_f = 2.950580 \text{ kg/s}$. Assuming a fuel pressure drop of 0.5 times the combustion chamber pressure distributed between the cooling jacket and the injector assembly [13], we adopt a coolant inlet pressure of $P_f = 1.5 P_{cc} = 9000 \text{ kPa}$. Besides, the coolant inlet temperature is presumed to be 100 K which corresponds to a density of 445.340 kg/m^3 at the stated inlet pressure. The local flow velocity of the coolant requisite for adequate convective heat transfer within the channels at every location along the thrust chamber profile can be determined using the Sieder–Tate equation [13]. The equation comprises of such parameters as the Nusselt number, the Reynolds number, the Prandtl number, the coolant constant, its heat transfer coefficient, thermal conductivity, dynamic viscosity, specific heat,

Table 6.1.: Physical, mechanical and thermal properties of Inconel 625. [51]

Melting temperature	1560	K
Upper service temperature	1255	K
Density	8440	kg/m ³
Specific heat capacity	620	J/kg/K
Young's modulus	147.5	GPa
Poisson's ratio	0.336	
Ultimate strength	284.1	MPa
Yield strength	275.8	MPa
Ultimate strength (Room temp.)	965.3	MPa
Yield strength (Room temp.)	479.2	MPa
Thermal conductivity	22.8	W/m/K
Linear expansion coefficient	15.8	μm/m/K

density, and the like, all of which vary with both temperature and pressure of the coolant. Instead, we run RPA [41] to iteratively ascertain the number and dimensions of the channels at all crucial thrust chamber locations, and verify via trial-and-error that the maximum wall temperature at any location stays below the softening temperature of Inconel 625.

We rationally select a maximum allowable working stress of $\sigma_{w.inn} = 200$ MPa and a maximum allowable wall temperature of $T_{w.max} = 1000$ K for the entire thrust chamber inner jacket, both values being well below their respective safe limits for Inconel 625. The superalloy [51] has a softening temperature of around 1100 K and a yield stress of about 275 MPa at such elevated temperatures. The working stress, in conjunction with internal pressure and radius along the thrust chamber profile, obtains us a thickness of $t_{w.inn} = 1.00$ mm that can safely be adopted as the minimum wall thickness throughout the inner jacket. A conservative value for the inner wall thickness is deemed acceptable not only because it reduces temperature drops and thermal stresses across the wall but also because the inner jacket, being a non-structural component, does not endure the induced mechanical loads usually associated with rocket engine operation.

For the thrust chamber outer shell, we consider a design stress of $\sigma_{w.out} = 400$ MPa, twice as much that of the inner wall owing to the much cooler operating temperatures of the outer wall, and a safety factor of 2.0 so as to accommodate any uncertainty in loads, vibrations or shocks. This, together with the higher coolant pressure, results in an outer wall thickness of $t_{w.out} = 3.00$ mm. The ribs between the milled channels have a minimum thickness of $t_{rib} = 0.75$ mm—25% thinner than that of the inner wall because of the cooler working temperatures as well as the balanced loading conditions within the cooling channels.

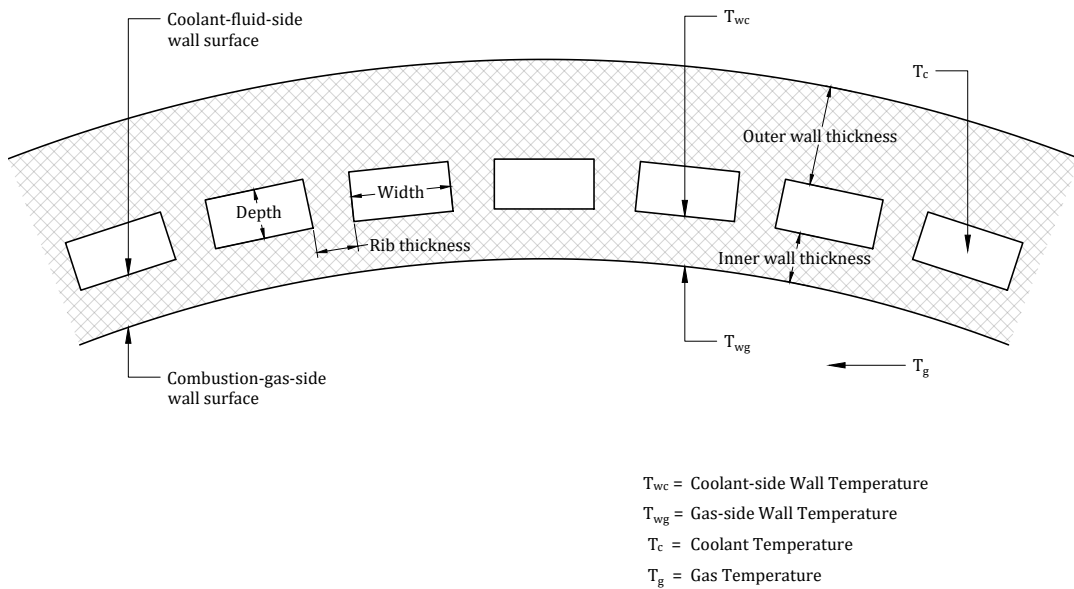


Figure 6.4.: Configuration layout of the thrust chamber cooling jacket.

In order to investigate the temperature distribution along the inner wall and by extension the coolant pressure drop, we preliminarily test with selecting the number of channels between 50 and 150 while varying the channel depth between 0.75 mm and 7.50 mm at each key thrust chamber location. We employ a jacket design with 100 channels—resulting in the channel widths of 3.40 mm around the chamber, 1.35 mm at the throat, and 7.22 mm near the exit of the nozzle—and a uniform depth of 1.00 mm throughout the channel profile. Such a configuration offers an optimum combination of heat transfer rates and hydraulic losses within the channels as well as inert mass and fabrication feasibility for the engine.

All crucial inner wall and coolant parameters at key thrust chamber sections are summarized in table 6.2. Moreover, the convective heat flux distribution along the

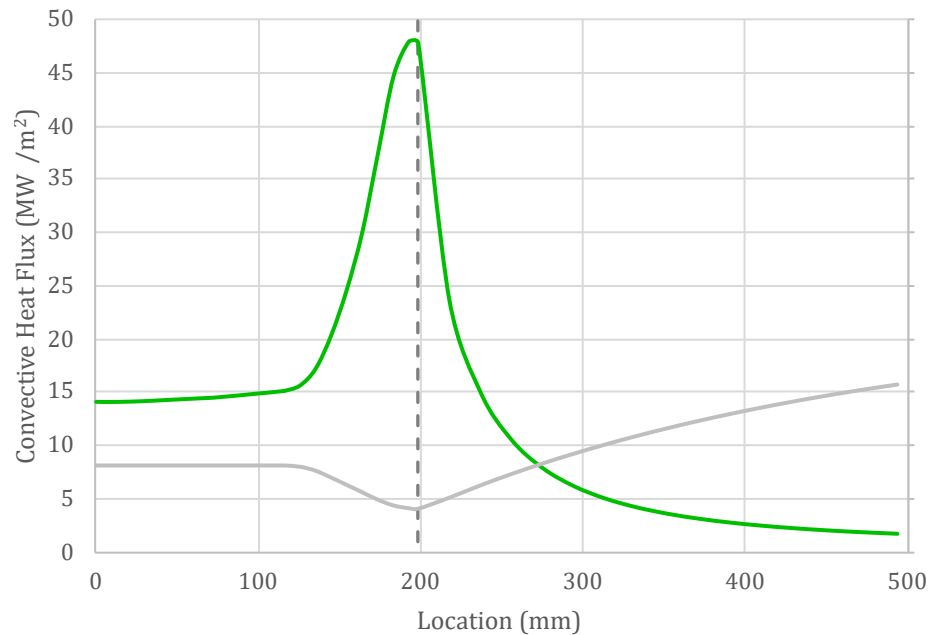


Figure 6.5.: Axial distribution of convective heat flux on the inner thrust chamber wall. [41]

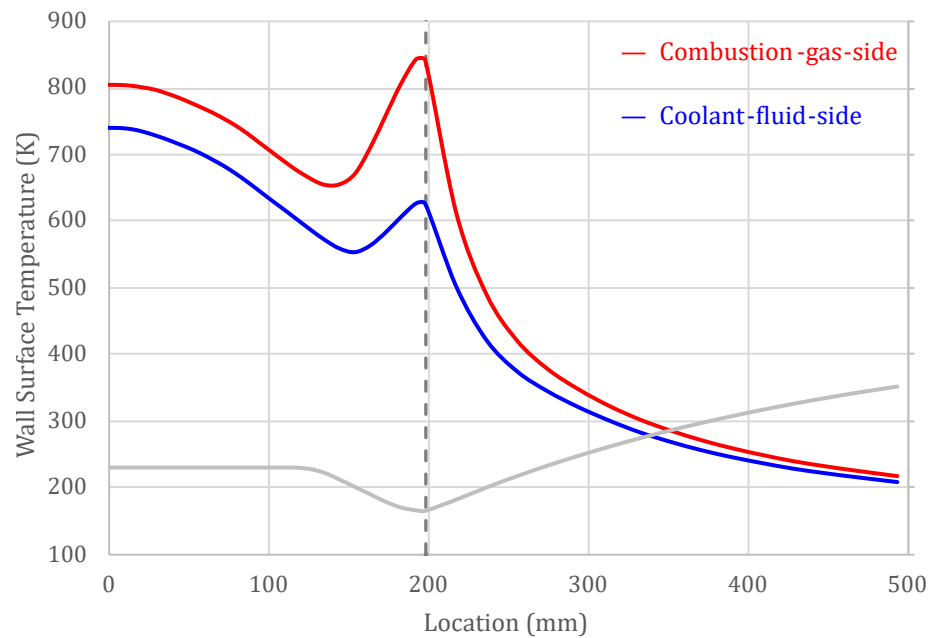


Figure 6.6.: Axial distribution of temperature on the thrust chamber inner wall surfaces. [41]

Table 6.2.: Cooling jacket parameters at key thrust chamber sections.

	CHAMBER	THROAT	EXIT	
Channel width	3.40	1.35	7.22	mm
Channel depth	1.00	1.00	1.00	mm
Cumulative area	339.69	135.49	722.16	mm ²
Film coefficient	5.52	18.47	0.56	kW/m ² /K
Heat flux	16904.82	48902.60	1830.23	kW/m ²
Flow velocity	68.97	72.35	8.90	m/s

inner wall, the temperature distribution on the wall surfaces, and the variation of both pressure and temperature for the coolant are plotted in figures 6.5, 6.6, and 6.7 respectively.

We recognize that the combustion-gas-side wall surface reaches its peak temperatures both at the throat, due to the immense rates of heat flux around this region,

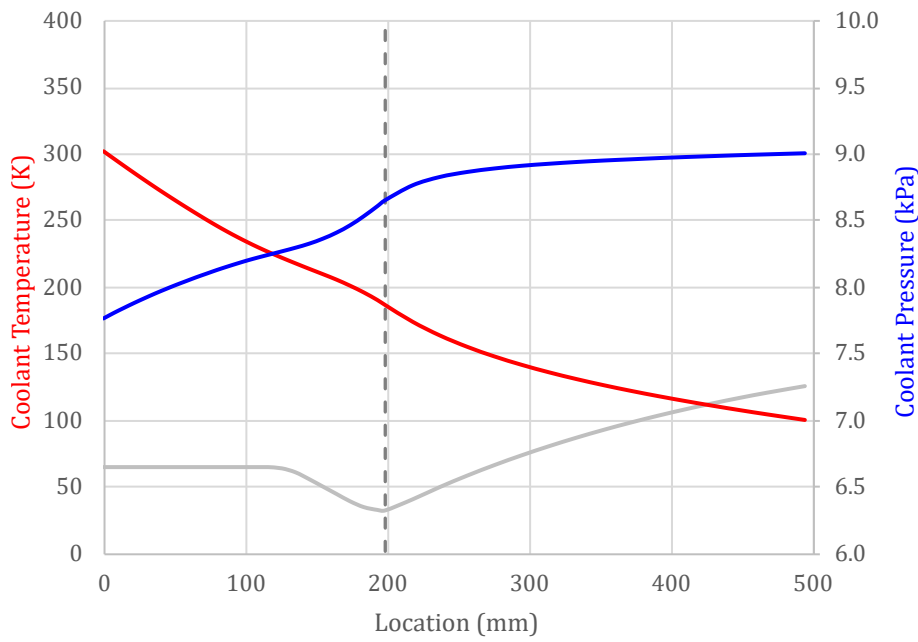


Figure 6.7.: Axial variation of both temperature and pressure for the coolant within the cooling jacket. [41]

as well as near the injector, because of the gradual accretion of coolant temperature that culminates at this section. Likewise, the coolant-fluid-side wall surface temperature reaches its highest towards the injector end after a small spike near the throat. Regardless, our maximum wall surface temperature, of 842.84 K, lies well below the softening temperature of Inconel 625. In addition, the coolant obtains an outlet pressure of 7772 kPa and a bulk temperature of 301.98 K within the jacket, thereby transitioning the liquid fuel into a supercritical fluid; methane has a critical pressure and a critical temperature of 4604 kPa and 190.58 K respectively.

6.1.2 Upper-Stage Thrust Chamber

As stated earlier, the upper-stage thrust chamber employs a regeneratively cooled section down to an area ratio of 15 and a radiatively cooled section towards aft of the divergent nozzle extension. Depicted schematically in figure 6.8, such an arrangement is feasible due to the moderate heat transfer criteria near the nozzle exit. Because the highest gas temperature in the region is about 1200 K, we opt to use Niobium C-103—a refractory-metal alloy with 10% hafnium and 1% titanium constituents—as the wall material for the radiative section. Nb C-103 has a melting point of 2620 K, an upper service temperature of 1755 K, a thermal conductivity of 44.6 W/m/K, a density of 8850 kg/m³ and an emissivity of 0.92, in addition to such properties as high tensile strength, good corrosion resistivity and excellent formability [61].

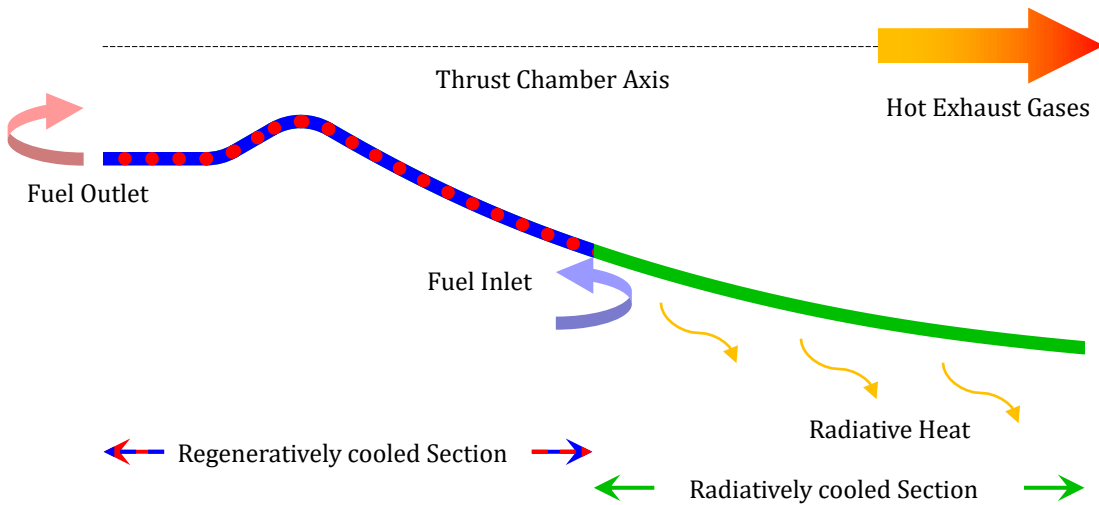


Figure 6.8.: Schematic diagram of the upper-stage regenerative/radiative cooling thrust chamber.

With a uniform wall thickness of $t_{w,rad} = 1.00$ mm, the nozzle extension obtains a peak wall surface temperature of 1584.13 K—a value well within the operating

temperature threshold for the material. The wall surface temperature distribution for the entire thrust chamber wall is presented in figure 6.9.

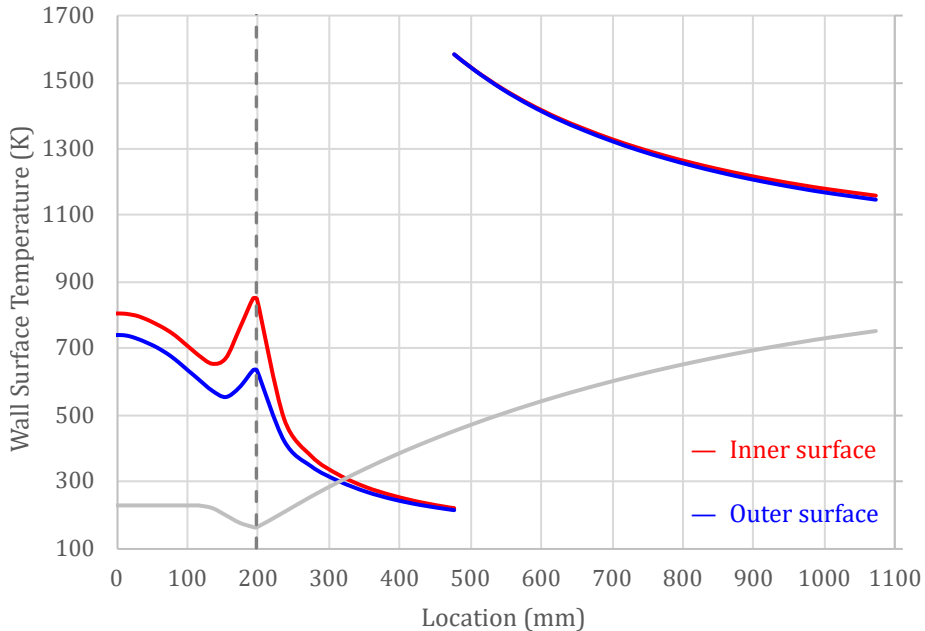


Figure 6.9.: Axial distribution of temperature on the upper-stage thrust chamber wall surfaces. [41]

6.2 INJECTOR DESIGN

The quintessential function of an injector is to inject propellants into the combustion chamber in the correct proportions and the right conditions to yield efficient and stable combustion. Placed at the forward end of the combustion chamber, the injector also performs the structural task of closing off the top of the thrust chamber against the combustion fluid it contains and transferring the generated thrust into the structure of the rocket. High combustion efficiencies can be obtained from metered distribution, proper atomization and uniform mixing of the propellants at their required flow rates and mixture ratios. Combustion stability is also a crucial requirement for a satisfactory injector design, since “high performance can become secondary if the injector is easily triggered into destructive instabilities” [13, p. 105]. Stable operation depends in good part on the selection of the injector element type and the provision for damping any oscillatory phenomena.

The design of an injector, much like other application before, entails numerous conditions and considerations [12]. The selection of injection elements has largely

been dominated by the type of propellants used, the collective properties of the bipropellant combination, and the conditions for propellant injection prior to ignition. And the placement of the elements on the injector plate has predominantly been determined by the spatial distribution of spray atomization and vaporization, the provisions for uniform mass distribution of and adequate mixing interaction between the propellants after ignition, and the possibility for tailoring the mixture ratio distribution to minimize chamber wall heat flux. Considering the aforementioned criteria and with regard to the LOX/LCH₄ bipropellant combination, we examine below the applicability of a few injection elements and manifold configurations for our combustion chamber.

6.2.1 Injection Elements

Depending on the pattern of oxidizer and fuel injection into the combustion chamber, injection elements may broadly be classified into the following types [13] [12] [62].

Showerhead Injectors

A *showerhead* element is among the simplest injection elements and typically injects axial non-impinging streams of either oxidizer or fuel from each orifice into the combustion chamber. These elements exhibit low rates of mass transfer across the injector, and rely on turbulence and diffusion between the jets and the combustion fluid in order to achieve adequate atomization and mixing. Because of their non-uniformity in spray distribution across the injector face and their ineffective bipropellant atomization and mixing along the chamber length, these elements are seldom used for primary thrust generation. Their poor atomization and mixing characteristics, however, make them well suited for film cooling applications, with the fuel jets acting as coolant between the combustion fluid and the chamber wall.

Impinging Injectors

The *like impinging* elements accomplish atomization by the self-impingement of respective jets from oxidizer doublets and fuel doublets. Mixing of the propellants is achieved downstream of the jet impingement point and takes place as a result of turbulent intermixing between adjacent oxidizer and fuel spray fans. Effective atomization occurs as a function of injection velocity, impingement angle and impingement distance. And attainment of efficient mixing is dependent upon the relative geometric arrangement of and between oxidizer doublets and fuel doublets, such as orifice size, spacing between respective fans and fan inclination

angle. Again, *like quadlet* elements are pairs of *like doublets* that are canted toward each other in order to induce better bipropellant mixing and deliver higher combustion performance for similar atomization and vaporization efficiencies and equal number of impinging pairs.

Unlike the above however, the *unlike impinging* elements such as *unlike doublets* impinge an oxidizer jet directly upon a fuel jet, and achieve virtually all atomization and mixing in the immediate vicinity of the impingement point. Ignition and combustion of the bipropellant mixture occur closer to the injector face and result in a relatively high injector plate heat flux. Unlike doublets work best for propellant combinations which have nearly equal oxidizer and fuel injection orifice areas and nearly equal injection stream momentum ratios. And again, *unlike triplet* elements impinge two opposing jets of one propellant upon a single jet of the other propellant, and are arranged in oxidizer-fuel-oxidizer or fuel-oxidizer-fuel configurations depending upon properties of the bipropellant mixture and characteristics such as droplet atomization, spray distribution, mixing uniformity and thermal compatibility. While unlike impinging elements tend to produce finer atomization and better mixing than like impinging elements of comparable orifice dimensions and pressure drops, they tend to exhibit poorer spatial controllability of spray distribution and higher susceptibility toward combustion instabilities.

Concentric Injectors

A *concentric*—or *coaxial*—injection element injects two concentric streams of propellants, with the central jet usually being the oxidizer while the annular jet typically being the fuel, in a self-impinging conical spray pattern into the combustion chamber. The already atomized and mixed spray from each element further impinges on sprays from adjacent elements to produce an even finer atomized and better mixed bipropellant spray. Ignition and combustion of the mixture, much like for unlike impinging elements, occur fairly close to the impingement point. Because of their indirect nature of propellant impingement, these elements require proportionately lower fuel-to-oxidizer injection velocity ratios in order for sufficient injection momentum differences to adequately atomize and mix the propellant jets. Now, it can be difficult to achieve uniform combustion fluid distribution and tailored bipropellant mixture ratios across an injector face with concentric injection elements without evoking combustion instability conditions.

Shear coaxial injectors are typically used with liquid oxidizer and gaseous fuel combinations since these elements require even larger injection momentum dissimilarities between the propellant jets to satisfactorily shear the streams for effective

atomization and mixing. And with their relatively narrow spray exit cone angles, these elements tend to cause high temperatures near the convergent nozzle section of a thrust chamber because of incomplete combustion of oxidizer droplets by the end of the chamber length.

Swirl coaxial injectors, on the other hand, can be used with liquid/liquid, liquid/gaseous or gaseous/gaseous bipropellant combinations, for these elements induce a swirl motion on either of or both the bipropellant jets, either by tangential flow into the element or by mechanical channels inside the element, prior to their injection which helps self-atomize the swirled stream without the added assistance of the other stream. These elements, because of their rather wide spray cones, can cause overheating of the forward section of a thrust chamber if positioned too close to the perimeter of an injector plate due to impingement of the oxidizer spray near the forward chamber wall.

Hybrid Injectors

A hybrid injection element, such as a *pintle* injector, is one that combines two or more of the elements above into a single unit for the injection of bipropellants into the combustion chamber. In the pintle element, one propellant flows down the inside of the pintle and is ejected radially through a series of holes or slots near the tip of the pintle while the other propellant leaves the manifold through an annular sheet around the base of the pintle. Depending on the propellant flowing inside the pintle tip, pintle flows are classified as either oxidizer-centered or fuel-centered patterns. Among the crucial advantages of a pintle injector are its inherent combustion stability, deep throttling capability, small dribble volume and face shutoff features.

6.2.2 Design of Injection Elements

Considering the benefits and limitations of each injection element above and referring to a few successful design studies [60] [63] [64], we employ unlike type impingement elements for the primary injection of oxidizer and fuel in our project. Figure 6.10 sketches a typical unlike doublet impingement injection pattern. Perhaps the most crucial parameter in the design of an injection element is the propellant pressure drop across the injector. A high pressure drop—although strains resources within the feed system—increases injection velocity of the propellants, which not only aids in their atomization and mixing, thereby ensuring a more complete and stable combustion, but also mitigates the inefficiencies associated with propellant dribbling. We opt for a loss in pressure equal to 25% of the combustion

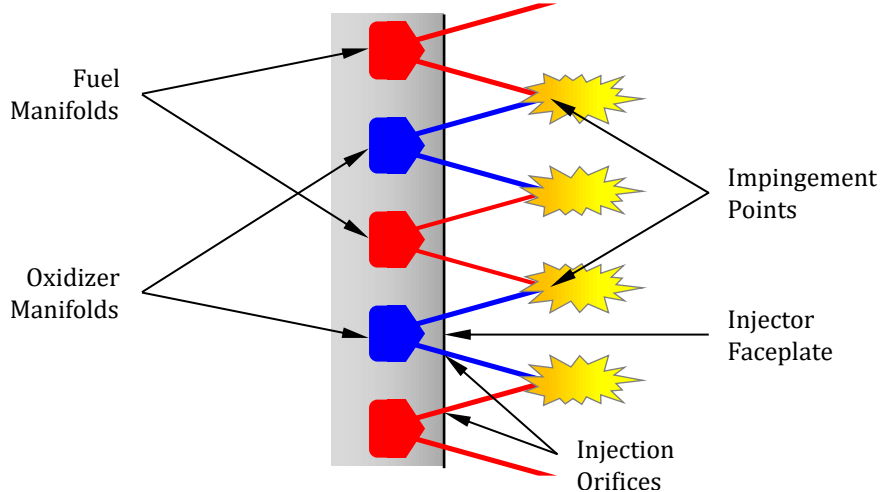


Figure 6.10.: Typical injection configuration of an unlike doublet impingement injector. [12]

chamber pressure, resulting in an injector pressure of $P_{inj} = 1.25 P_{cc} = 7500 \text{ kPa}$ and a pressure drop of $\Delta P = 1500 \text{ kPa}$ across the injection orifice system.

For the flow of an incompressible fluid through hydraulic orifices, the mass flow rate \dot{m} and the injection velocity v can be expressed as

$$\dot{m} = C_d A \sqrt{2 \Delta P \rho} \quad (6.1)$$

$$v = C_d \sqrt{2 \Delta P / \rho} \quad (6.2)$$

where, C_d is the dimensionless discharge coefficient, A the cumulative cross-sectional area of the orifices, and ρ the propellant mass density. The injection temperature of the oxidizer is assumed to be about 95 K. And from subsection 6.1.1, we determined the fuel temperature following its passage through the thrust chamber heat exchanger to be around 305 K. These temperatures (and pressures) correspond to densities of $\rho_{inj,o} = 1134.26 \text{ kg/m}^3$ and $\rho_{inj,f} = 53.17 \text{ kg/m}^3$ for the oxidizer and the fuel respectively.

It is now apparent that a discharge coefficient approaching unity maximizes the injection velocity for a given pressure drop. Therefore, assuming “smooth well-rounded entrances to injection holes with clean bores” [12, p. 282], we cautiously adopt a discharge coefficient of 0.80 for our injector assembly. Doing so gives us propellant injection velocities of $v_{inj,o} = 41.14 \text{ m/s}$ and $v_{inj,f} = 190.03 \text{ m/s}$, and thus a fuel-to-oxidizer velocity ratio of 4.62. Since the velocity ratio falls below the minimum range (of 10) typical for a coaxial injection element [13] [60], our

selection of the impingement type injector can be deemed appropriate.

From the propellant mass flow rates of $\dot{m}_o = 8.114096 \text{ kg/s}$ and $\dot{m}_f = 2.950580 \text{ kg/s}$, we obtain cumulative injection areas of $A_{inj,o} = 173.87 \text{ mm}^2$ and $A_{inj,f} = 292.03 \text{ mm}^2$. Now, [62] asserts that for unlike impingement elements, a specific oxidizer-to-fuel orifice diameter ratio is necessary for an optimum mixing efficiency. This ratio, when the impingement angle is 60° , can be expressed as

$$\left(\frac{d_o}{d_f}\right)^2 = M \left(\frac{\rho_{inj,f}}{\rho_{inj,o}} \left(\frac{\dot{m}_o}{\dot{m}_f} \right)^2 \right)^{0.7} \quad (6.3)$$

where, M represents the mixing factor for a specific injection element. For 1-on-1 and 2-on-1 unlike element types, the mixing factors equal 1.0 and 1.6 respectively.

Again, [62] affirms that, even for an optimum diameter configuration, the smaller the orifice diameter, the finer is the droplet size, the higher becomes the vaporization rate and level of mixing, and the better becomes the performance. This implies maximizing the number of oxidizer and fuel orifices within the feasibility of fabrication. From references [63] and [64], and with consideration to the above design aspects (without delving deep into any complications relevant to combustion instabilities), we preliminarily adopt 120 oxidizer orifices, which results ideally in 96 fuel orifices.

However, by employing a marginally smaller fuel orifice at the expense of a slightly higher pressure drop (There in fact is the pressure budget available within the fuel feed system to accommodate this!), we opt to match the number of oxidizer and fuel orifices to 120 each. Doing so gives us orifice diameters of $D_{ori,o} = 1.36 \text{ mm}$ and $D_{ori,f} = 1.76 \text{ mm}$. The unlike doublet element sets are arranged in two concentric patterns on the injector faceplate with 80 pairs on the outer ring divided evenly into two rows of 48 and 32 elements and 40 pairs on the inner ring distributed again into two rows of 24 and 16 elements. The configuration layout of our injector is presented in figure 6.11.

Because performance is further enhanced “when the resultant momentum of impinging streams is approximately axial” [12, p. 283], and since the impingement angle has been accepted as 60° , our oxidizer and fuel orifices are oriented at 38° and 22° respectively from the thrust chamber axis towards one another. Any net spray momentum can effectively be cancelled by directing the injection element pairs from the inner ring and the outer ring at each other.

In order to abate the adverse effects of jet misimpingement from long partially-

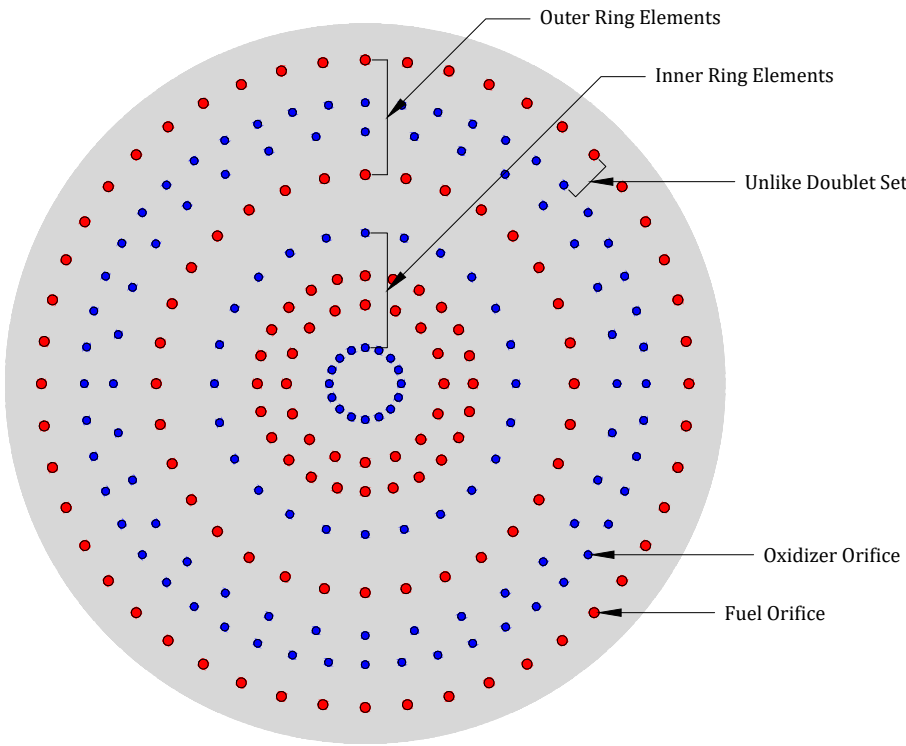


Figure 6.11.: Configuration layout of the injector faceplate. The colours blue and red represent the oxidizer and fuel orifices respectively. Distance within the unlike doublet set orifices equals 7.738 mm. Propellant impingement occurs at 6.528 mm from the injector surface.

disintegrated propellant streams, the ratio of free-stream jet length to injection orifice diameter ought to be, as [62] suggests, between 5 and 7. With our length-to-diameter ratios approximately 6 and 4 for the oxidizer and fuel jets respectively, we obtain an impingement distance of 6.528 mm from the injector faceplate, thus resulting in a distance of 7.738 mm between centres of the orifices within a doublet set. Now, to adequately manage heat flux to the injector, we choose Inconel 625 [51] as the material for the injector assembly. Table 6.3 below summarizes all pertinent parameters for our injector.

6.3 LAUNCH VEHICLE SPECIFICS

Our study, through the sections covered thus far, has revolved around design details of the engine assembly and/or its associated subsystems. This section, instead, encompasses the launch vehicle specifics, such as engine configurations, mass ratios, mission velocities, and the like.

Table 6.3.: Design parameters for the injector faceplate assembly.

Combustion chamber pressure P_{cc}	6000	kPa
Injector pressure P_{inj}	7500	kPa
Oxidizer parameters		
Mass flow rate \dot{m}_o	8.114	kg/s
Density $\rho_{inj,o}$	1134.26	kg/m ³
Injection velocity $v_{inj,o}$	41.14	m/s
Injection area $A_{inj,o}$	173.87	mm ²
Orifices	120	
Orifice diameter $D_{ori,o}$	1.36	mm
Orifice angle $\theta_{ori,o}$	38°	
Fuel parameters		
Mass flow rate \dot{m}_f	2.951	kg/s
Density $\rho_{inj,f}$	53.17	kg/m ³
Injection velocity $v_{inj,f}$	190.03	m/s
Injection area $A_{inj,f}$	292.03	mm ²
Orifices	120	
Orifice diameter $D_{ori,f}$	1.76	mm
Orifice angle $\theta_{ori,f}$	22°	
Impingement distance	6.528	mm
Orifice distance	7.738	mm
Material	Inconel 625	

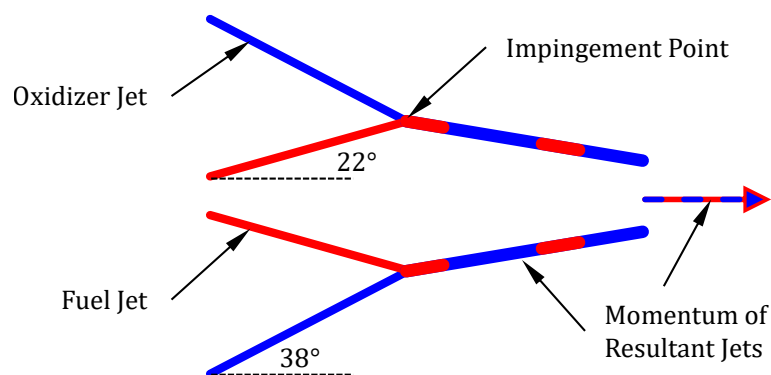


Figure 6.12.: Propellant impingement angles and resultant jet momentum.

As stated earlier, the objective of our hypothetical mission is to deliver a light payload into LEO. With a payload capacity of 200 kg, we target for a perfectly circular orbit at 500 km altitude. This corresponds to an orbital speed of 7616.6 m/s for our payload. In order to accommodate losses due to gravity and drag during the flight, we add a factor of 1.25 times the orbital speed and obtain a mission velocity “delta-v” of about 9500 m/s.

In section 5.2, we have established mass flow rate of $\dot{m} = 11.064676 \text{ kg/s}$ and average exhaust velocities of $v_{e.1st} = 2700.486590 \text{ m/s}$ and $v_{e.2nd} = 3335.262440 \text{ m/s}$ for our thrust chamber variants. (Here, the lesser quantity between the average exhaust velocity v_e and the effective exhaust velocity c is considered the exhaust velocity.) We initially ascertain delta-v and mass metrics for the upper stage and finally move on to those of the booster stage with its engine cluster configuration.

Now, launch vehicles typically have structural mass fractions between 10 to 15% for the upper stage and between 5 to 10% for the booster stage to account for the inert hardware exclusive to the stage [12]. Structural mass fraction is usually higher for the upper stage than for the booster stage because the net propellant mass is significantly higher for the latter than for the former [65, ch. 13]; with larger tanks having better volume-to-surface ratios, there is less tankage mass per unit propellant mass for the booster stage. We, therefore, conservatively adopt structural mass fractions of $\varepsilon_{2nd} = 0.125$ and $\varepsilon_{1st} = 0.075$ which correspond to propellant mass fractions of $\zeta_{2nd} = 87.5\%$ and $\zeta_{1st} = 92.5\%$ for both our rocket stages respectively.

The rocket equation for a twin-stage launcher is expanded and expressed as [12]

$$\Delta v = v_{e.1st} \ln \left(\frac{1}{\text{MR}_{1st}} \right) + v_{e.2nd} \ln \left(\frac{1}{\text{MR}_{2nd}} \right) \quad (6.4)$$

Equation 6.4 can be expressed in terms of structural mass fraction as [65, ch. 13]

$$\Delta v = v_{e.1st} \ln \left(\frac{v_{e.1st} \eta - 1}{v_{e.1st} \varepsilon_{1st} \eta} \right) + v_{e.2nd} \ln \left(\frac{v_{e.2nd} \eta - 1}{v_{e.2nd} \varepsilon_{2nd} \eta} \right) \quad (6.5)$$

where, η represents the Lagrange multiplier and can be solved iteratively.

From the mass flow rate and for a given burn time, we attain the stage propellant mass as

$$m_{pro} = \dot{m} t_b \quad (6.6)$$

Using the above propellant and structural mass fractions, we obtain both wet and

dry stage masses as

$$m_{wet} = \frac{1}{\zeta} m_{pro} \quad (6.7a)$$

$$m_{dry} = \varepsilon m_{wet} \quad (6.7b)$$

For the operation duration of each stage, we follow standard flight profiles for small launchers (such as that of Electron [7])—wherein the upper stage operates anywhere upwards of 180 s, whereas the booster stage operates anywhere up to 180 s. And in order to generate the necessary liftoff/ascent thrust, we require a cluster of thrust chambers in a parallel burn arrangement for the first stage. In addition, we add in 15 s of propellant margin to each engine to account for start and stop transients during startup and shutdown operations. By cycling the nominal engine burn time between 180 s, 240 s and 300 s for the upper stage and between 120 s, 150 s and 180 s for the booster stage while employing a cluster of 5, 7 and 9 thrust chambers therein, we determine both the liftoff mass and the delta-v for our launch vehicle using the equations above. Results of the calculations are presented in table 6.4.

It is observed that certain combinations of burn times and cluster configurations are downright unfeasible in terms of delta-v, while others yield a rather exorbitant liftoff mass. Further, a few combinations offer superfluous mission velocities at the expense of unwarranted launch vehicle mass. Any combination with a delta-v below 9500 m/s or a liftoff mass above 20 t or a 2% excess delta-v is disregarded, and thus greyed out in our tabulation. (The relative Δv therein corresponds to the minimum mission velocity, i.e., 9500 m/s.)

We decide to allow some margin (of nearly +1.5%) for vehicle performance with regard to delta-v and select a nominal burn time of $t_{b,2ND} = 180$ s for the upper stage and of $t_{b,1ST} = 120$ s for the booster stage with a cluster of 9 thrust chambers. Accordingly, the total propellant budget is of 195 s and 135 s for both the stages. Correspondingly, we obtain a mass of around $m_{LV} = 17200$ kg and a delta-v of about $\Delta v_{LV} = 9636.6$ m/s for our launch vehicle. The delta-v budget is thereby distributed as 5527.7 m/s for the second stage and 4108.9 m/s for the first stage. Configuration of the engine cluster on our booster is portrayed in figure 6.13.

6.4 SUMMARY

Having designed the thrust chamber configurations for our twin-staged rocket, we

Table 6.4.: Preliminary mass and delta-v values of our launch vehicle for the nominal burn times at the structural mass fractions considered.

$t_{b.2ND}$ (s)	$t_{b.1ST}$ (s)	N_{1ST}	m_{LV} (kg)	Δv_{LV} (m/s)	Δv (%)
180	120	5	10740.065	8737.897657	- 8.02
		7	13969.755	9254.994660	- 2.58
		9	17199.444	9636.616163	+ 1.44
	150	5	12534.337	9046.236315	- 4.78
		7	16481.735	9560.492737	+ 0.64
		9	20429.133	9932.552578	+ 4.55
	180	5	14328.609	9302.881990	- 2.07
		7	18993.716	9809.524642	+ 3.26
		9	23658.822	10170.068158	+ 7.05
240	120	5	11498.786	8623.640510	- 9.22
		7	14728.475	9134.503122	- 3.85
		9	17958.165	9520.982790	+ 0.22
	150	5	13293.058	8926.512933	- 6.04
		7	17240.456	9443.232184	- 0.60
		9	21187.854	9826.458687	+ 3.44
	180	5	15087.330	9182.552216	- 3.34
		7	19752.436	9698.835948	+ 2.09
		9	24417.543	10075.459234	+ 6.06
300	120	5	12257.507	8510.705225	- 10.41
		7	15487.196	9009.029692	- 5.17
		9	18716.885	9393.550566	- 1.12
	150	5	14051.778	8804.780770	- 7.32
		7	17999.177	9315.668708	- 1.94
		9	21946.575	9702.146594	+ 2.13
	180	5	15846.050	9056.480901	- 4.67
		7	20511.157	9572.711413	+ 0.77
		9	25176.264	9956.830522	+ 4.81
(+ 15 s)		(+ 15 s)			

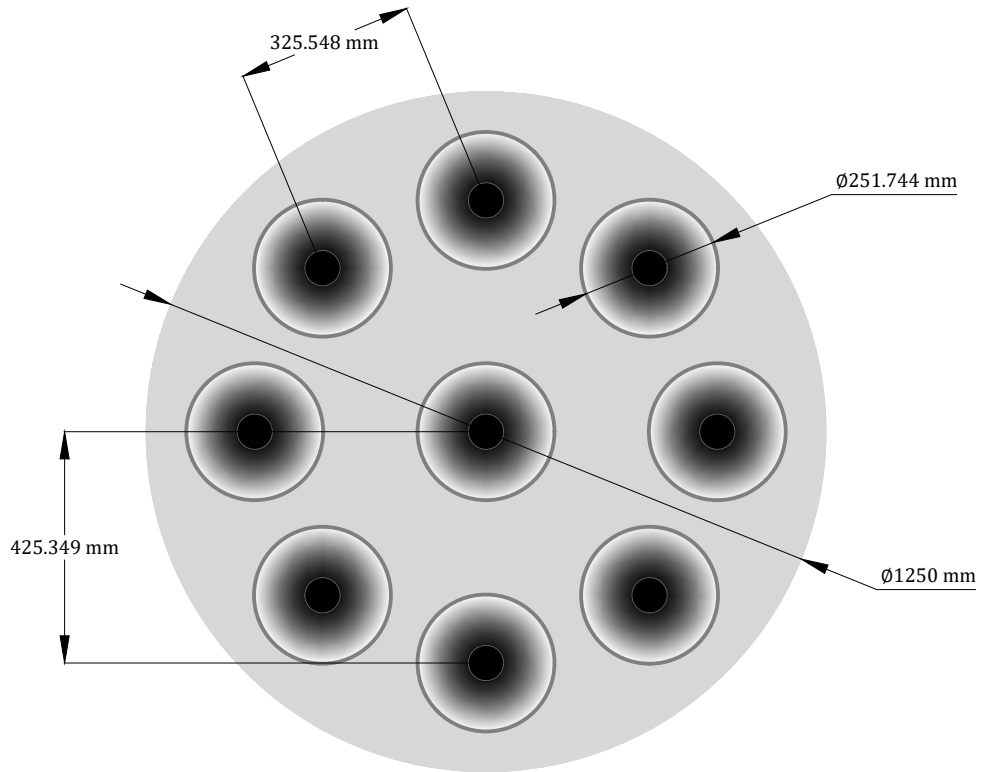


Figure 6.13.: Cluster configuration of the booster stage engines.

delve into analysing the heat transfer and mitigating the excessive thermal energy by implementing steady-state cooling techniques. Our one-dimensional analyses are performed only at the most critical wall sections, such as around key regions of the chamber, at and near the throat, and towards the exit of the nozzle. We employ regenerative cooling for the combustion chamber and the nozzle down to an area ratio of 15, i.e., encompassing entirety of the booster-stage engine, beyond which we employ radiative cooling owing to the relatively moderate temperatures therein, i.e., towards aft of the upper-stage nozzle.

In our regeneratively cooled thrust chamber, the main fuel feed is circulated as the coolant fluid within the cooling jacket. We inject the coolant through the inlet manifold at the nozzle exit from where it flows unidirectionally upward within the longitudinal channels following which it enters into the injector manifold. We adopt a milled-slot jacket design and choose Inconel 625 as the wall material for both the inner jacket and the outer shell. With heat flux being the highest at the throat, the cooling channels at the region are designed for the maximum flow velocity and the minimum cross-sectional area. For our radiatively cooled nozzle segment, we use Niobium C-103 as the wall material. Our mechanisms

and materials are, as a consequence, perfectly compatible to withstand the high thermal energy generated within our propulsion system.

Next, we explore design principles of the injector and look into the process of metering, injection, atomization, vaporization and mixing of propellants for their effective combustion. High combustion efficiency and good combustion stability can be obtained from metered distribution, proper atomization and uniform mixing of the propellants at their required flow rates and mixture ratios. Having considered quite a few injection elements, we select the unlike type impingement elements for our thrust chamber design, wherein an oxidizer jet is impinged directly upon a fuel jet and virtually all atomization and mixing is achieved in the immediate vicinity of the impingement point; ignition and combustion occur closer to the injector face, which results in a relatively high injector plate heat flux. The unlike doublet element sets are arranged in two concentric patterns with 80 pairs on the outer ring divided evenly into two rows of 48 and 32 elements and 40 pairs on the inner ring distributed again into two rows of 24 and 16 elements.

In the end, we strive to determine the tentative liftoff mass of our launch vehicle from mass flow rates and average exhaust velocities of both our engines as well as with rational assumptions of structural mass fractions for each stage. Following standard flight profiles for small launchers, we obtain the operation duration for both our rocket stages. And using the minimum mission velocity necessary, we conclude to employ a cluster of 9 engines in a parallel burn arrangement on the booster stage of our rocket.

7

CONCLUSION

The objective of our project has been to preliminarily develop a “new generation” propulsion system that could be employed in both the booster stage and the upper stage of a small-lift orbital-class rocket to deliver a light payload into LEO. The launch vehicle for our hypothetical mission is to have a delta-v budget of 9500 m/s and a payload capacity of 200 kg. And above all, both the liquid rocket engines are obligated to be as similar to each other as pragmatically possible. Such an engine configuration for a launch vehicle closely mirrors that of Rutherford/Electron from Rocket Lab or of Merlin/Falcon 9 from SpaceX.

While the conception of engine systems driven by electric pump feed systems or running on the liquid oxygen and liquid methane mixture is anything but new, what is novel about our study is the amalgamation of these two conceptualizations to design one single propulsion system that can outperform current rocket engines in the comparable performance class. In that regard, we have unequivocally demonstrated the feasibility of our liquid rocket propulsion system to accomplish a typical real-life mission, such as the one outlined in our objectives.

7.1 CONCLUSION

We, at first, looked into the theoretical notions of ideal propulsion systems along with the means to incorporate losses to the incurred over-performance through realistic correction factors. In our quest to select the best bipropellant combination for our mission, we investigated a multitude of propellant characteristics critical to engine performance. In particular, we analysed the combustion of LOX with LH₂, RP-1 and LCH₄ using CEA for a frozen composition flow, and determined

the best mixture ratio to yield the highest specific impulse: for hydrolox, kerolox and methalox bipropellants, the optimum mixture ratios are 5.50, 2.25 and 2.75 respectively. We also examined the variation of combustion temperature, characteristic velocity and molecular mass as functions of mixture ratio. For the LOX/LCH₄ combination at its optimum mixture ratio, we obtained a chamber temperature of 3350.27 K at a chamber pressure of 6894.757 kPa.

With regard to the propellant feed system, we determined fairly quickly that a pressure feed system would be anything but suitable for our engine specifications. We concentrated our effort studying the pump feed system instead. Having skimmed over a few pump-fed-engine cycles, we considered the gas generator cycle as the yardstick for turbopump system performance. With electropump systems, we investigated the significance of both power density and energy density in governing the battery pack mass. Since the mass penalty from battery packs was historically a major bottleneck in the development of electric-pump-fed rocket engines, adoption of such a system has only just become feasible owing to recent advancements in battery technologies. Electropump feed systems at present, therefore, offer comparable performance to—or even can outperform—gas generator cycle engines under the right conditions. In our study, where the thrust is 30 kN and the combustion chamber pressure is 6000 kPa, we realized that the electropump system yielded lesser mass, thereby better mass ratio, than the turbopump feed system for nominal engine burn times above 88 s; and the switch from critical power density to critical energy density for our battery pack occurred around 150 s.

Next, we designed two thrust chamber versions for our launch vehicle—a sea-level variant with a nozzle expansion area ratio of 15 for the booster stage and a vacuum-optimized variant with an area ratio of 100 for the upper stage. We obtained a few crucial thrust chamber performance parameters from CEA and calculated the rest with MATLAB using the theoretical equations from chapter 2. In order to account for a slight over-performance, we incorporated somewhat conservative correction factors and worked out all our results again. Consequently, we attained a mass flow rate of 11.065 kg/s and a throat diameter of 65 mm. For our convergent-divergent nozzle contours, we examined the expansion and shock characteristics of the exhaust jet based on TIC, TOC, TOP, and the method of characteristics techniques. We subsequently adopted the TOP “thrust optimised parabolic” contour for both the nozzle variants, and ascertained all pertinent internal dimensions therein.

Thereafter, we investigated heat transfer from the combustion fluid to the thrust chamber walls; we employed steady-state mitigation methods to manage the high thermal energy within and obviate any failure. We implemented regenerative cool-

ing, using Inconel 625, for the combustion chamber and the nozzle down to an area ratio of 15, i.e., encompassing entirety of the booster-stage engine, beyond which we implemented radiative cooling, with Niobium C-103, owing to the relatively moderate temperatures, i.e., towards aft of the upper-stage nozzle. Further, we designed the injector assembly to inject propellants in the correct proportions and the right conditions so as to yield efficient and stable combustion. Our injector faceplate, also of Inconel 625, comprised two concentric patterns of unlike impingement doublet sets—with 80 pairs on the outer ring divided evenly into two rows of 48 and 32 elements and 40 pairs on the inner ring distributed again into two rows of 24 and 16 elements.

We, at last, strived to evaluate the liftoff mass of our launch vehicle from performance parameters of both the thrust chamber configurations as well as with rational assumptions of structural mass fractions for each stage: 0.075 being for the first and 0.125 for the second. In doing so, and following standard flight profiles, we settled for nominal operation durations of 120 s and 180 s (plus 15 s each to accommodate transient conditions) for the booster stage and the upper stage respectively; both our burn times are, as compared to electropump systems, well within the optimal envelope for electropump feed system performance. With a cluster of 9 engines on the booster, our hypothetical launch vehicle has a mass of roughly 17200 kg (200 kg of which is the payload) and a delta-v of approximately 9600 m/s—quite within the desirable range of specifications for small-lift orbital-class twin-stage rockets of today. And thus concludes the preliminary design of our propulsion system.

7.2 LIMITATIONS & FUTURE WORK

Limitations

Having accomplished our objective, we do recognize that our design has, much like any other preliminary design, certain implicit shortcomings. First, ours is a theoretical study based on idealistic models of the principles/processes involved in liquid rocket propulsion systems. We adopt our crucial (and in a way initial) performance figures, viz. combustion chamber temperature, effective molecular mass and specific heat ratio, from CEA with the assumption that NASA CEA does not overestimate its values; that need not necessarily be so. Likewise, RPA generates results, both operational and analytical, that could be a touch optimistic. Adopting perfect correction factors, consequently, is perhaps a tricky endeavour. Without any empirical data to back our design, this study is to be deemed but

provisional.

Second, while we have proven the viability of electric-pump-fed engine cycles to outperform both pressure feed systems and turbopump feed systems, the outperformance only exists within a narrow window of engine operating conditions. Put another way, above or below a certain combustion chamber pressure or a given burn time or a specific thrust, a pressure-fed system or a turbopump-fed system instead will reign supreme. Moreover, the batteries at present are still quite limited by the technologies of today. Nonetheless, with advances in battery technologies lately, there is room for improvement of both power density and energy density so as to save mass and/or enhance performance. Regardless, it will perhaps be a very long time (if not downright impossible) before batteries come anywhere near matching the energy densities of fossil fuels.

And third, throughout our design process, we have performed numerous iterations to various parameters whenever we realized the need of our propulsion system to attain and/or assume values and/or details necessary for the mission objective. Our reconsiderations might have been, at times, somewhat biased towards achieving a favourable design outcome. An instance of this would be the structural mass fraction of each stage to obtain a certain launcher liftoff mass. Another similar example would likely be the selection of nozzle contours for both our engines. But because little could be done to verify the validity of our theoretical design, we regard all our assumptions perfectly sound in this design study.

Future Work

The ultimate realization of the task initiated in this project is, quite unequivocally, the flight qualification of our “new generation” propulsion system for a small-lift orbital-class launch vehicle like ours. A more prudent target would perhaps be to hot-fire test our rocket engine after finalising the preliminary design. To accomplish that, we ought to perform at least the following tasks:

- Conduct computational fluid dynamics analyses for the combustion fluid characteristics to preclude instabilities and model stable engine operating conditions.
- Design the rotodynamic pump elements, like the stator assembly, the rotor assembly, inducer, impeller, diffuser vanes and volute for our propellant feed properties.
- Develop the remainder systems and/or components necessary for engine operation, such as detailed designs for injector manifolds, ignition devices,

propellant feed assembly, engine control system, thrust vector control, to list a few.

- Perform structural and thermal analyses using the more appropriate tools.
- Build and test the liquid rocket propulsion system.

With this, we conclude the objective of this project and the scope of my thesis.

A

CEA COMPUTATION

This appendix presents the output of the CEA analysis [39] on the basis of which we perform all our design calculations.

NASA-GLENN CHEMICAL EQUILIBRIUM PROGRAM CEA2, FEBRUARY 5, 2004
BY BONNIE MCBRIDE AND SANFORD GORDON
REFS: NASA RP-1311, PART I, 1994 AND NASA RP-1311, PART II, 1996

```
# Problem Type: "Rocket" (Infinite Area Combustor)
prob case=METHALOX_6000_2.750 ro frozen
# Pressure (1 value):
p,bar= 60
# Supersonic Area Ratio (2 values):
supar= 15, 100
# Oxidizer/Fuel Wt. ratio (1 value):
o/f= 2.75
# You selected the following fuels and oxidizers:
reac
fuel CH4(L)           wt%=100.0000
oxid O2(L)             wt%=100.0000
# You selected these options for output:
output short
output massf
output siunits
# The following line is the end of your CEA input file!
end
```

THEORETICAL ROCKET PERFORMANCE ASSUMING FROZEN COMPOSITION

Pin = 870.2 PSIA

	REACTANT	WT FRACTION (SEE NOTE)	ENERGY KJ/KG-MOL	TEMP K
FUEL	CH4 (L)	1.0000000	-89233.000	111.643
OXIDANT	O2 (L)	1.0000000	-12979.000	90.170

O/F= 2.75000 %FUEL= 26.666667

R, EQ.RATIO= 1.450641 PHI, EQ.RATIO= 1.450641

	CHAMBER	THROAT	EXIT	EXIT
Pinf/P	1.0000	1.7781	150.46	1962.05
P, BAR	60.000	33.744	0.39878	0.03058
T, K	3338.67	3022.92	1316.75	748.18
RHO, KG/CU M	4.2155 0	2.6185 0	7.1040-2	9.5875-3
H, KJ/KG	-1780.73	-2560.60	-6489.75	-7597.78
U, KJ/KG	-3204.04	-3849.31	-7051.10	-7916.74
G, KJ/KG	-45034.4	-41723.7	-23548.7	-17290.7
S, KJ/(KG) (K)	12.9554	12.9554	12.9554	12.9554
M, (1/n)	19.503	19.503	19.503	19.503
Cp, KJ/(KG) (K)	2.4856	2.4533	2.0726	1.8173
GAMMAS	1.2070	1.2103	1.2590	1.3065
SON VEL, M/SEC	1310.7	1248.9	840.7	645.5
MACH NUMBER	0.000	1.000	3.651	5.284

PERFORMANCE PARAMETERS

Ae/At	1.0000	15.000	100.00
CSTAR, M/SEC	1834.8	1834.8	1834.8
CF	0.6807	1.6726	1.8590
Ivac, M/SEC	2280.8	3251.8	3504.4
Isp, M/SEC	1248.9	3068.9	3410.9

MASS FRACTIONS

*CO	0.34809	*CO2	0.18457	COOH	0.00002
*H	0.00110	HCO	0.00003	HO2	0.00002
*H2	0.01741	HCOOH	0.00001	H2O	0.42142
H2O2	0.00001	*O	0.00148	*OH	0.02273
*O2	0.00312				

* THERMODYNAMIC PROPERTIES FITTED TO 20000.K

NOTE. WEIGHT FRACTION OF FUEL IN TOTAL FUELS AND OF OXIDANT IN
TOTAL OXIDANTS

B

MATLAB SCRIPT

This appendix presents the MATLAB code snippets, together with their output, used to compute our design parameters. The code is divided into three sections: first, for the thrust chamber performance; second, for the pump feed system, and third, for the rocket mass and delta-v metrics.

B.1 THRUST CHAMBER PARAMETERS

```
1 %%%%%%%%
2
3 function [stage] = ThrustChamberParameters()
4
5 G0 = 9.80665;           %% Earth Standard Gravity
6 RSTAR = 8.314462618;    %% Universal Gas Constant
7 rho_O = 1142.0;          %% Density Oxidizer
8 rho_F = 0422.8;          %% Density Fuel
9 P_cc = 6000000;          %% Combustion Chamber Pressure
10 OF = 2.75;               %% O/F Mixture Ratio
11 F_nomi = 0;
12 C_L = 100;                %% Characteristics Lines
13 MLNC = 0;                 %% Function Switch
14 expn = 0;                  %% Nozzle Expansion Area Ratio
15 P_e = 0;
16 P_ext = 0;
17 T_cc = 3338.67;          %% Combustion Chamber Temperature
18 MM = 19.503;              %% Effective Molecular Mass
19 k = 1.2070;                %% Specific Heat Ratio
20 k_t = 1.2103;              %% Specific Heat Ratio _ Throat
```

```

21 rho_cc = 4.2155;           %% Combustion Chamber Fluid Density
22 D_t = 60.00;
23 D_t = 65.00;
24 % D_t = 64.465918;        %% optimized for 30kN uncorrected
25 % D_t = 65.130381;        %% optimized for 30kN corrected
26
27 alpha = 15;
28 beta = 30;
29 cntr = 4.0;                %% Nozzle Contraction Area Ratio
30 L_STAR = 0.70;              %% Characteristic Length
31 corrfact_c_STAR = 0.99;
32 corrfact_C_f = 0.97;
33 corrfact_m_DOT = 1.01;
34
35 DS = 275000000;            %% Design Strength = Yield @ Temp
36 FS = 1.375000;             %% Safety Factor = 0.727272727273
37 chnl_num = 100;             %% Coolant Channel Number
38 dpth = 1.000;               %% Coolant Jacket Depth
39 MAWT = 1000.0;              %% Maximum Allowable Wall Temperature
40 DeltaP = 0.25;              %% Pressure Drop
41 rho_inj_O = 1134.2600;      %% Density @ 1M K & 7.50 MPa
42 rho_inj_F = 0053.1685;      %% Density @ 1M K & 7.50 MPa
43 ori_num_O = 120;             %% D = 1.36
44 ori_num_F = 120;             %% D = 1.76
45 angle_ori_O = 38;
46 angle_ori_F = 22;
47 dis_coeff = 0.80;            %% Discharge Coefficient
48 MixFac = 1.0;                %% Unlike 1-1 Mixing Factor // 0.696
49 FACNUM = 4;                  %% Factor Number
50 LENFAC = 0;                  %% Length Factor
51
52 %      xxxxxxxxxxxxxxxxxxxxxxxxxxxxxxxxxxxxxxxxxxxxxxxxxxxxxxxx
53
54 clc;
55
56 fprintf('\n\n');
57 fprintf('\tRocket Stages:\n\n');
58 fprintf('\t\t1\t\tFIRST\t\tBOOSTER\t\t\t\t•\n');
59 fprintf('\t\t2\t\tSECOND\t\tUPPER\t\t\t\t••\n');
60 fprintf('\n\t\tPlease enter your stage... ');
61 stage = input(' ', 's');
62 % stage = '1';
63 % stage = '2';
64 % stage = 'AA';              %% Select! Stage! Here! Now! Go!

```

```

65 if (strcmpi(stage, '1') == 1)
66     stage = '1ST';
67     stagename = 'FIRST      "BOOSTER"      STAGE'      •;
68     expn = 15;
69     k_e = 1.2590;
70     P_e = 39878;
71     P_ext_aa = 101325.0;
72     P_ext_zz = 2.067920;
73     div_i = 28;
74     div_e = 10;
75 end
76
77 if (strcmpi(stage, '2') == 1)
78     stage = '2ND';
79     stagename = 'SECOND      "UPPER"      STAGE'      ••;
80     expn = 100;
81     k_e = 1.3065;
82     P_e = 03058;
83     P_ext_aa = 0.886280;
84     P_ext_zz = 000000.0;
85     div_i = 34;
86     div_e = 08;
87 end
88 %
89 %      xxxxxxxxxxxxxxxxxxxxxxxxxxxxxxxxxxxxxxxxxxxxxxxxxxxxxxxx
90
91 P_ext = P_ext_zz;
92 P_ext = P_ext_aa;
93 % % P_ext = P_e;
94 A_t = pi / 4 * D_t ^ 2 / 1000000;
95 D_e = D_t * sqrt(expn);
96 A_e = pi / 4 * D_e ^ 2 / 1000000;
97 corrfact_c = corrfact_c_STAR * corrfact_C_f;
98 corrfact_F = corrfact_c_STAR * corrfact_C_f * corrfact_m_DOT;
99 corrfact_n = corrfact_c * corrfact_c ;
100 M = MM / 1000;
101 R = RSTAR / M;
102 c_STAR = (sqrt(k * R * T_cc)) / (k * sqrt((2 / (k + 1)) ...
103           ^ ((k + 1) / (k - 1))));
104 c_STAR = c_STAR * corrfact_c_STAR;
105 C_f_opt = sqrt(2 * k * k / (k - 1) * (2 / (k + 1)) ...
106           ^ ((k + 1) / (k - 1)) * (1 - (P_e / P_cc) ^ ((k - 1) / k)));
107 C_f = C_f_opt + (P_e - P_ext) / P_cc * expn;
108 C_f = C_f * corrfact_C_f;

```

```

109 m_DOT = P_cc * A_t / c_STAR;
110 m_DOT = m_DOT * corrfact_m_DOT;
111 c = c_STAR * C_f;
112 I_s = c_STAR * C_f / G0;
113 F = P_cc * C_f * A_t * corrfact_m_DOT;
114 F_DASH = F * corrfact_F;%% => F' = F'' × corrfact_F ^ 2
115 m_DOT_DASH = 30000 / c;
116 % m_DOT_DASH = F / c;
117 % m_DOT_DASH = F_DASH / c;
118 P_t = P_cc * (2 / (k_t + 1)) ^ (k_t / (k_t - 1));
119 T_t = T_cc / ((P_cc / P_t) ^ ((k_t - 1) / k_t));
120 T_e = T_cc / ((P_cc / P_e) ^ ((k_e - 1) / k_e));
121 SV_cc = R * T_cc / P_cc;
122 SV_t = SV_cc * (P_cc / P_t) ^ (1 / k_t);
123 SV_e = SV_cc * (P_cc / P_e) ^ (1 / k_e);
124 v_cc = sqrt(2 * k / (k - 1) * R * T_cc * (1 - (P_cc / P_cc) ...
125           ^ ((k - 1) / k)));
126 v_t = sqrt(2 * k_t / (k_t - 1) * R * T_cc * (1 - (P_t / P_cc) ...
127           ^ ((k_t - 1) / k_t)));
128 v_e = c - (P_e - P_ext) * A_e / m_DOT;
129 sv_e = sqrt(k_e * R * T_e);
130 M_e = v_e / sv_e;
131
132 Cline = C_L;
133 Gamma = k_e;
134 Mexit = M_e;
135 Stage = stage;
136 if (MLNC > 0)
137     MLNC = MinimumLengthNozzleContour(Cline, Gamma, Mexit, Stage);
138 end
139 velout = min(c, v_e);
140
141 L_N = (D_e - D_t) / tand(alpha) / 2;
142 L_n = 0.8 * L_N;
143 V_cc = L_STAR * A_t;
144 D_cc = D_t * sqrt(cntr);
145 A_cc = pi / 4 * D_cc ^ 2 / 1000000;
146 L_f = (D_cc - D_t) / tand(beta) / 2;
147 V_f = pi / 24 / tand(beta) * (D_cc * D_cc * D_cc - D_t * D_t * D_t);
148 V_c = V_cc * 1000000000 - V_f;
149 L_c = V_c / (pi / 4 * D_cc * D_cc);
150 L_cc = L_c + L_f;
151 L = L_n + L_cc;
152 t_s = V_cc * rho_cc / m_DOT;

```

```

153 m_DOT_O = 1 / (OF + 1) * m_DOT * (OF);
154 m_DOT_F = 1 / (OF + 1) * m_DOT * 1.00;
155
156 MAWS = DS / FS;           %% Maximum Allowable Working Stress
157 thck_inn = (D_cc * 0.50) * (P_cc * 0.50) / (MAWS * 1.00) * (1.00);
158 thck_inn = round(thck_inn);
159 thck_out = (D_cc * 0.50) * (P_cc * 1.50) / (MAWS * 2.00) * (2.00);
160 thck_out = round(thck_out);
161 thck_rib = thck_inn * 0.75;
162 thck_cc = thck_inn;
163 thck_t = thck_inn;
164 thck_e = thck_inn;
165 crcm_cc = 2 * pi * (D_cc / 2 + thck_cc);
166 crcm_t = 2 * pi * (D_t / 2 + thck_t);
167 crcm_e = 2 * pi * (D_e / 2 + thck_e);
168 chnl_wdth_cc = crcm_cc / chnl_num - thck_rib;
169 chnl_wdth_t = crcm_t / chnl_num - thck_rib;
170 chnl_wdth_e = crcm_e / chnl_num - thck_rib;
171 chnl_dpth_cc = dpth;
172 chnl_dpth_t = dpth;
173 chnl_dpth_e = dpth;
174
175 DeltaP = P_cc * DeltaP;
176 P_inj = P_cc + DeltaP;
177 A_inj_O = m_DOT_O / (dis_coeff * sqrt(2 * DeltaP * rho_inj_O));
178 A_inj_F = m_DOT_F / (dis_coeff * sqrt(2 * DeltaP * rho_inj_F));
179 A_ori_O = A_inj_O / ori_num_O;
180 A_ori_F = A_inj_F / ori_num_F;
181 D_ori_O = sqrt(A_ori_O * 4 / pi) * 1000;
182 D_ori_F = sqrt(A_ori_F * 4 / pi) * 1000;
183 v_inj_O = dis_coeff * sqrt(2 * DeltaP / rho_inj_O);
184 v_inj_F = dis_coeff * sqrt(2 * DeltaP / rho_inj_F);
185 v_inj_O = m_DOT_O / rho_inj_O / A_inj_O;
186 v_inj_F = m_DOT_F / rho_inj_F / A_inj_F;
187 D_ori_OF = sqrt(MixFac * ((rho_inj_F / rho_inj_O) ...
188     * (m_DOT_O / m_DOT_F) ^ 2) ^ (0.7));
189 angle_inj = atand(((m_DOT_O * v_inj_O * sind(angle_ori_O)) ...
190     - (m_DOT_F * v_inj_F * sind(angle_ori_F))) ...
191     / ((m_DOT_O * v_inj_O * cosd(angle_ori_O)) ...
192     + (m_DOT_F * v_inj_F * cosd(angle_ori_F))));
193 LENFAC = (D_ori_F * cosd(angle_ori_F)) / (D_ori_O * cosd(angle_ori_O));
194 LENFAC = LENFAC * FACNUM;
195 len_O = D_ori_O * LENFAC;
196 len_F = D_ori_F * FACNUM;

```

```
197 hei_O = cosd(angle_ori_O) * len_O;
198 hei_F = cosd(angle_ori_F) * len_F;
199 dis_O = sind(angle_ori_O) * len_O;
200 dis_F = sind(angle_ori_F) * len_F;
201 lenfac_O = len_O / D_ori_O;
202 lenfac_F = len_F / D_ori_F;
203 dis_oriinj = dis_O + dis_F;
204 dis_imping = max(hei_O, hei_F);
205
206 %      xxxxxxxxxxxxxxxxxxxxxxxxxxxxxxxxxxxxxxxxxxxxxxxxxxxxxxxx
207
208 stage = 'ZZ';
209
210 return;
211
212 end
213
214 %%
```

1st Stage Thrust Chamber Output

```

1 >>
2
3     FIRST      "BOOSTER"      STAGE    •
4
5 -----
6
7         cofa_c*      =      99.000      [...]
8         cofa_Cf      =      97.000      [...]
9         cofa_mDOT    =     101.000      [...]
10        cofa_c      =     96.030000    [...]
11        cofa_F      =     96.990300    [...]
12        cofa_n      =     92.217609    [...]
13        R          =     426.317111    [...]
14        c*         =    1817.399932    [...]
15        Cf          =     1.485907    [...]
16        c           =    2700.486590    [...]
17        Is          =     275.372996    [...]
18        F           =    29880.009851    [...]
19        F'          =    28980.711195    [...]
20        mDOT        =     11.064676    [...]
21        mDOT.O     =     8.114096    [...]
22        mDOT.F     =     2.950580    [...]
23        mDOT'       =     11.109109    [...]
24
25        vinj.O     =     41.142844    [...]
26        vinj.F     =    190.030543    [...]
27        Ainj.O     =    173.873427    [...]
28        Ainj.F     =    292.031450    [...]
29        Aori.O     =     1.448945    [...]
30        Aori.F     =     2.433595    [...]
31        Dori.O     =     1.358254    [...]
32        Dori.F     =     1.760270    [...]
33        Θinj       =     -0.330     [...]
34        Θ.O         =      38        [...]
35        Θ.F         =      22        [...]
36        DSoriinj   =     7.738160    [...]
37        DSimping   =     6.528375    [...]
38        FAC.O      =     6.099467    [...]
39        FAC.F      =     4.000000    [...]
40        LEN.O      =      8.28       [...]
41        LEN.F      =      7.04       [...]
42        HEI.O      =    6.528375114945 [...]
43        HEI.F      =    6.528375114945 [...]

```

44				
45	Dcc	=	130.000000	[...]
46	Rcc	=	65.000000	[...]
47	CRCMcc	=	414.690230	[...]
48	Acc	=	0.013273228961	[...]
49	Lc	=	142.163203	[...]
50	Lf	=	56.291651	[...]
51	Lcc	=	198.454855	[...]
52	Pcc	=	6000000.000000	[...]
53	Tcc	=	3338.670000	[...]
54	SVcc	=	0.237222	[...]
55	vcc	=	0.000000	[...]
56	Vcc	=	0.002322815068	[...]
57	ts	=	0.000885	[...]
58				
59	Dt	=	65.000000	[...]
60	Rt	=	32.500000	[...]
61	CRCMt	=	210.486708	[...]
62	At	=	0.003318307240	[...]
63	Pt	=	3374871.418511	[...]
64	Tt	=	3021.010723	[...]
65	SVt	=	0.381617	[...]
66	vt	=	1248.501396	[...]
67	θcon	=	30	[...]
68	θd.i	=	28	[...]
69	θd.e	=	10	[...]
70				
71	De	=	251.743918	[...]
72	Re	=	125.871959	[...]
73	CRCM ϵ	=	797.160027	[...]
74	Ae	=	0.049774608605	[...]
75	Pe	=	39878.000	[...]
76	Te	=	1190.248514	[...]
77	SVe	=	12.724392	[...]
78	ve	=	2976.906822	[...]
79	Me	=	3.724493	[...]
80	Pext	=	101325.000	[...]
81				
82	LN	=	348.468894	[...]
83	Ln	=	278.775115	[...]
84	Rtu	=	48.750	[...]
85	Rtd	=	13.000	[...]
86				
87	L	=	477.229970	[...]

```

88   THCK.i    =    1.000      [...]
89   THCK.o    =    3.000      [...]
90   DPTHcc   =    1.000      [...]
91   DPTHt    =    1.000      [...]
92   DPTHe    =    1.000      [...]
93   WDTHcc   =    3.397      [...]
94   WDTHt    =    1.355      [...]
95   WDTHe    =    7.222      [...]
96
97   VelOut   =  2700.486590391  [...]
98   L*        =    0.700000    [...]
99   Expn      =    15.000
100  Cntr      =    4.000
101  MAWS     =    200.000      [...]
102  Pcc/Pe    =    150.458900
103  Pcc/Pext  =          59
104  Pe/Pext   =    0.393565
105  Pe-Pext   =   -61447.000
106  F../mDOT  =    0.266667
107  O../mDOT  =    0.733333
108  De/Dcc   =    1.936492
109  De/Dt    =    3.872983
110  Lcc/Dcc  =    1.526576
111  Lc/Lf    =    2.525476
112  ..F/..O   =    4.618799
113  Acc/..O   =    76.338456
114  Acc/..F   =    45.451368
115
116 -----
117
118 >>

```

2nd Stage Thrust Chamber Output

```

1 >>
2
3     SECOND    "UPPER"      STAGE    ••
4
5 -----
6
7         cofa_c*      =      99.000      [...]
8         cofa_Cf      =      97.000      [...]
9         cofa_mD0T     =     101.000      [...]
10        cofa_c      =    96.030000      [...]
11        cofa_F      =    96.990300      [...]
12        cofa_n      =    92.217609      [...]
13        R          =    426.317111      [...]
14        C*         =    1817.399932      [...]
15        Cf          =    1.885631      [...]
16        c           =    3426.945580      [...]
17        Is          =    349.451197      [...]
18        F           =    37918.043388      [...]
19        F'          =    36776.824036      [...]
20        mD0T       =    11.064676      [...]
21        mD0T.O     =    8.114096      [...]
22        mD0T.F     =    2.950580      [...]
23        mD0T'       =    8.754151      [...]
24
25        vinj.O     =    41.142844      [...]
26        vinj.F     =    190.030543      [...]
27        Ainj.O     =    173.873427      [...]
28        Ainj.F     =    292.031450      [...]
29        Aori.O     =    1.448945      [...]
30        Aori.F     =    2.433595      [...]
31        Dori.O     =    1.358254      [...]
32        Dori.F     =    1.760270      [...]
33        Θinj       =    -0.330      [...]
34        Θ.O         =    38          [...]
35        Θ.F         =    22          [...]
36        DSoriinj   =    7.738160      [...]
37        DSimping   =    6.528375      [...]
38        FAC.O      =    6.099467      [...]
39        FAC.F      =    4.000000      [...]
40        LEN.O       =    8.28          [...]
41        LEN.F       =    7.04          [...]
42        HEI.O       =    6.528375114945 [...]
43        HEI.F       =    6.528375114945 [...]

```

```

44
45     Dcc      =    130.000000      [...]
46     RCC      =    65.000000      [...]
47     CRCMcc   =    414.690230      [...]
48     Acc      =    0.013273228961 [...]
49     Lc       =    142.163203      [...]
50     Lf       =    56.291651      [...]
51     Lcc      =    198.454855      [...]
52     Pcc      =    6000000.000000 [...]
53     Tcc      =    3338.670000      [...]
54     SVcc     =    0.237222      [...]
55     vcc      =    0.000000      [...]
56     Vcc      =    0.002322815068 [...]
57     ts       =    0.000885      [...]
58
59     Dt       =    65.000000      [...]
60     Rt       =    32.500000      [...]
61     CRCMt    =    210.486708      [...]
62     At       =    0.003318307240 [...]
63     Pt       =    3374871.418511 [...]
64     Tt       =    3021.010723      [...]
65     SVt      =    0.381617      [...]
66     vt       =    1248.501396      [...]
67     θcon     =    30          [...]
68     θd.i     =    34          [...]
69     θd.e     =    8           [...]
70
71     De       =    650.000000      [...]
72     Re       =    325.000000      [...]
73     CRCMe    =    2048.318410      [...]
74     Ae       =    0.331830724035 [...]
75     Pe       =    3058.000       [...]
76     Te       =    563.787177      [...]
77     SVe      =    78.597816      [...]
78     ve       =    3335.262441      [...]
79     Me       =    5.951841      [...]
80     Pext     =    0.886        [...]
81
82     LN       =    1091.624861      [...]
83     Ln       =    873.299889      [...]
84     Rtu      =    48.750        [...]
85     Rtd      =    13.000        [...]
86
87     L         =    1071.754744      [...]

```

```
88      THCK.i    =    1.000          [...]
89      THCK.o    =    3.000          [...]
90      DPTHcc   =    1.000          [...]
91      DPTHt    =    1.000          [...]
92      DPTHe    =    1.000          [...]
93      WDTHcc   =    3.397          [...]
94      WDTHt    =    1.355          [...]
95      WDTHe    =   19.733          [...]
96
97      VelOut   =  3335.262440675  [...]
98      L*        =  0.700000        [...]
99      Expn      = 100.000
100     Cntr      =    4.000
101     MAWS      = 200.000          [...]
102     Pcc/Pe    = 1962.066710
103     Pcc/Pext  =    6769870
104     Pe/Pext   = 3450.376856
105     Pe-Pext   = 3057.114
106     F../mDOT  =    0.266667
107     O../mDOT  =    0.733333
108     De/Dcc    =    5.000000
109     De/Dt     = 10.000000
110     Lcc/Dcc   =    1.526576
111     Lc/Lf     =    2.525476
112     ..F/..O   =    4.618799
113     Acc/..O   =    76.338456
114     Acc/..F   =    45.451368
115
116 -----
117
118 >>
```

B.2 ENGINE CYCLE PARAMETERS

```

1 %%%%%%%%%%%%%%%%%%%%%%%%%%%%%%%%%%%%%%
2
3 function [cycle] = EngineCycleParameters()
4
5 cycle = 'AA';
6
7 G0 = 9.806650;           %% Gravity - Earth
8 P_cc = 6000000;          %% Pressure - Thrust Chamber
9 eta_op = 0.66;            %% Efficiency - Oxidizer Pump
10 eta_fp = 0.60;           %% Efficiency - Fuel Pump
11 eta_mot = 0.95;          %% Efficiency - Motor
12 eta_inv = 0.85;           %% Efficiency - Inverter
13 eta_bat = 0.90;           %% Efficiency - Battery
14 delta_op = 20000.00;       %% Density Power - Oxidizer Pump
15 delta_fp = 15000.00;       %% Density Power - Fuel Pump
16 delta_tp = 12500.00;       %% Density Power - Turbopump
17 delta_mot = 5500.00;        %% Density Power - Motor
18 delta_inv = 60000.00;       %% Density Power - Inverter
19 delta_batP = 6500.00;       %% Density Power - Battery
20 delta_batE = 300.00 * 3600; %% Density Energy - Battery
21                                         %% Density Power - Battery
22 delta_batP = delta_batP / 1000;
23                                         %% Density Power - Battery
24 delta_batE = delta_batE / 1000;
25                                         %% Density Energy - Battery
26 OF_gg = 0.333333;           %% Mass Mixture Ratio - Gas Generator W. F.
27 rho_o = 1142.00;             %% Density - Oxidizer
28 rho_f = 0422.80;             %% Density - Fuel
29 rho_gg = 12.6240;            %% Density - Gas Generator W. F.
30 rho_ggm = 8440.00;            %% Density - Gas Generator Material
31 dotm_op = 8.114096;           %% Mass Flow Rate - Oxidizer Pump
32 dotm_fp = 2.950580;           %% Mass Flow Rate - Fuel Pump
33 dotm_gg = 0.75 * (dotm_op + dotm_fp) / 100; %% Mass Flow Rate - Gas Generator W. F.
34                                         %% Mass Margin - Propellant
35 kappa_p = 1.05;                %% Safety Factor - Gas Generator
36 kappa_gg = 2.50;                %% Mass Margin - Battery Pack
37 kappa_bat = 1.25;               %% Head Rise - Oxidizer Pump
38 Deltap_op = 1.25 * P_cc / rho_o / G0; %% Head Rise - Fuel Pump
39                                         %% Pressure - Gas Generator
40 Deltap_fp = 1.50 * P_cc / rho_f / G0;
41                                         %% Strength - Gas Generator Material
42 p_gg = 1.00 * P_cc;            %% Strength - Gas Generator Material
43 sigma_ggm = 50000000;           %% Strength - Gas Generator Material

```

```

44 t_s = 0.0100; %% Stay Time - Gas Generator W. F.
45 t_b = 0; %% Burn Time - Thrust Chamber
46
47 ...
48 t_b = 135.00; %% Burn Time - 1ST STAGE
49 t_b = 195.00; %% Burn Time - 2ND STAGE
50 t_b = 00:01:1000; %% Burn Time - Thrust Chamber
51 t_b = [135 195]; %% Burn Time - Thrust Chamber
52 ...
53
54 P_op = 0; %% Power - Oxidizer Pump
55 P_fp = 0; %% Power - Fuel Pump
56 P_tp = 0; %% Power - Turbopump
57
58 m_o_TPFS = 0; %% Mass - TP Oxidizer
59 m_f_TPFS = 0; %% Mass - TP Fuel
60 m_tp_TPFS = 0; %% Mass - Turbopump
61 m_gg_TPFS = 0; %% Mass - Gas Generator
62 m_xo_TPFS = 0; %% Mass - Gas Generator Oxidizer
63 m_xf_TPFS = 0; %% Mass - Gas Generator Fuel
64 m_xx_TPFS = 0; %% Mass - Gas Generator Propellant
65 M_FS_TPFS = 0; %% Mass - TPFS - Feed System
66 M_P_TPFS = 0; %% Mass - TPFS - Propellant
67 MR_TPFS = 0; %% Mass Ratio - TPFS
68
69 m_o_EPFS = 0; %% Mass - EP Oxidizer
70 m_f_EPFS = 0; %% Mass - EP Fuel
71 m_op_EPFS = 0; %% Mass - Oxidizer Pump
72 m_fp_EPFS = 0; %% Mass - Fuel Pump
73 m_mot_EPFS = 0; %% Mass - Motor
74 m_inv_EPFS = 0; %% Mass - Inverter
75 m_bat_EPFS = 0; %% Mass - Battery
76 M_FS_EPFS = 0; %% Mass - EPFS - Feed System
77 M_P_EPFS = 0; %% Mass - EPFS - Propellant
78 MR_EPFS = 0; %% Mass Ratio - EPFS
79
80 M_TPFS = 0; %% Mass - TPFS
81 M_EPFS = 0; %% Mass - EPFS
82
83 %      xxxxxxxxxxxxxxxxxxxxxxxxxxxxxxxxxxxxxxxxxxxxxxxxxxxxxxxx
84
85 P_op = ((dotm_op * Deltap_op) / (eta_op * rho_o));
86 P_fp = ((dotm_fp * Deltap_fp) / (eta_fp * rho_f));
87 P_tp = P_op + P_fp;

```

```

88
89 m_o_TPFS = kappa_p * t_b * dotm_op;
90 m_f_TPFS = kappa_p * t_b * dotm_fp;
91 m_tp_TPFS = (1 / delta_tp) * (P_tp);
92 m_gg_TPFS = (3 / 2) * (rho_ggm / sigma_ggm) ...
93           * (dotm_gg * t_s / rho_gg) * p_gg * kappa_gg;
94 m_xo_TPFS = kappa_p * t_b * (1 / (OF_gg + 1) * (dotm_gg * OF_gg));
95 m_xf_TPFS = kappa_p * t_b * (1 / (OF_gg + 1) * (dotm_gg * 1.000));
96 m_xx_TPFS = m_xo_TPFS + m_xf_TPFS;
97 M_FS_TPFS = m_tp_TPFS + m_gg_TPFS + m_xx_TPFS;
98 M_P_TPFS = m_o_TPFS + m_f_TPFS;
99 MR_TPFS = M_FS_TPFS ./ M_P_TPFS .* 100;
100
101 m_o_EPFS = kappa_p * t_b * dotm_op;
102 m_f_EPFS = kappa_p * t_b * dotm_fp;
103 m_op_EPFS = (1 / delta_op) * P_op;
104 m_fp_EPFS = (1 / delta_fp) * P_fp;
105 m_mot_EPFS = (1 / delta_mot) * (P_tp);
106 m_inv_EPFS = (1 / (delta_inv * eta_mot)) * (P_tp);
107 m_bat_EPFS = (1 / (eta_inv * eta_mot)) * kappa_bat * (P_tp) ...
108           * (max((1 / (delta_batP)), (t_b / (delta_bate * eta_bat)))); 
109 M_FS_EPFS = m_op_EPFS + m_fp_EPFS ...
110           + m_mot_EPFS + m_inv_EPFS + m_bat_EPFS;
111 M_P_EPFS = m_o_EPFS + m_f_EPFS;
112 MR_EPFS = M_FS_EPFS ./ M_P_EPFS .* 100;
113
114 M_TPFS = m_o_TPFS + m_f_TPFS + m_tp_TPFS + m_gg_TPFS ...
115           + m_xo_TPFS + m_xf_TPFS;
116 M_EPFS = m_o_EPFS + m_f_EPFS + m_op_EPFS + m_fp_EPFS ...
117           + m_mot_EPFS + m_inv_EPFS + m_bat_EPFS;
118
119 %      xxxxxxxxxxxxxxxxxxxxxxxxxxxxxxxxxxxxxxxxxxxxxxxxxxxxxxxx
120
121 cycle = 'ZZ';
122
123 return;
124
125 end
126
127 %%%%%%%%

```

Engine Cycle Parameters Output

```

1 >>
2
3 -----
4
5     OP H.R.      =      669.691      [...]
6     FP H.R.      =     2170.635      [...]
7     OP P.        =      7.209      [...]
8     FP P.        =     25.247      [...]
9
10    GG M.        =      0.083      [...]
11    GG D.        =     50.073      [...]
12
13    *
14
15 -----
16
17
18 -----
19
20    •   T   P   F   S
21
22    MASS TPFS   =   1580.208520      [...]
23    MASS TPFS   =   2282.511167      [...]
24
25    →   M.o      =   1150173.108      [...]
26    →   M.o      =   1661361.156      [...]
27    →   M.f      =   418244.715      [...]
28    →   M.f      =   604131.255      [...]
29    →   M.tp      =      2.597      [...]
30    →   M.gg      =      24.967      [...]
31    →   M.xgg     =   11763.134      [...]
32    →   M.xgg     =   16991.193      [...]
33
34    →   P         =   1568.417823      [...]
35    →   P         =   2265.492411      [...]
36    →   FS        =      11.790697      [...]
37    →   FS        =      17.018756      [...]
38
39    →   FS / P   •   =      0.752      [...]
40    →   FS / P   •   =      0.751      [...]
41
42 -----
43

```

```

44
45 -----
46
47     •   E    P    F    S
48
49     MASS EPFS = 1576.155889 [...]
50     MASS EPFS = 2275.580356 [...]
51
52     → M.o = 1150173.108 [...]
53     → M.o = 1661361.156 [...]
54     → M.f = 418244.715 [...]
55     → M.f = 604131.255 [...]
56     → M.op = 0.360 [...]
57     → M.fp = 1.683 [...]
58     → M.mot = 5.901 [...]
59     → M.inv = 0.569 [...]
60     → M.bat = 7729.552 [...]
61     → M.bat = 10079.431 [...]
62
63     → P = 1568.417823 [...]
64     → P = 2265.492411 [...]
65     → FS = 7.738066 [...]
66     → FS = 10.087945 [...]
67
68     → FS / P • = 0.493 [...]
69     → FS / P • = 0.445 [...]
70
71 -----
72
73
74 -----
75
76     M TPFS = 1580.208520 [...]
77     M TPFS = 2282.511167 [...]
78
79     M EPFS = 1576.155889 [...]
80     M EPFS = 2275.580356 [...]
81
82     *
83
84 -----
85
86 >>

```

B.3 VEHICLE MASS PARAMETERS

```

1 %%%%%%
2
3 function [delta] = VehicleMassParameters()
4
5 delta = 'AA';
6
7 G0 = 9.80665;
8 R0 = 6371000;
9 mDOT = 11.064676254169;
10 mass_payl = 0200;           %% Payload Mass [kg]
11 orbit = 0500;             %% Orbit Altitude [km]
12 velo_1ST = 2700.486590390697; %% Exhaust Velocity
13 velo_2ND = 3335.262440674872; %% Exhaust Velocity
14 time_burn_1ST = 120;        %% Operation Duration == 135
15 time_burn_2ND = 180;        %% Operation Duration == 195
16 SMF_1ST = 0.075;           %% Structural Mass Fraction >> ΔT = 135
17 SMF_2ND = 0.125;           %% Structural Mass Fraction >> ΔT = 195
18 ETA = 0.000641075875;    %% 1# = 0.075 || 2# = 0.125 >> <<--
19 margin = 15;
20 NUM = 09;
21
22 %     xxxxxxxxxxxxxxxxxxxxxxxxxxxxxxxxxxxxxxxxxxxxxxxxxxxxxxxxxxxxx
23
24 orbit = orbit * 1000;
25 velo_orbit = R0 * sqrt(G0 / (R0 + orbit));
26 velo_orbit = sqrt(0.398600441 * 10 ^ 15 / (R0 + orbit));
27 velo_mission = velo_orbit * 1.250;
28 velo_mission = round(velo_mission, 2, "significant");
29
30 velo_delta_stage_1ST = velo_1ST * log((velo_1ST * ETA - 1) ...
31     / (velo_1ST * ETA * SMF_1ST));
32 velo_delta_stage_2ND = velo_2ND * log((velo_2ND * ETA - 1) ...
33     / (velo_2ND * ETA * SMF_2ND));
34 velo_delta_stage = velo_delta_stage_1ST + velo_delta_stage_2ND;
35
36 OMR_1ST = (velo_1ST * ETA - 1) / (velo_1ST * ETA * SMF_1ST);
37 OMR_2ND = (velo_2ND * ETA - 1) / (velo_2ND * ETA * SMF_2ND);
38 PMF_1ST = 1 - SMF_1ST;
39 PMF_2ND = 1 - SMF_2ND;
40 CHK_1ST = ETA * velo_1ST * (SMF_1ST * OMR_1ST - 1) ^ 2 + 2 ...
41     * SMF_1ST * OMR_1ST - 1;
42 CHK_2ND = ETA * velo_2ND * (SMF_2ND * OMR_2ND - 1) ^ 2 + 2 ...
43     * SMF_2ND * OMR_2ND - 1;

```

```

44 mass_wet_1ST = (OMR_1ST - 1) / (1 - OMR_1ST * SMF_1ST) ...
45           * (mass_payl + 000000000000);
46 mass_wet_2ND = (OMR_2ND - 1) / (1 - OMR_2ND * SMF_2ND) ...
47           * (mass_payl);
48 mass_wet_1ST = (OMR_1ST - 1) / (1 - OMR_1ST * SMF_1ST) ...
49           * (mass_payl + mass_wet_2ND);
50 mass_wet_2ND = (OMR_2ND - 1) / (1 - OMR_2ND * SMF_2ND) ...
51           * (mass_payl);
52 mass_dry_1ST = mass_wet_1ST * SMF_1ST;
53 mass_dry_2ND = mass_wet_2ND * SMF_2ND;
54 mass_prop_1ST = mass_wet_1ST - mass_wet_1ST * SMF_1ST;
55 mass_prop_2ND = mass_wet_2ND - mass_wet_2ND * SMF_2ND;
56 % time_burn_1ST = mass_prop_1ST / mDOT / NUM;
57 % time_burn_2ND = mass_prop_2ND / mDOT / 1.0;
58 % time_burn_1ST = round(time_burn_1ST, 2, "significant");
59 % time_burn_2ND = round(time_burn_2ND, 2, "significant");
60 time_burn_1ST = time_burn_1ST + margin;
61 time_burn_2ND = time_burn_2ND + margin;
62 mass_prop_1ST = mDOT * time_burn_1ST * NUM;
63 mass_prop_2ND = mDOT * time_burn_2ND * 1.0;
64 mass_wet_1ST = mass_prop_1ST / PMF_1ST;
65 mass_wet_2ND = mass_prop_2ND / PMF_2ND;
66 mass_dry_1ST = mass_wet_1ST * SMF_1ST;
67 mass_dry_2ND = mass_wet_2ND * SMF_2ND;
68 mass_vehicle = mass_payl + mass_wet_1ST + mass_wet_2ND;
69 velo_delta_1ST = velo_1ST * log((mass_payl + mass_wet_2ND ...
70           + mass_wet_1ST) / (mass_payl + mass_wet_2ND + mass_dry_1ST));
71 velo_delta_2ND = velo_2ND * log((mass_payl + mass_wet_2ND) ...
72           / (mass_payl + mass_dry_2ND));
73 velo_delta_vehicle = velo_delta_1ST + velo_delta_2ND;
74
75 %      xxxxxxxxxxxxxxxxxxxxxxxxxxxxxxxxxxxxxxxxxxxxxxxxxxxxxxxx
76
77 delta = 'ZZ';
78
79 return;
80
81 end
82
83 %%%%%%%%%%%%%%%%

```

Vehicle Mass Parameters Output

```

1 >>
2
3 -----
4
5     Orbit      =      500.000000      [...]
6     V.Orbit    =      7616.561      [...]
7     V.Mission  =      9500.000      [...]
8
9     ΔV.1 φ     =      4667.513924      [...]
10    ΔV.2 φ     =      4832.486076      [...]
11    ΔV • φ    =      9500.000000      [...]
12
13    ΔV.1 θ     =      4108.950112      [...]
14    ΔV.2 θ     =      5527.666051      [...]
15    ΔV • θ    =      9636.616163      [...]
16
17    B.T.1      =      135.000      [...]
18    B.T.2      =      195.000      [...]
19
20    SMF.1      =      0.075      [...]
21    SMF.2      =      0.125      [...]
22    PMF.1      =      92.500      [...]
23    PMF.2      =      87.500      [...]
24    OMR.1      =      5.631621      [...]
25    OMR.2      =      4.258459      [...]
26    ETA        =      0.000641075875      [...]
27
28  •
29
30    M.Prop.1   =      13443.582      [...]
31    M.Dry..1   =      1090.020      [...]
32    M.Wet..1   =      14533.602      [...]
33    M.Prop.2   =      2157.612      [...]
34    M.Dry..2   =      308.230      [...]
35    M.Wet..2   =      2465.842      [...]
36
37    M.Payl..   =      200.000      [...]
38    M.Vehi..   =      17199.444      [...]
39
40 -----
41
42 >>

```

BIBLIOGRAPHY

- [1] Carl Sagan. *Cosmos*. New York, USA: Random House, 1980. ISBN: 0-394-50294-9.
- [2] Tim Dodd and Mariia Kiseleva. "Soviet Rocket Engines". 2021. URL: <https://everydayastronaut.com/soviet-rocket-engines/> (visited on 06/01/2022).
- [3] "Falcon Nine - SpaceX". 2021. URL: <https://www.spacex.com/vehicles/falcon-9/> (visited on 06/01/2021).
- [4] SpaceNews. "SpaceNews Archive". 2023. URL: <https://spacenews.com/section/news-archive/> (visited on 03/08/2023).
- [5] Vox. "Private spaceflight, explained". 2015. URL: <https://www.vox.com/2015/2/6/18073658/private-space-flight> (visited on 03/01/2023).
- [6] Harbard Business Review. "The Commercial Space Age Is Here". 2021. URL: <https://hbr.org/2021/02/the-commercial-space-age-is-here> (visited on 03/01/2023).
- [7] "Electron - Rocket Lab". 2021. URL: <https://www.rocketlabusa.com/rockets/electron/> (visited on 06/01/2021).
- [8] Harry Jones. "The Recent Large Reduction in Space Launch Cost". Conference Paper, 48th International Conference on Environmental Systems, ICES-2018-81. California, USA, July 2018. URL: <http://hdl.handle.net/2346/74082> (visited on 03/08/2023).
- [9] Space.com. "8 ways that SpaceX has transformed spaceflight". 2022. URL: <https://www.space.com/ways-spacex-transformed-spaceflight> (visited on 03/08/2023).
- [10] John Gardi and Jon Ross. "The Future of Space Launch is Here!" 2022. URL: <http://justatinker.com/Future/> (visited on 03/01/2023).
- [11] Axelspace Corporation. "Announcing the new development of critical components to prepare for the mass production of next-generation microsatellites". Aug. 12,

2020. URL: https://www.axelspace.com/news/press_20201012/ (visited on 03/12/2023).
- [12] George P. Sutton and Oscar Biblarz. *Rocket Propulsion Elements*. Ninth Edition. New Jersey, USA: John Wiley & Sons, Inc., 2017. ISBN: 978-1-118-75388-0.
 - [13] David H. Huang and Dieter K. Huzel. *Modern Engineering for Design of Liquid-Propellant Rocket Engines*. Revised and Updated Edition. Washington DC, USA: American Institute of Aeronautics and Astronautics, 1992. ISBN: 1-56347-013-6.
 - [14] "CODATA Value: Molar Gas Constant". Fundamental Physical Constants. The NIST Reference on Constants, Units, and Uncertainty. May 20, 2019. URL: <https://physics.nist.gov/cgi-bin/cuu/Value?r> (visited on 02/10/2021).
 - [15] George P. Sutton. *History of Liquid Propellant Rocket Engines*. Virginia, USA: American Institute of Aeronautics and Astronautics, 2006. ISBN: 978-1-56347-649-5.
 - [16] Jonathan C. McDowell. "Engine Data Table". Engines, Launch Vehicles. General Catalog of Artificial Space Objects. 2020. URL: <https://planet4589.org/space/gcat/data/tables/engines.html> (visited on 03/05/2021).
 - [17] Mark Wade. "Vinci". Encyclopedia Astronautica. 2019. URL: <http://www.astronautix.com/v/vinci.html> (visited on 03/04/2021).
 - [18] Mark Wade. "RL-10 B-2". Encyclopedia Astronautica. 2019. URL: <http://www.astronautix.com/r/rl-10b-2.html> (visited on 03/04/2021).
 - [19] John D. Clark. *Ignition! An Informal History of Liquid Rocket Propellants*. New Jersey, USA: Rutgers University Press, 1972. ISBN: 0-8135-0725-1.
 - [20] PubChem. "PubChem Compound Summary for CID 977, Oxygen". National Center for Biotechnology Information. 2021. URL: <https://pubchem.ncbi.nlm.nih.gov/compound/Oxygen> (visited on 03/12/2021).
 - [21] Engineering ToolBox. "Oxygen - Thermophysical properties". 2008. URL: https://www.engineeringtoolbox.com/oxygen-d_1422.html (visited on 03/12/2021).
 - [22] Mark Wade. "LOX". Encyclopedia Astronautica. 2019. URL: <http://astronautix.com/l/lox.html> (visited on 03/12/2021).
 - [23] Virginia P. Dawson and Mark D. Bowles. *Taming Liquid Hydrogen: The Centaur Upper Stage Rocket 1958-2002*. The NASA History Series. Washington DC, USA: National Aeronautics and Space Administration, Office of External Relations, 2004. Chap. Introduction. URL: <https://history.nasa.gov/SP-4230.pdf>.
 - [24] PubChem. "PubChem Compound Summary for CID 783, Hydrogen". National Center for Biotechnology Information. 2021. URL: <https://pubchem.ncbi.nlm.nih.gov/compound/Hydrogen> (visited on 03/20/2021).
 - [25] Engineering ToolBox. "Hydrogen - Thermophysical Properties". 2008. URL: https://www.engineeringtoolbox.com/hydrogen-d_1419.html (visited on 03/20/2021).

- [26] College of the Desert. “*Module 1: Hydrogen Properties*”. Hydrogen Fuel Cell Engines and Related Technologies: Revision 0, Dec. 2001. URL: https://www1.eere.energy.gov/hydrogenandfuelcells/tech_validation/pdfs/fcm01r0.pdf (visited on 03/21/2021).
- [27] Robert A. Braeunig. “*Rocket Propellants*”. *Basics of Space Flight*. Rocket & Space Technology. 2008. URL: <http://www.braeunig.us/space/propel.htm> (visited on 02/15/2021).
- [28] Norbert Brügge. “*Space Launch Vehicles*”. *Spacerockets: Database & Analytics*. B14643.de. 2021. URL: <http://www.b14643.de/Spacerockets/index.htm> (visited on 03/22/2021).
- [29] Mark Wade. “*LOX/LH₂*”. Encyclopedia Astronautica. 2019. URL: <http://astronautix.com/l/loxlh2.html> (visited on 04/02/2021).
- [30] Pablo Rachov, Hernán Tacca, and Diego Lentini. “*Electric Feed Systems for Liquid Propellant Rocket Engines*”. Research rep. 2010. URL: <https://www.aacademica.org/hernan.emilio.tacca/9.pdf> (visited on 02/01/2021).
- [31] Mark Wade. “*LOX/Kerosene*”. Encyclopedia Astronautica. 2019. URL: <http://astronautix.com/l/loxkerosene.html> (visited on 04/23/2021).
- [32] “*Detail Specification—Propellant: Rocket Grade Kerosene*”. MIL-DTL-25576D. Washington DC, USA: Department of Defense, May 20, 2005.
- [33] PubChem. “*PubChem Compound Summary for CID 297, Methane*”. National Center for Biotechnology Information. 2021. URL: <https://pubchem.ncbi.nlm.nih.gov/compound/Methane> (visited on 05/21/2021).
- [34] Robert A. Braeunig. “*Rocket Thermodynamics*”. Rocket & Space Technology. 2012. URL: <http://www.braeunig.us/space/thermo.htm> (visited on 02/15/2021).
- [35] Mark Wade. “*LOX/LCH₄*”. Encyclopedia Astronautica. 2019. URL: <http://astronautix.com/l/loxlch4.html> (visited on 05/21/2021).
- [36] Engineering ToolBox. “*Adiabatic Flame Temperatures*”. 2005. URL: https://www.engineeringtoolbox.com/adiabatic-flame-temperature-d_996.html (visited on 04/10/2021).
- [37] Gerald Hagemann. “*LOX/Methane - The Future is Green*”. Airbus Defence & Space, Nov. 4, 2015. URL: <http://www.academie-air-espace.com/upload/doc/ressources/Launchers/slides/hagemann.pdf> (visited on 05/21/2021).
- [38] Engineering ToolBox. “*Methane - Thermophysical Properties*”. 2008. URL: https://www.engineeringtoolbox.com/methane-d_1420.html (visited on 05/21/2021).
- [39] Sanford Gordon and Bonnie J. McBride. “*CEARUN*”. CEA (*Chemical Equilibrium with Applications*). NASA Glenn Research Center, Ohio, USA: NASA, 1994. URL: <https://cearun.grc.nasa.gov/>.

- [40] Sanford Gordon and Bonnie J. McBride. “*Introduction to CEA*”. *Computer Program for Calculation of Complex Chemical Equilibrium Compositions and Applications*. NASA. 1994. URL: <https://cearun.grc.nasa.gov/intro.html> (visited on 06/01/2021).
- [41] Alexander Ponomarenko. “*Rocket Propulsion Analysis*”. *RPA Standard Edition v.2.x*. Version v.2.3.2. Germany, 2008. URL: <https://www.rocket-propulsion.com/index.htm>.
- [42] Robert A. Braeunig. “*Rocket Propulsion*”. *Basics of Space Flight*. Rocket & Space Technology. 2012. URL: <http://www.braeunig.us/space/propuls.htm> (visited on 02/15/2021).
- [43] Robert A. Braeunig. “*Propellant Combustion Charts*”. Rocket & Space Technology. 2005. URL: <http://www.braeunig.us/space/comb.htm> (visited on 02/15/2021).
- [44] Mike Jetzer. “*heroicrelics.org*”. 2021. URL: <http://heroicrelics.org/> (visited on 06/20/2021).
- [45] NASA. “*Turbopump Systems for Liquid Rocket Engines*”. *Space Vehicle Design Monograph*. NASA SP-8107. Aug. 1974. URL: <https://ntrs.nasa.gov/citations/19750012398> (visited on 06/26/2021).
- [46] Hyun-Duck Kwak, Sejin Kwon, and Chang-Ho Choi. “*Performance assessment of electrically driven pump-fed LOX/kerosene cycle rocket engine: Comparison with gas generator cycle*”. Aerospace Science and Technology, Vol. 77. Republic of Korea, 2018. doi: [10.1016/j.ast.2018.02.033](https://doi.org/10.1016/j.ast.2018.02.033). URL: <https://www.sciencedirect.com/science/article/pii/S1270963817320953> (visited on 07/20/2021).
- [47] Pablo Rachov, Hernán Tacca, and Diego Lentini. “*Electric Feed Systems for Liquid-Propellant Rockets*”. Journal of Propulsion and Power, Vol. 29, No. 5. Argentina & Italy, 2013. doi: [10.2514/1.B34714](https://doi.org/10.2514/1.B34714). URL: <https://arc.aiaa.org/doi/10.2514/1.B34714> (visited on 07/20/2021).
- [48] N. Soldà and D. Lentini. “*Opportunities for a Liquid Rocket Feed System Based on Electric Pumps*”. Journal of Propulsion and Power, Vol. 24, No. 6. Italy, 2008. doi: [10.2514/1.35074](https://doi.org/10.2514/1.35074). URL: <https://arc.aiaa.org/doi/10.2514/1.35074> (visited on 07/20/2021).
- [49] Jeffrey Ball. “*The Race Is on to Build a Better Battery*”. FORTUNE. May 24, 2019. URL: <https://fortune.com/longform/race-build-better-battery/> (visited on 06/15/2021).
- [50] Eric Adams. “*The Age of Electric Aviation Is Just 30 Years Away*”. WIRED. May 31, 2017. URL: <https://www.wired.com/2017/05/electric-airplanes-2/> (visited on 06/15/2021).

- [51] Special Metals Corporation. "INCONEL Alloy 625". UNS N06625/W.Nr. 2.4856. 2013. URL: <https://www.specialmetals.com/documents/technical-bulletins/inconel/inconel-alloy-625.pdf> (visited on 06/14/2022).
- [52] "U.S. Standard Atmosphere, 1976". NOAA-S/T 76-1562. Washington DC, USA: National Oceanic, Atmospheric Administration, National Aeronautics, Space Administration, and U.S. Air Force, Oct. 1976.
- [53] John David Anderson Jr. *Fundamentals of Aerodynamics*. Sixth Edition. New York, USA: McGraw-Hill Education, 2017. ISBN: 978-1-259-12991-9.
- [54] Roelof Vos and Saeed Farokhi. *Introduction to Transonic Aerodynamics*. Fluid Mechanics and Its Applications, Volume 110. The Netherlands: Springer, 2015. ISBN: 978-94-017-9747-4.
- [55] Jan Östlund. "Flow Processes in Rocket Engine Nozzles with Focus on Flow Separation and Side-Loads". Stockholm, Sweden: Royal Institute of Technology, 2002. URL: <http://www.diva-portal.org/smash/get/diva2:7328/FULLTEXT01.pdf> (visited on 11/15/2021).
- [56] J. H. Ahlberg, S. Hamilton, D. Migdal, and E. N. Nilson. "Truncated Perfect Nozzles in Optimum Nozzle Design". ARS Journal, Vol. 31, No. 5. Connecticut, USA, May 1961. doi: [10.2514/8.5577](https://arc.aiaa.org/doi/10.2514/8.5577). URL: <https://arc.aiaa.org/doi/10.2514/8.5577> (visited on 01/04/2022).
- [57] L. V. Gogish. "Investigation of Short Supersonic Nozzles". AN SSSR, Izvestiya, Mechanika Zidkosti i Gaza. 1966.
- [58] G. V. R. Rao. "Exhaust Nozzle Contour for Optimum Thrust". Journal of Jet Propulsion, Vol. 28, No. 6. California, USA, June 1958. doi: [10.2514/8.7324](https://arc.aiaa.org/doi/10.2514/8.7324). URL: <https://arc.aiaa.org/doi/10.2514/8.7324> (visited on 03/01/2022).
- [59] G. V. R. Rao. "Approximation of Optimum Thrust Nozzle Contour". Technical Notes. ARS Journal, Vol. 30, No. 6. California, USA, June 1960, p. 561. doi: [10.2514/8.5151](https://arc.aiaa.org/doi/10.2514/8.5151). URL: <https://arc.aiaa.org/doi/10.2514/8.5151> (visited on 03/10/2022).
- [60] Nobuyuki Yatsuyanagi. "Comprehensive Design Method for LOX/Liquid-Methane Regenerative Cooling Combustor with Coaxial Injector". Transactions of the Japan Society for Aeronautical and Space Sciences, Vol. 52, No. 177. Japan, 2009, pp. 180–187. doi: [10.2322/tjsass.52.180](https://www.jstage.jst.go.jp/article/tjsass/52/177/52_177_180/_pdf/-char/en). URL: https://www.jstage.jst.go.jp/article/tjsass/52/177/52_177_180/_pdf/-char/en (visited on 07/27/2022).
- [61] H. C. Starck. "C-103 Nb Alloy: Properties & Applications". Aug. 10, 2020. URL: <https://www.hcstarsolutions.com/c103-nb-alloy-properties-applications/> (visited on 08/15/2022).

- [62] G. S. Gill and W. H. Nurick. “*Liquid Rocket Engine Injectors*”. *Space Vehicle Design Monograph*. NASA SP-8089. Mar. 1976. URL: <https://ntrs.nasa.gov/citations/19760023196> (visited on 08/14/2022).
- [63] John C. Melcher and Robert L. Morehead. “*Combustion Stability Characteristics of the Project Morpheus Liquid Oxygen / Liquid Methane Main Engine*”. Conference Paper, 50th AIAA/ASME/SAE/ASEE Joint Propulsion Conference. Ohio, USA, 2014. doi: [10.2514/6.2014-3681](https://arc.aiaa.org/doi/10.2514/6.2014-3681). URL: <https://arc.aiaa.org/doi/10.2514/6.2014-3681> (visited on 07/27/2022).
- [64] James R. Hulka and Gregg W. Jones. “*Performance and Stability Analyses of Rocket Thrust Chambers with Oxygen/Methane Propellants*”. Conference Paper, 46th AIAA/ASME/SAE/ASEE Joint Propulsion Conference. Tennessee, USA, July 2010. doi: [10.2514/6.2010-6799](https://arc.aiaa.org/doi/abs/10.2514/6.2010-6799). URL: <https://arc.aiaa.org/doi/abs/10.2514/6.2010-6799> (visited on 07/27/2022).
- [65] Howard D. Curtis. *Orbital Mechanics for Engineering Students*. Fourth Edition. Butterworth-Heinemann, 2020. ISBN: 978-0-08-102133-0.

& to my Mom

Division of Space Technology
Department of Computer Science, Electrical and Space Engineering

Luleå University of Technology 2023

